Cyclotron-Cavity Mode Resonant Cooling in Single Component Electron Plasmas

by

Alexander Peter Povilus

A dissertation submitted in partial satisfaction of the
requirements for the degree of
Doctor of Philosophy

in

Physics

in the

Graduate Division

of the

University of California, Berkeley

Committee in charge:

Professor Joel Fajans, Chair
Professor Jonathan Wurtele
Professor Edward Morse

Spring 2015

Cyclotron-Cavity Mode Resonant Cooling in Single Component Electron Plasmas

Abstract

Cyclotron-Cavity Mode Resonant Cooling in Single Component Electron Plasmas

by

Alexander Peter Povilus

Doctor of Philosophy in Physics

University of California, Berkeley

Professor Joel Fajans, Chair

Generating cold single component electron plasmas, below 20K, is of interest to many experiments that require low temperatures for optimizing recombination rates or producing monoenergetic beams. Here, we report on the demonstration of a technique that allows for rapid cooling of a single-component electron plasma confined in a Penning trap. Electrons are confined in an electromagnetic cavity, allowing use of the Purcell effect to enhance spontaneous emission of cyclotron radiation in the cavity. This allows for faster passive thermalization of the confined plasma to the temperature of electrodes that constitute the cavity.

This thesis is dedicated to Marissa and Anna.

Contents

List of Figures

List of Tables

Acknowledgments

This work would not have been possible without the help and encouragement of many people over my graduate career at Berkeley.

I would like to thank my wife, Marissa, and daughter, Anna, for their patience with my irregular schedule and long hours. It took a longer than expected, but it's finally done.

Thanks to Steve Chapman, who has been a friend and colleague since undergrad at the University of Michigan. It seems like we're going to still be on similar research trajectories for a while.

The final push for data while I was writing my thesis was done by Eric Hunter, who will be the next graduate student to run this experiment. I have taken him up the tallest ladder in the lab and proclaimed that all equipment that he could see will one day be his to fix.

Our collaborators at University of British Columbia, Walter Hardy and Nathan Evetts designed the bulge cavity which made the cooling behavior possible to observe in the final weeks.

I would like to thank the graduate students and postdocs who have been a part of the lab and their invaluable contributions to this project, including Marcelo Baquero-Ruiz, Chukman So, Andrey Zhmoginov, Andy Charman, Punit Ghandi, Fumika Isono, Celeste Carruth, and Will Bertsche.

I would also like to thank the many undergraduates who have contributed (and I may have conned into joining the group): Crystal Bray, Arielle Little, Matthew Turner, Zak Vendeiro, Caroline Wurden, Nicole Lewis, Sabrina Shanman, Nate Belmore. Keep ambitious.

Thanks to Joel Fajans and Jonathan Wurtele for being my advisors for nearly a decade; I have had the fairly unique experience of developing and running a large experiment during my time here, and it would not have been possible without your advice and support. Now I get to be someone else's problem.

I would like to thank my thesis committee for their feedback and willingness to revise the thesis, allowing me to start a new postdoctoral position on schedule.

Chapter 1

Introduction

1.1 Motivation

Non-neutral plasmas are plasmas that have a net charge, usually by depletion of one charged species in the plasma. This can change the behavior of the plasma since self-fields tend to play a significant role in the dynamics. These plasmas typically appear in a wide variety of experiments such as focusing charge beams [41], surface porosity and defect analysis [34], antimatter recombination experiments [3, 9, 32], positron annihilation spectroscopy [67, 73], and strongly coupled Coloumb crystals generated from laser ionization [12, 23]. It is of particular interest to understand the dynamics of these plasmas since many of the processes in these experiments are highly dependent on the energy and density distribution of confined charges.

Non-neutral plasmas often contain interesting processes, such a neutral synthesis and low-energy collisional dynamics, at low temperatures. Unfortunately low temperature is a somewhat nebulous term since there are many thresholds for which interesting behavior can occur. This can range anywhere from when electron collision rates are inhibited in a strong magnetic field ($\sim$ 400K) [10, 57], through species separation in a multi-species plasma [52, 6, 21], to the strong coupling regime where the plasma structure crystallizes ($\sim$ 1K) [12]. In this thesis, we focus on confined, single species electron plasmas, with the intention to use the plasmas for recombination experiments that generally attempt to operate near 10K. Note that these plasmas are outside the strong-coupling regime, such that crystallization is not expected to play a role in the dynamics.

Our group is affiliated with the Antihydrogen Laser Physics Apparatus (ALPHA) collaboration, a group dedicated to performing precision spectroscopy on the antihydrogen atom. In this experiment, low temperatures are necessary for guaranteeing high recombination rates, via $e^+ + e^+ + \bar{p} \rightarrow e^+ + \bar{H}^*$ collisions, which scale as $T^{-9/2}$ [54]. Additionally, since the magnetic moment of ground state antihydrogen, determined mostly by the positron spin, is relatively weak the trapping potentials are limited to 0.8K depth; antihydrogen created must have kinetic energies below this level if it is to be trappable. These considerations necessitate finding ways to generate colder plasmas in order to improve the efficiency of antihydrogen synthesis operations, now limited to $\sim 1-2$ per experimental cycle (100s).

Generally, non-neutral plasmas in these regimes are contained in a strong magnetic field. This provides a confinement of charged particles transverse to field lines, as particles are, to good approximation, locked to field lines by cyclotron motion. The strong magnetization allows for a variety of unusual behaviors in a non-neutral plasma, some distinctly advantageous for our applications. In particular, the cyclotron motion permits charged particles in the trap to radiate away energy via Larmor radiation, providing a natural cooling mechanism for confined plasmas. The ALPHA and ATRAP antihydrogen experiments at CERN rely on this mechanism for cooling lepton, i.e. electron or positron, plasmas. Unfortunately, there are also complications that arise. For example, in these strongly magnetized regimes, these axial and transverse degrees of motion tend to decouple at lower temperatures [10]. Characterization of such effects is a rich field of study that is necessary for understanding confined non-neutral plasma behavior.

Achieving low temperatures reliably in pure lepton plasmas has proven elusive to the non-neutral plasma community, but it is a critical part of the antihydrogen synthesis process. Cold non-neutral plasmas have been generated by laser cooling [46]. However, electrons do not have internal states to interact with, and attempts to couple with cyclotron motion to axial motion using RF appear impractical on typical experimental timescales [49]. This is not to suggest that small numbers of confined leptons have not been cooled to low temperatures [75, 60], but these experiments do not have the high collision rate or collective effects generally associated with plasma dynamics. The technique demonstrated by these experiments, the enhanced coupling of cyclotron motion to electromagnetic cavity modes resonances, a realization of the Purcell effect, is still applicable to a plasmas. In this thesis we report on a demonstration of cavity-enhanced cooling of a pure electron plasma in the large-N confinement regime.

1.2 Overview

The work presented in this thesis was done over the course of nine years during my graduate career. During this time I had the opportunity to work as part of the ALPHA collaboration towards the development of trapped antihydrogen[9]. As a member of the collaboration, I developed diagnostic systems for plasma behavior, discussed in Chapter 4. I was particularly troubled by the cooling behavior of plasmas in the ALPHA experiment. Although the walls of the trap were cooled to nearly 4K, electron plasmas generally were found to thermalize to $\sim$ 50K. While this has been improved upon in the recent iteration of ALPHA, the electrons are still not thermalizing with electrode material.

In a search for a solution, I decided to investigate the effect that cavity modes would have on the plasmas. The electrode structure at ALPHA was unsuitable for this study because the electrode stack used was not designed to have large Q, the closable aperture was not behaving reliably at the time, and electrode geometry was complicated by a need to accommodate electrodes with high voltages for antiproton capture. At this point, I was given the opportunity to design and build a cold electron plasma trap at Berkeley to study these effects. This trap, the Cold Electron Research (CERES) apparatus, was designed to search for cavity mode interactions with these plasmas in the hopes of generating a reliable, cold source of plasmas. A large number of fellow graduate and undergraduate students have assisted in the construction and operation of this device during my time at Berkeley.

In this thesis, we will start by reviewing some basic non-neutral plasma physics in this chapter, relevant to understand the behavior of this system. In Chapter 2, we will review cavity mode interactions and provide a model for a collective bottleneck effect that is caused by saturation of the cavity mode. The following two chapters, 3 and 4, are dedicated to discussing the structure of the apparatus and the diagnostics used, respectively. Finally, results are presented for the observation of enhanced cavity modes (Chapter 5) and additional plasma behaviors that we discovered while reaching this goal (Chapter 6).

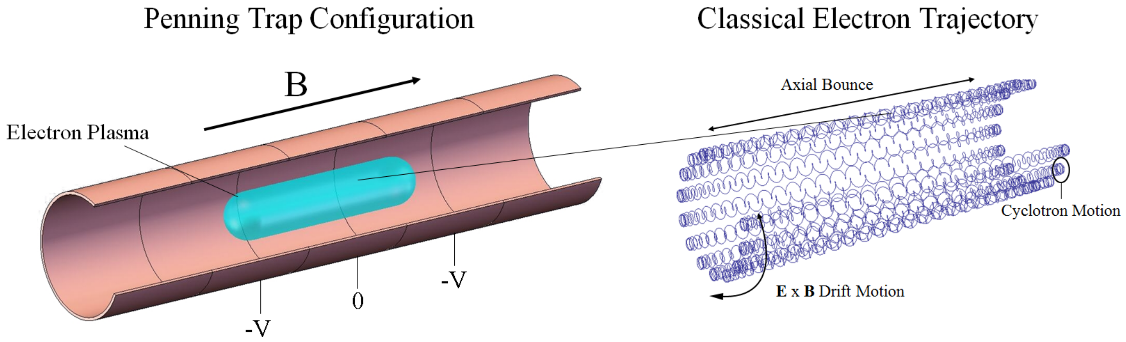

Figure 1.1: Penning Trap Configuration. Electrons are trapped by a combination of strong axial magnetic field and electrostatic fields applied by cylindrical electrodes. A typical classical electron orbit with the hierarchy of motion is shown on the right.

1.3 Non-Neutral Plasma Confinement in Penning Traps

We confine single component electron plasmas using a Penning-Malmberg trap. In this configuration, electrons are confined in a stack of cylindrically-symmetric electrodes. A homogeneous, strong magnetic field is applied to confine the transverse motion of the particles, while a electrostatic potential is applied to the electrodes for axial confinement. Confined electrons behave like a plasma since the electrons will tend to distribute themselves such that the axial electric field is zero inside the ensemble of particles. There is, however, a non-zero transverse field component that arises since the electrons are, to zeroth-order, confined to field lines. This transverse field generates an $\mathbf{E} \times \mathbf{B}$ drift in the plasma. If the plasma is azimuthally-symmetric, this drift motion follows a circular orbit around the axis of the plasma; if the plasma has constant desnity, the plasma exhibits a bulk rigid rotation with $\omega_m = en/(8\pi\epsilon_0 B)$, ignoring corrections due to finite electrode size. A diagram depicting these basic Penning trap behaviors is shown in Fig. 1.1.

This results in a hierarchy of motion for confined electrons. Electrons exhibit fast, circular cyclotron motion about field lines with angular frequency $\omega_c = eB/m$. The axial motion of electrons has two relevant time scales, the expectation of a bounce frequency of an individual electron in the plasma with thermal velocity $\nu_b = \sqrt{k_b T/m_e}/2L$, and the angular frequency from bulk displacement of the plasma ω_z, resulting from the electrostatic confinement potential applied. Frequencies in our plasmas are expected to have ordering,

$$\omega_c \gg 2\pi\nu_b, \omega_c \gg \omega_m. \tag{1.1}$$

Note that while most of the frequencies listed here describe plasma oscillations, the quantity ν_b does not describe a coherent plasma oscillation in the system, but rather a useful scale of time to understand the dynamics of the system.

Under this ordering the transverse bulk drift appear decoupled, however the general solution for particle has combined fast and slow components of transverse motion,

$$\omega_{\pm} = \frac{\omega_c}{2}\left(1 \pm \sqrt{1 - \omega_m/\omega_c}\right). \tag{1.2}$$

The case where $\omega_m = \omega_c$ describes an upper bound for the density of charge confined in the trap, known as the Brillouin density. The hierarchy also allows for stability in plasma confinement; if frequencies are too close, then perturbations to confinement fields would cause the plasma to couple the axial and transverse motions, leading to instabilities. An example of this is seen by zero-frequency modes in confined antiproton plasmas where $\nu_b \sim \omega_m$ can lead to loss of confinement. [7]

Finite Trivelpiece-Gould Modes

Bulk excitation of a thermalized non-neutral plasma takes the form of Trivelpiece-Gould modes [22]. These modes represent collective perturbations to the magnetized plasma distribution under the influence of an external confinement potential and are analogous to the description of lower order collective modes in an ion trap [42] . These modes are important since excitation of these modes is the typical way in which energy is transfered into our plasmas. Excitations at the mode frequencies are convenient for generating heating due to the accessibility of their typical frequency range, which typically have $f \sim \mathcal{O}(10\text{MHz})$, and can be used as a coarse diagnostic for many plasma parameters [50]. This also means that heating effects can be due to noise present in this band and present an experimental challenge in reducing the exposure of the plasma to non-thermal noise external to the confinement region.

Evaluation of the frequencies associated with these modes is often simplified under the assumption that the confinement length of the plasma is very long relative to the radius of the plasma, such that the plasma has a flattop radial profile. Unfortunately, we do not have this luxury in our system, and so the mode location and behavior is difficult and costly to predict *a priori*. The mode behavior is established empirically in our system based on observation of driven perturbations to the plasma.

Instabilities Associated with Penning Traps

Electron plasmas that are trapped have a long but finite lifetime. This is due to the fact that electron-electron collisions in the plasma conserve the canonical angular momentum. As a result, $\langle r^2 \rangle$ is conserved, where the average is taken over the confined particles. Three main effects lead to loss of confinement: electron-neutral collisions with the background gas [27], diocotron instabilities caused by resistive drag on the plasma from image charges on the electrode walls [51], and non-azimuthal symmetry in the applied fields [15].

Electron-neutral plasma collisions are inherent in Penning trap systems due to a trace amount of molecules in the vacuum system. The diffusion caused by collisions with background gases is expected to scale as $\partial_t \langle r^2 \rangle \propto N\nu_{en}/\omega_c^2$. This behavior has a significant effect for the typical conditions and timescales that our experiment runs within at background pressures $\sim 10^{-9}$mbar. Typically the in-cavity vacuum is significantly less than this since the walls are cryogenic and background gases tend to adsorb to the walls. It is unclear at what timescale the walls saturate, but occasional reheating of the trap can be required to keep pressures low.

Diocotron instabilities are caused when the plasma distribution is not axisymmetric. When the plasma has an offset from the center of the electrode stack (an $m = 1$ diocotron mode), this causes a bulk drift, with angular frequency ω_D, about the trap axis due to the electric fields generated by image charges. This drift satisfies the condition that $\omega_m \ll \omega_D$ since the plasma is generally small relative to the inner diameter and near the center of the trap. The image charges contribute a dissipative effect, unintuitively driving the plasma to higher radius. This can eventually result in the plasma being driven into the electrode wall; this effect is a concern where the trap may lack azimuthal symmetry such as near the sectored electrodes.

Finally, collisions in the plasma no longer conserve the canonical angular momentum when azimuthal asymmetries are introduced into the system. The scaling and behavior of diffusion caused by this effect was studied by a former graduate student in the group, Steve Chapman [15]. It is possible that this can drive expansion in our plasma due to imperfections in the electrode structure and coil geometry.

It is often critical to check that plasmas are not rapidly expanding from these behaviors since many of the effects discussed in this thesis assume that the plasma is well-centered in the trap and that the expansion of the plasma is slow. The expansion term is particularly important since radial diffusion causes Joule heating in the plasma due to the transverse self-fields of trapped charges. There is a discrepancy, however since the observed heating rates in our plasma from diffusion generally account for only $\sim 10\%$ of the heating required to match equilibrium temperatures observed.

Plasma Manipulation

Confined plasmas are manipulated by application of magnetic and electric fields. Many manipulations involve varying the electrostatic potentials applied to the electrodes, allowing shaping of the confinement well and transport of particles through the electrode structure. Generally these potentials will vary on timescales $\geq 10\mu$s to ensure adiabatic manipulation in the plasma. Faster signals can be applied to resonantly interact with the plasma through axial plasma modes or the $\mathbf{E} \times \mathbf{B}$ drift motion. We do not interact with the cyclotron motion directly since this is ≥ 20GHz in the fields we operate, and this frequency cannot be easily coupled into the cavity.

In particular, the fast signals can be used to torque the plasma through the "rotating wall" technique, by driving the ω_m drift motion with a rotating transverse electric field [25].

This can be used to compress and center the plasma in the trap. We discuss this technique in detail in Sec. 6.1 where we explored optimization of this technique for short length plasmas.

The solenoid magnetic field in which we operate can be shifted to adjust the cyclotron frequency. This is important for tuning the cyclotron-cavity resonances that are the focus of this thesis. Transverse fields can be applied to steer beams and correct magnetic field misalignments. For hybrid traps, such as those in $\bar{H}$-synthesis experiments, additional multipole magnetic fields are applied to the trap to provide minimum-B confinement for diamagnetic states ground states of $\bar{H}$.

Chapter 2

Theory of Cavity-Cyclotron Resonance Cooling

In this chapter we present a theoretical formulation of the cavity-cyclotron coupling in the cavity and the implications it has for passive cooling of a large number ($N > 10^4$) of particles confined in a Penning trap geometry. The formulation assumes that the dominant mechanism to enhanced cooling rates is the Purcell effect [62], where the emission rate of atoms is predicted to change based on the environment within which the atoms are confined. This effect has been observed in a variety of physical systems utilizing quantum dots and atoms confined in cavities [31, 37, 79]. In order to use this effect on cyclotron emission in our system, I found that some theoretical formalism needed to be tailored to apply to our particular cavity geometry.

Section 2.1 reviews the cavity mode structure and the Purcell effect. The cavity modes and interaction with magnetized electrons needed to characterize behavior in our Penning trap are derived.

Section 2.2 describes a contribution I made to the understanding of a fundamental multiparticle effect, cavity mode saturation of the cooling rate, important in a regime where the density modes is sparse such that particles are expected to radiate into a single cavity mode. In different words, if there is a large number of electrons in a high quality factor cavity, the electrons will tend to thermalize with the electromagnetic mode such that cooling becomes dependent on the cavity-thermal bath coupling rather than the cyclotron cavity coupling. Here, limits are characterized for when this behavior becomes significant and theoretical cooling rates are calculated.

2.1 Cyclotron Cooling of Electrons in a Finite Penning Trap Cavity

We are interested in finding the expected cooling rate of strongly-magnetized electrons confined in a Penning trap from spontaneous emission of cyclotron radiation. We will be making use of the Landau quantization of a free particle and the quantized electromagnetic field in a cavity to an effective impedance of electrons in the cavity coupling to the walls. While the calculation of radiative cooling does not necessarily require quantum mechanics, the coupling rates are easier to calculate and visualize as coupled harmonic oscillators in this method. Additionally, since we want to generate plasmas in the regime where $T \approx \hbar\Omega_c$, we want to explore possible quantized behavior.

It should be noted that this approach is a specific case evaluation of the Purcell effect [62]. The methods for calculating the emission rates are similar to those used to predict inhibited spontaneous emission of an atom in a cavity [35, 47]. In our case, the transverse motion of the electrons is treated as a pseudoatomic system for purposes of emission. This resonant coupling behavior has previously been observed for small numbers of electrons in a resonant cavity ($N \leq 10^5$) by Hanneke and Gabrielse in 2007 [38], but has not been observed for cavities with a larger number of particles. Cavity-enhanced cooling, while discussed by Hanneke in the context of driven sideband cooling, is also applicable to understanding passive cooling. In the following, we present a formal review of this mechanism and recover predicted cooling rates for electrons in this cavity.

Cyclotron cooling is an inherently single-particle phenomemon since, to highest order, the cooling rates depend only on the acceleration of the charged particles in a magnetic field. The radiation in a high magnetic field is much higher that the plasma frequency, and so it is assumed to pass through the plasma with only resonant scattering effects. These effects, described in this section, take the form of absorption and emission terms in the particle-field interaction. Calculations are presented in Heaviside-Lorentz units.

Electromagnetic Cavity Modes

In this section we will do a quick review of the structure of electromagnetic cavity modes. From classical electrodynamics, we know that the modes in a cavity are the solutions to,

$$\left(\nabla^2 - \frac{1}{c^2}\frac{\partial^2}{\partial t^2}\right)\mathbf{A} = 0. \tag{2.1}$$

where $\mathbf{A}$ is the vector potential. The vector potential satisfies,

$$\mathbf{B} = \nabla \times \mathbf{A}, \quad \mathbf{E} = -\frac{1}{c}\frac{\partial \mathbf{A}}{\partial t} \tag{2.2}$$

In a perfectly conducting cylindrical cavity, the solutions to this wave equation can be split into modes with either transverse electric (TE) or transverse magnetic (TM) fields. The solutions have boundary conditions $\partial B_z/\partial n|_{\partial V} = 0$ and $E_z|_{\partial V} = 0$, respectively. More explicitly, the wavefunction solutions take the form,

$$\begin{aligned}
\text{(TM)}\quad \mathbf{A}\left(\mathbf{x},t\right) &= \nabla\times\nabla\times\left(\frac{C_{mnk_z}}{\omega}J_m(\gamma_{mn}\rho)\cos\left(k_z z\right)e^{i(m\phi-\omega t)}\right)\hat{z} && (2.3)\\
\text{(TE)}\quad \mathbf{A}\left(\mathbf{x},t\right) &= i\omega\nabla\times\left(\frac{C_{mnk_z}}{\omega}J_m(\gamma'_{mn}\rho)\sin\left(k_z z\right)e^{i(m\phi-\omega t)}\right)\hat{z}. && (2.4)
\end{aligned}$$

In these equations, $\gamma_{mn} = x_{mn}/R_w, \gamma'_{mn} = x'_{mn}/R_w$ where R_w is the radius of the cylinder, x_{mn} nth zero of J_m, and x'_{mn} nth zero of J'_m. The frequency of the mode is given by $\omega = c\sqrt{k_z^2+\gamma_{mn}^2}$.

In a realistic cavity, the boundary conditions are relaxed since electromagnetic waves will penetrate a small distance into the walls of the cavity. This behavior allows the cavity modes to thermalize with the walls of the cavity. The extent of this coupling is described in terms of an effective quality factor, Q, for each mode of the cavity. The result is a broadening, Γ, and downshift, $\Delta\omega$ of the cavity mode frequencies,

$$\Gamma = \frac{\omega}{Q}, \quad \Delta\omega = -\frac{\omega}{2Q}. \tag{2.5}$$

We can switch from a classical modes in the cavity to quantized formalism easily since the mode structure is known. The vector potential $\mathbf{A}$ is expressed in terms of raising and lowering operators a and $a^\dagger$ for each cavity mode,

$$\mathbf{A_r ad} = c\sum_{mnk_z\alpha}\sqrt{\frac{\hbar}{2V\omega}}\left[a_{mnk_z\alpha}\mathbf{u}_{mnk_z\alpha}(\mathbf{x},t)e^{-i\omega t} + \text{c.c.}\right]. \tag{2.6}$$

The value α is the "polarization" of the cavity mode, either TE or TM. The essential difference between the classical and quantized value for the vector potential is that the quantized vector potential is normalized for discrete numbers of photons. Normalizing the classical fields, we find that,

$$\begin{aligned}
\mathbf{u}_{mnk_z(\text{TE})} &= \sqrt{\frac{2}{\gamma'^2_{mn}\beta'_{mn}}}\left(\frac{im}{\rho}J_m(\gamma'_{mn}\rho)\hat{\rho} + \gamma_{mn}J'_m(\gamma'_{mn}\rho)\hat{\phi}\right)\\
&\quad\times e^{im\phi}\sin\left(k_z z\right)\\
\mathbf{u}_{mnk_z(\text{TM})} &= \sqrt{\frac{2c^2}{\omega^2\gamma^2_{mn}\beta_{mn}}}\Big(\gamma_{mn}k_z J'_m(\gamma_{mn}\rho)\sin\left(k_z z\right)\hat{\rho}
\end{aligned}$$

$$
\begin{aligned}
&+\frac{imk_z}{\rho}J_m(\gamma_{mn}\rho)\sin{(k_z z)}\hat{\phi} \\
&+\left[\gamma_{mn}^2 J_m''(\gamma_{mn}\rho)+\frac{\gamma_{mn}}{\rho}J_m'(\gamma_{mn}\rho)-\frac{m^2}{\rho^2}J_m(\gamma_{mn}\rho)\right] \\
&\left.\times\cos{(k_z z)}\hat{z}\right)e^{im\phi}. \qquad (2.7)
\end{aligned}
$$

Using the definition of a Bessel function, the $\hat{z}$ term in the TE mode can simply be reduced to $\gamma_{mn}^2 J_m(\gamma_{mn}\rho)\cos{(k_z z)}$. The normalization constants β and β' are given by,

$$
\beta'_{mn}=(J_m^2(\gamma'_{mn})-J_{m+1}^2(\gamma'_{mn})); \quad \beta_{mn}=J_{m+1}^2(\gamma_{mn}). \qquad (2.8)
$$

For later reference, there are two identities for Bessel functions that will become particularly useful in future calculations,

$$
\begin{aligned}
J_m(x) &= \frac{x}{2m}(J_{m-1}(x)+J_{m+1}(x)) \\
J_m'(x) &= \frac{1}{2}(J_{m-1}(x)-J_{m+1}(x)). \qquad (2.9)
\end{aligned}
$$

Landau Quantization

Before we discuss the particle interaction with the field from the previous section, we need to examine the dynamics of a charged particle in a strong magnetic field. Since we would like to perform a quantum mechanical calculation of this interaction, we briefly review the wavefunction solutions for a particle in a homogeneous magnetic field. This solution is presented in Landau and Lifschitz's textbook, *Quantum Mechanics* [48].

Algebraic Solution

The Hamiltonian for this system is,

$$
H=(\pi)^2/2m=(\mathbf{p}+q\mathbf{A}/c)^2/2m \qquad (2.10)
$$

Here, we use the Landau gauge for a homogeneous magentic field B_0 in the $\hat{z}$ direction, $\mathbf{A}\rightarrow\mathbf{A}_0=B_0 x\hat{y}$. For this calculation, we do not include the spin of the electron. Solving the for the energy eigenvalues and eigenfunctions of this equation, we have:

$$
\begin{aligned}
\psi_{k_y k_z n}(\mathbf{x}) &= \phi_n\left(x-\frac{\hbar k_y}{m\omega_c}\right)e^{i(k_y y+k_z z)}; \\
E_{k_y k_z n} &= \frac{\hbar^2 k_z^2}{2m}+\left(n+\frac{1}{2}\right)\hbar\omega_c. \qquad (2.11)
\end{aligned}
$$

Here, $\omega_c = \frac{eB_0}{m}$ is the cyclotron frequency and $\phi_n x$ is the n^{th} wavefunction of the 1D harmonic oscillator. Since the solution takes the form of the harmonic oscillator, we can convert p_x and x basis into a raising and lowering operator ($b^\dagger$ and b) basis, simplifying cyclotron emission calculations. Out of convenience, we use $\tilde{x} = x - \frac{\hbar k_y}{m\omega_c}$ such that,

$$\begin{aligned} p_{\tilde{x}} &= i\sqrt{\frac{\omega_c \hbar}{2m}}\left(b^\dagger - b\right) \\ \tilde{x} &= \sqrt{\frac{\hbar}{2\omega_c m}}\left(b^\dagger + b\right). \end{aligned} \tag{2.12}$$

Wavefunction solution

It is also useful to know the quantized waveform in a magnetic field. In particular, we will want to have an expression for the waveform for a single particle so that we can perform a time-dependant perturbation to evaluate collision rates.

We will use the Landau gauge for this derivation. That is, $\mathbf{A} = \frac{1}{2}\mathbf{x} \times (B\hat{z})$. Using this gauge, we rewrite Eq. 2.10 in cylindrical coordinates,

$$H = -\frac{\hbar^2}{2m}\left(\frac{\partial^2}{\partial z^2} + \frac{1}{r}\frac{\partial}{\partial r}r\frac{\partial}{\partial r} + \frac{1}{r^2}\frac{\partial^2}{\partial \phi^2}\right) - \frac{i\hbar\omega_c}{2}\frac{\partial}{\partial \phi} + \frac{m\omega_c^2 r^2}{8}, \tag{2.13}$$

such that $\omega_c = qB/(mc)$, i.e. the cyclotron frequency. Note that H is easily seperable into r,θ, and z components, and that $[H, p_z] = 0; [H, L_z] = 0$. Thus, we reduce our wavefunction to the form,

$$\psi_{l,k_z}(r, \phi, z) = \sqrt{(1/\pi L)}R_l(r)\exp\left(i(l\phi + k_z z)\right), \tag{2.14}$$

where integer l and real-valued k_z are quantum numbers of $L_z, p_z/(i\hbar)$ respectively, and the $\sqrt{(1/\pi L)}$ is a normalization constant with L being the extent of our wavefunction along z; we will later take the limit $L \to \infty$. The function $R_l(r)$ is a solution to the reduced Hamiltonian,

$$\tilde{H}_l = -\frac{\hbar^2}{2m}\left(\frac{1}{r}\frac{\partial}{\partial r}r\frac{\partial}{\partial r} - \frac{1}{r^2}l^2\right) + \frac{\hbar\omega_c}{2}l + \frac{m\omega_c^2 r^2}{8}. \tag{2.15}$$

This differential equation has allowed energies, $\tilde{E}_n = (n + \frac{1+l+|l|}{2})\hbar\omega_c$. In this case, we have our second transverse quantum number, n, which in conjunction with Eq. 2.15 gives appropriate radial wave solutions,

$$R_{nl}(r) = \sqrt{\frac{m\omega_c \Gamma(n+1)}{2\pi\hbar\Gamma(n+|l|+1)}}\xi^{|l|}L_n^{|l|}(\xi^2)\exp\left(-\xi^2/2\right), \tag{2.16}$$

where $\xi = \sqrt{\frac{m\omega_c}{2\hbar}}r$ and L_p^q is an associated Laguerre polynomial.

Particle-Field Interaction

Having established the structure of the electron and photon field separately, we now combine the two systems to look at emission/absorption rates. For this calculation, we modify the vector potential of the one-particle Hamiltonian in Eq. 2.10 to include cavity mode terms,

$$\mathbf{A} \rightarrow \mathbf{A}_0 + \mathbf{A}_{\text{rad}}, \tag{2.17}$$

where the radiation component of the vector potential is given by Eq. 2.6. In this case, we can split the Hamiltonian into two terms, [64]

$$\begin{aligned} H &= H_0 + H_{\text{int}} \\ &= \left(\frac{(\mathbf{p} + e\mathbf{A_0}/c)^2}{2m} + H_{\text{rad}} \right) + \left(\frac{e}{2mc} \{ \mathbf{p} + e\mathbf{A_0}/c, \mathbf{A}_{\text{rad}} \} + \frac{e^2 \mathbf{A}^{\mathbf{2}}_{\text{rad}}}{2mc^2} \right). \end{aligned} \tag{2.18}$$

The term $\frac{e^2\mathbf{A}^{\mathbf{2}}_{\text{rad}}}{2mc^2}$ is considered neglegible since the radiation field is generally thermalized to low temperatures, and so pondermotive forces do not make a signficiant contribution to the Hamiltonian. The free radiation field Hamiltonian is provided by Sakurai [64] in the simple form, $H_{\text{rad}} = (1/2) \sum_{m,n,k,\alpha} \hbar\omega_c (a^{\dagger}_{mnk_z\alpha} a_{mnk_z\alpha} + a_{mnk_z\alpha} a^{\dagger}_{mnk_z\alpha})$. The unperturbed term, with particle and radiation field decoupled, is perturbed by an interaction term that represents the coupling between the two systems. We can then calculate transition rates in the combined system using Fermi's rule,

$$\Gamma_{i \rightarrow f} = \frac{2\pi}{\hbar} | \langle f | H_{\text{int}} | i \rangle |^2 D_E. \tag{2.19}$$

When using Fermi's rule, there is an implicit assumption that the time of observation is longer than ω_c^{-1} and each H_{int} matrix element is small relative to $\hbar\omega_c$, both applicable to cooling operations which generally have $\Gamma \ll \omega_c$. It may seem that in combining the two systems, we have ignored the boundary conditions of the cavity in the case of the particle. However, since we are working with low-energy electrons, we would expect the transverse component of the wavefunction to be localized on the length scale of the typical Larmor radius in the system ($\approx 1\mu$m), so the finite size of the cavity is not an issue. In addition, since the wavelength of the radiation is much larger than the Larmor radius, $r_L = \sqrt{\frac{2k_BT}{m}}/\omega_c$, we can use a dipole approximation in the transverse direction to eliminate contributions from multi-photon transitions.

Example: Magnetized Particle in Free Space

We first reproduce the emission rates in free space. In free space, the radiation field has,

$$\mathbf{u}_{\mathbf{k}\alpha} = \vec{\epsilon}^{\,(\alpha)}_{\mathbf{k}} e^{i(\mathbf{k}\cdot\mathbf{x})}. \tag{2.20}$$

Here, $\vec{\epsilon}_{\mathbf{k}}$ is a the standard polarization vector in the $\hat{k}$ direction. Using the dipole approximation $e^{i(\mathbf{k}\cdot\mathbf{x})} \to 1$ and substituting raising and lowering operators from Eq. 2.12, the interaction term becomes,

$$\begin{aligned} H_{\text{int}} &= \frac{e}{mc}(\mathbf{p} - \frac{eB}{c}\tilde{x}\hat{y}) \cdot \frac{1}{\sqrt{V}} \sum_{q,\alpha} c\sqrt{\frac{\hbar}{2\omega}}\vec{\epsilon}_{\mathbf{k}}^{(\alpha)} e^{-i(k_y y+k_z z-\omega t)} \\ &= -\frac{e\hbar}{2\sqrt{mV}} \sum_{q,\alpha} \sqrt{\frac{\omega_c}{\omega}} e^{-i(k_y y+k_z z-\omega t)} \\ &\quad \times(-i(b-b^\dagger)\hat{x} + (\sqrt{\frac{2}{\omega_c\hbar}}p_y - (b+b^\dagger))\hat{y} + (\sqrt{\frac{2}{\omega_c\hbar}}p_z)\hat{z}) \cdot \vec{\epsilon}_{\mathbf{k}}^{(\alpha)}. \end{aligned} \tag{2.21}$$

Now we can algebarically solve for emission rates. Since there is only a first-order b or $b^\dagger$ terms in this Hamiltonian, we know by selection rules and energy conservation that a magnetized particle with Landau level $|l>$ can either emit a photon and enter transition to a $|l-1>$ state or absorb a photon and transition to an $|l+1>$. The related rates can be given as,

$$\Gamma_{em} = \frac{2\pi}{\hbar} | \left\langle k_y', k_z', l-1 | H_{\text{int}} | 0, 0, l \right\rangle |^2 D_E, \tag{2.22}$$

$$\Gamma_{abs} = \frac{2\pi}{\hbar} | \left\langle k_y', k_z', l+1 | H_{\text{int}} | 0, 0, l \right\rangle |^2 D_E. \tag{2.23}$$

Explicitly solving for the differential emission rate in a cavity with n_γ photons in the $-\mathbf{k}$ mode, with energy and momentum conservation in the $\hat{y}$ and $\hat{z}$ directions, Eq. 2.22 becomes,

$$\Gamma_{em} - \Gamma_{abs} = (l(n_\gamma+1) - (l+1)n_\gamma)\frac{2\pi e^2\hbar}{mV}\frac{\omega_c}{\omega}\cos^2\theta D_{E,\Omega}, \tag{2.24}$$

$$\text{where } \omega = \frac{\sqrt{1+\frac{2\hbar\omega_c\cos^2\theta}{mc^2}}-1}{\frac{\hbar\cos^2\theta}{mc^2}} \approx \omega_c. \tag{2.25}$$

Here, the density of final states in a differential solid angle $d\Omega$ of the photon momentum vector is,

$$D_{E,\Omega} = \frac{\omega^2 V}{(2\pi)^3\hbar c^3} d\Omega. \tag{2.26}$$

Integrating over the solid angle, we get a cooling rate,

$$\begin{aligned} \dot{U} &= -\int \hbar\omega(\Gamma_{em} - \Gamma_{abs}) d\Omega \\ &= \frac{e^2\omega_c^2((n_\gamma - l)\hbar\omega_c)}{3\pi mc^3}. \end{aligned} \tag{2.27}$$

This rate is identical to the classically expected Larmor radiation rate with thermalization of the particle relative to the cavity taken into account using equipartition.

Cyclotron Emission in a Long, Cylindrical Cavity

Using the same technique as in the free particle case, we calculate expected emission rates in a long, cylindrical cavity. In this case, we use "long" to mean that the cavity is long enough to assume a continuous distribution of axial modes. We start by simplifying the **u** operators in Eq. 2.7 using the identities in Eq. 2.9,

$$\begin{aligned}
\mathbf{u}_{mnk_z(\mathrm{TE})} &= \sqrt{\frac{1}{2\beta'_{mn}}}\Big(-i(J_{m-1}(\gamma'_{mn}\rho) + J_{m+1}(\gamma'_{mn}\rho))\hat{\rho} \\
&\quad (J_{m-1}(\gamma'_{mn}\rho) - J_{m+1}(\gamma'_{mn}\rho))\hat{\phi}\Big) \\
&\quad \times e^{im\phi}\sin{(k_z z)} \\
\mathbf{u}_{mnk_z(\mathrm{TM})} &= \sqrt{\frac{c^2}{2\omega^2\beta_{mn}}}\Big(k_z(J_{m-1}(\gamma_{mn}\rho) - J_{m+1}(\gamma_{mn}\rho)))\sin{(k_z z)}\hat{\rho} \\
&\quad -ik_z(J_{m-1}(\gamma_{mn}\rho) + J_{m+1}(\gamma_{mn})\rho))\sin{(k_z z)}\hat{\phi} \\
&\quad +\gamma_{mn}J_m(\gamma_{mn}\rho)\cos{(k_z z)}\hat{z}\Big) \times e^{im\phi}.
\end{aligned} \tag{2.28}$$

Here, we again take advantage of the fact that the Larmor radius is much smaller than the radiation wavelength. Since $J_m(r)$ behaves like an r^m polynomial as $r \to 0$, and the $e^{im\phi}$ term effectively introduces a (m/r) term to the radial scaling of fields near the origin, we can conclude that there are no higher-order field contribution terms in the center of the trap greater than what one would expect from the effective wavelength. The wavefunction of the electron is presumed to be localized since the particle is assumed to be gyrating about a magnetic field line at a radius R. In this case, a dipiole approximation can be made, replacing $\rho \to R, e^{im\phi} \to 1$ in the above **u** and overlaping the $\tilde{x}, y$ co-ordinates from the particle operators with the local r, ϕ coordinates of the cavity. We use this condition to guide the following heurisitic calculation.

The density of final states in the cavity, emitting into a particular mode is given as,

$$D_E = \frac{\omega}{\sqrt{\omega^2 - \gamma^2 c^2}}\left(L/2\pi\hbar c\right). \tag{2.29}$$

From this, we have $\Gamma_{\mathrm{em}} - \Gamma_{\mathrm{abs}}$ rates into particular n, m TM and TE modes,

$$\Gamma_{\mathrm{TE}} = (l - n_\gamma)\frac{e^2}{R_w^2 m\beta'_{mn}c}\frac{\omega_c}{\sqrt{\omega_c^2 - {\gamma'}_{mn}^2 c^2}}J_{m-1}^2(\gamma'_{mn}R), \tag{2.30}$$

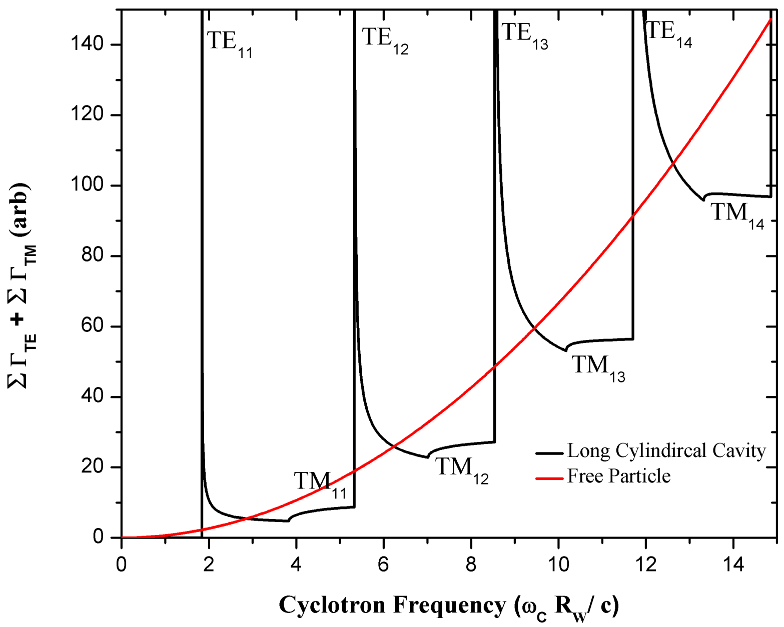

Figure 2.1: Cyclotron emission rate in a long, cylindrical cavity. The curve is compared to the free particle emission rate. Note that moving in the positive direction along horizontal axis is the equivalent operating in higher magnetic fields. TE modes produce obvious resosnances, while TM modes make a first-order contribution when there is a signficant axial component to the mode.

$$\Gamma_{\text{TM}} = (l - n_\gamma)\frac{e^2}{R_w^2 m \beta_{mn} c}\frac{\sqrt{\omega_c^2 - \gamma_{mn}^2 c^2}}{\omega_c} J_{m+1}^2(\gamma_{mn} R). \tag{2.31}$$

In the limit of $R \to 0$ we take the highest order of the Taylor expansion to approximate the above Γ as,

$$\Gamma_{\text{TE}} = (l - n_\gamma)\frac{e^2}{R_w^2 m \beta'_{mn} c}\frac{\omega_c}{\sqrt{\omega_c^2 - \gamma'^2_{mn} c^2}}\left(\frac{(\gamma'_{mn} R/2)^{|m-1|}}{\Gamma(|m|)}\right)^2, \tag{2.32}$$

$$\Gamma_{\text{TM}} = (l - n_\gamma)\frac{e^2}{R_w^2 m \beta_{mn} c}\frac{\sqrt{\omega_c^2 - \gamma_{mn}^2 c^2}}{\omega_c}\left(\frac{(\gamma_{mn} R/2)^{|m+1|}}{\Gamma(|m|)}\right)^2. \tag{2.33}$$

One interesting feature is that if we expect the plasma to be in the center of the trap ($R \approx 0$), the only modes with significant contributions are TE $m = 1$ and TM $m = -1$ modes.

Other modes are unavailable for cooling since they don't have a significant contribution in the center of the trap. Under this approximation, we have a cooling rate per particle of,

$$\dot{U} \simeq \sum_{\{n|\gamma'_{1n}c\leq\omega_c\}} \hbar\omega_c\Gamma_{\mathrm{TE};1n} + \sum_{\{n|\gamma_{1n}c\leq\omega_c\}} \hbar\omega_c\Gamma_{\mathrm{TM};-1n}. \tag{2.34}$$

The effective emission rate for magnetized electrons where the cyclotron emission wavelength is the same order as the cavity size is shown in Fig. 2.1. The sharp peaks correspond to TE cavity modes, while the smaller steps are TM cavity modes. The essential feature of this system that makes these lineshapes possible is the density of states; having more states available for emission in the cavity corresponds to a faster cyclotron cooling rate. Fig 2.1 resembles calculations found in Kleppner's paper on inhibited emssion, using a different geometry [47].

Finite Cavity Emission Rates

Until this point, we have assumed that the length of the cavity is long, and consequently modes are densely distributed relative to the linewidth of the modes. However, for our cavity, this is not the case since the cavity has a finite length, only an order of magnitude greater than the diameter, resulting in a discrete set of modes. The quality factor of the modes, resulting from small, but finite, resistance of the electrodes can influence emission behavior. In this regime, the density of modes is expected to take the form of a series of peaks with Lorentzian distribution, with the effective linewidth, $\gamma = \omega/2Q$, determined by the quality factor, Q, of each mode. This results in a revision to Eq. 2.29,

$$D_E = \frac{(\gamma/2\pi\hbar)}{(\omega-\omega_0)^2 + (\gamma/2)^2}, \tag{2.35}$$

for each individual cavity mode. Note that the finite Q of the cavity mode shifts the resonant frequency, ω_0, from the solution given by the ideal cylindrical cavity by $\Delta\omega = -\omega/2Q$.

An example of the new effective cyclotron emission rate is solved numerically in Fig. 2.2. Again, the features of this curve are dominated by the density of states; since there is no longer a continuous distribution, the cooling rates are largely determined by the sharpness of the peaks. The background emission rate is due to contributions from lower TE and TM modes that are expected to have relatively low Q due to scattering in the cavity geometry.

In addition, the z-dependent terms from Eq. 2.28 can no longer be averaged due to finite boundary conditions, so each mode has an emission rate proportional to $\sin^2(k_z z)$, where k_z is now only permitted to have values $n\pi/L$. This can have a significant effect on electrons that are tuned to a mode with low k_z, but are only trapped along a small axial length.

The consideration of doppler broadening of the interaction peak due to finite temperature distributions is outside the scope of this thesis, however it is expected to act as a convolution

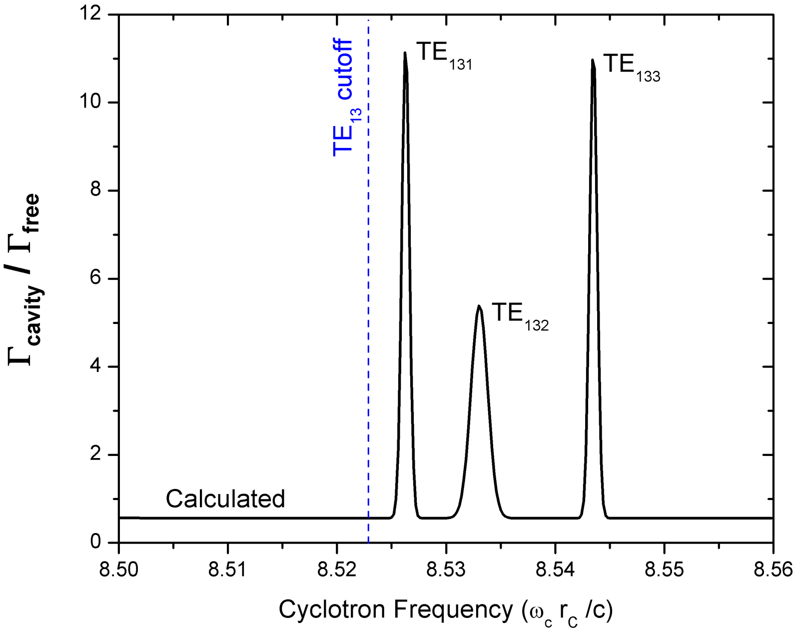

Figure 2.2: Numerically estimated cyclotron emission rates relative to freespace cooling rate in a high-Q, finite cavity near the TE_{13} cutoff, using Q's measured for modes in our cavity and a long plasma assumption. In this case, modes are sparsely distributed so that line widths do not typically overlap. The cyclotron frequency is tuned by adjusting the solenoid magnetic field. This model is consistent with cavity-coupling behaviors observed by Hanneke. [38]

with the emission rate of Γ, effectively broadening the peaks due to the axial contribution to the cavity mode and therefore reducing Q.

Quantum Mechanical, Low-T Corrections

For an ensemble of electrons, corrections are necessary to the effective cooling rate for low-temperature ($k_B T \sim \hbar\omega_c$). Assuming a Boltzmann distribution, the density matrix for a thermal ensemble can be written as,

$$\hat{\rho} = \sum_{l=0}^{\infty} \frac{\exp(-l\hbar\omega_c/k_B T)}{Z} \left|l\right\rangle\left\langle l\right| . \tag{2.36}$$

Here $Z = 1/(1 - \exp(-\hbar\omega_c/k_B T))$ is the partition function of the distribution of a harmoinc oscillator. Noting that the emission rates from Eq. 2.33 depend on the difference between the electron and cavity the harmonic oscillator states, we can condense the cavity geometry and coupling information into a constant, Γ_0, such that,

$$\Gamma = (l - n_\gamma)\Gamma_0. \tag{2.37}$$

Assuming the electromagnetic cavity is strongly coupled to a thermal bath of temperature T_0, the expecation value of the emission rate, $\langle\Gamma\rangle$ over the entire ensemble becomes,

$$\langle\Gamma\rangle = \sum_{l,n=0}^{\infty} \langle l| \frac{\exp(-n_\gamma \hbar\omega_c/k_B T_0)}{Z_\gamma}(l - n_\gamma)\Gamma_0 \hat{\rho}\,|l\rangle. \tag{2.38}$$

Simplification of this expression yields,

$$\langle\Gamma\rangle = \frac{\exp(\hbar\omega_c/k_B T_0) - \exp(\hbar\omega_c/k_B T)}{(\exp(\hbar\omega_c/k_B T_0) - 1)(\exp(\hbar\omega_c/k_B T) - 1)}\Gamma_0. \tag{2.39}$$

Intuitively, this term represents the fact that energy is transported in $\hbar\omega_c$ packets. Since there is a ground state for these distributions, emission becomes statisitically inhibited in the limit that $\hbar\omega_c \sim k_B T_0, k_B T$.

Other considerations

Since the plasma size is typically smaller than a wavelength of the cyclotron emission, it is possible that there are non-linear coherence effects in electron emission when many particles are stored. In particular we note that Dicke superradiance may play a role in the emission and absorption rates of particles, allowing emission of the ensemble to scale as the number of particles squared [19]. This is outside the scope of this thesis, but may play an imporant role if cavity saturation, discussed in the next section, fails to predict cooling rates of many-electron systems accurately.

2.2 Cavity Mode Saturation Effects

While working with ALPHA, I developed a mechanism that may partially explain some of the anomalously warm plasmas which are seen in non-neutral plasma experiments. The mechanism is a bottleneck effect, caused by the coupling chain required to remove energy from the electromagnetic cavity. Cooling in the cavity is dominated by cyclotron motion, as discussed in the previous section, where energy is radiated into the electromagnetic field. This radiation can be absorbed by the resistive walls of the cavity or resonantly reabsorbed back into the confined electrons. In a regime where cavity modes are not dense, that is when the cyclotron radiation has only one or less accessible cavity mode on average, placing too many particles in the cavity can lead to saturation of the the cavity mode resonant with cyclotron motion, impeding the cooling rate of particles in the system. Below is a simple model derivation that illustrates this effect and connects between the limit of large and small numbers of electrons.

In Sec. 2.1, we found that if electrons are placed in a cavity, they will emit radiation at a rate dependant on cavity geometry. More specifically, using Eq. 2.30, we find that the emission rate is also proportional to the term $(l - n_\gamma)$, or the difference between the Landau level of the particle and the number of photons in the cavity. In other words, the emission rate is proportional to the difference of transverse energy in the particle and energy stored in the cavity mode.

Let U_i be the energy of particle i, and U_C be the energy associated with the cavity mode. The cavity mode is coupled to an external environment acting as a heat bath with temperature $T_0 = U_0/k_B$. Assuming that the longitudinal motion thermalizes relatively quickly with transverse motion, the energy transport of this system can be condensed into a set of equations,

$$\begin{array}{rcl} \partial_t U_C & = & \kappa_Q(U_0 - U_C) + \sum_i \kappa_i(U_i - U_0) \\ \partial_t U_i & = & \kappa_i(U_C - U_i) \end{array} \tag{2.40}$$

The coupling constants κ_Q and κ_i are given by an effective Q of the cavity modes and the coupling rate of the particles to the cavity modes. Since collisions between particles conserve energy and particles are identical, the indices for particles can be reordered without loss of generality. To give some intuition, this system is analogous to a series of harmonic oscillators (electrons), coupled to a single harmonic oscillator with dissipation (cavity mode). Finding a cooling rate is equivalent to solving for the rate at which energy is dissipated by this system.

Using the substitution $\tilde{U_i} = U_i - U_0$, the time evolution operator can be written as,

$$\frac{\partial}{\partial t}\begin{pmatrix} \tilde{U}_C \\ \tilde{U}_1 \\ \tilde{U}_2 \\ \vdots \\ \tilde{U}_N \end{pmatrix} = \begin{pmatrix} -\kappa_Q - \sum \kappa_i & \kappa_1 & \kappa_2 & \cdots & \kappa_N \\ \kappa_1 & -\kappa_1 & 0 & & 0 \\ \kappa_2 & 0 & -\kappa_2 & & 0 \\ \vdots & & & \ddots & \vdots \\ \kappa_N & 0 & 0 & \cdots & -\kappa_N \end{pmatrix}\begin{pmatrix} \tilde{U}_C \\ \tilde{U}_1 \\ \tilde{U}_2 \\ \vdots \\ \tilde{U}_N \end{pmatrix} \tag{2.41}$$

The cooling behavior is tied to the slowest rate in the system, so we can find the cooling rate of the system solving for the lowest eigenvalue. The eigenvalue solutions to this equation are given by the characteristic polynomial of this operator,

$$(\lambda + \kappa_Q + \sum_i \kappa_i)\prod_i(\lambda + \kappa_i) + \sum_i(\kappa_i^2 \prod_{i\neq j}(\lambda + \kappa_j)) = 0 \tag{2.42}$$

Since electrons are interchangeable, we assume that the coupling constants from electrons to the cavity are all equal. Allowing $\kappa_i = \kappa$ for all particles, the characteristic polynomial becomes,

$$(\lambda + \kappa)^{N-1}(\lambda^2 + (\kappa_Q + (N+1)\kappa)\lambda + (\kappa_Q\kappa)). \tag{2.43}$$

In this case, the eigenvalues, are:

$$\lambda = -\kappa, \frac{1}{2}\left(-(\kappa_Q + (N+1)\kappa) \pm \sqrt{(\kappa_Q + (N+1)\kappa)^2 - 4(\kappa_Q\kappa)}\right).$$

There are two obvious regimes of interest in this problem. The first limit, $N\kappa \gg \kappa_Q$, describes a saturated cavity and has a thermalization rate of $2\kappa_Q/N$. Here, energy is quickly distributed equally amongst the photon modes of the cavity and electrons; however the dissipation of energy in the system is bottlenecked since it must leave through the cavity mode. The alternative case, where $N\kappa \ll \kappa_Q$, describes when the cavity is very tightly coupled to the thermal bath. In this case, the thermalization rate approaches κ; the cooling is cyclotron emission limited.

A similar saturation behavior was noted by Tan and Gabrielse in an experiment with fewer electrons and smaller trapping volume [75, 76]. However, the scaling behavior for saturation described in their paper is described by a parameter where $N^2\kappa/\kappa_Q \geq 1$ when saturation is important. This saturation scaling relies on superradiant behavior when the field is sufficently homogeneous due to coherent stimulation of cyclotron emission. In this case, it is expected that $\kappa \propto N$ rather than following single-particle motion behavior, however κ must then also include a correction term for the effective reduction in Q. This can cause potentially large shifts of the cavity mode frequency and mode-splitting due to coherent normal mode behavior of the now strongly-coupled cyclotron-cavity system, an effect demonstrated in atomic systems [53]. The details of this behavior is outside the scope of this thesis, but can have a potentially large influence on the cooling behavior.

In a confined non-neutral plasma, the cooling rate and cavity coupling both depend on the geometry of the cavity. In particular, in the sparse mode regime the cooling rate derived from 2.35, is expected to scale as $\kappa \propto 1/Q$ near a resonance. However, natural linewidth of the cavity mode also implies that $\kappa_Q \propto Q$. These effects compete when there a large number of particles and Q is large: although electrons become more strongly coupled to the cavity, the dissipation of energy is into the electrode walls is weaker.

We can perform a quick estimate for cavity saturation threshold in the CERES experimental cavity. The effective Q of cavity modes is inferred by a measurement of the linewidth of the modes with Agilent network analyzer. Modes in the cavity typically have $Q \sim 10000$. Operating at fields near 1.0T, the cooling rate of a single particle with cavity enhancement is $\kappa \sim 3\text{s}^{-1}$. Given that the cyclotron mode at 1T has $\omega_c = 176\text{GHz}$, this would imply a saturation limit near $6 \cdot 10^6$ confined particles.

In a more practical sense, tuning particle number and the cavity quality factor can be an important aspect of optimizing cooling rates in a cavity. If the Q is too large for the number of stored electrons, radiation is effectively trapped in the cavity long enough that it can get reabsrobed by the electrons. If Q is too small, the modes of the cavity will not couple to the electrons strongly, and the electrons will not exhibit enhanced cooling as shown in the previous section. Placing too many electrons in a cavity reduces the range in which particle can cool quickly, since it reduces the threshold for the bottleneck behavior. This is an important consideration for antihydrogen synthesis experiments, such as ALPHA, where experimental sequences typically store 10^7-10^8 leptons in a cavity at time for sympathetic cooling and antiproton-positron recombination.

Chapter 3

The CERES Apparatus

This chapter describes the structure of the Cold Electron Research (CERES) apparatus, that I constructed at Berkeley to study cooling behavior described in chapter 2. The device was conceived as an experimental platform for studying cyclotron-cavity coupling and prototyping various lepton plasma diagnostics and procedures for use in the ALPHA experiment. As such, many of the features are similar to ALPHA's structure. Plasmas are confined in a cylindrical Penning trap, placed in the bore of a large superconducting solenoid magnet. Similarly, electrodes are cooled to cryogenic temperatures, so that confined plasmas are expected to equilibrate to lower temperatures. In both systems electrons are generated by a heated filament and plasma diagnostics are primarily achieved using a microchannel plate (MCP) imaging assembly.

The device is specialized for cold, electron plasma studies. CERES has reduced cavity complexity so that modes are easier to predict and match experimentally. Electrode design was modified to ensure higher Q values in the cavity region. Two cryogenic doors were introduced on either side of the cavity region to ensure that the experimental region fully isolated from external radiation. In an effort to reduce operating costs, the cryogenics system had to be designed to reduce liquid helium consumption, introducing a closed-loop cryocooler refrigeration system for use in cooling the experimental region. A sectioned view of the apparatus is shown in Fig. 3.1.

The majority of sections in this chapter describe subsystems of the CERES apparatus, focusing on the design and construction of the cavity as well as a description of detection methods. The final section describes the characterization of 3D-printed metal components in our device, which we found useful in prototyping pieces that were difficult to machine using traditional fabrication methods.

3.1 The Cavity Structure

In order to measure the resonant-cavity phenomenon discussed in Chapter 2, an electromagnetic cavity was built that was capable of generating electrostatic potentials to confine and manipulate electrons in a high magnetic field. The cavity, located at the center of a long superconducting magnet, has a long cylindrical geometry with 40.00mm diameter and 58.70 cm long, coaxial with the magnetic field geometry. The cavity is a series of 18 stacked, controllable cylindrical electrodes and grounded end electrodes with closable apertures on the ends. The cavity is mounted inside an ultrahigh vacuum (UHV) chamber with oxygen free copper (OFHC) walls for heatsinking. Copper flanges capping the ends of the experimental region in the UHV chamber walls act as structural and thermal support for the electrode stack. The flange also prevents signals and blackbody radiation external to the experimental region from interacting with the cavity electrodes. The cavity structure is shown in Fig. 3.2.

Electrodes

Electrodes in the device are machined out of OFHC copper and plated with a 70μin (1.8μm) layer of gold. The gold serves to prevent oxidation of the surfaces as well as provide excellent conductivity for electrical connections. Individual electrodes are 25.40mm long with a 40.00mm inner diameter. A flat surface with threaded holes is provided on the exterior to attach signal cables to apply voltages to the electrodes. Signal cables are coaxially shielded KAP50 cable; the shield covers the entire length of the wire except for the last 2-3cm on both the isolation vacuum feedthrough and electrode sides. The signal cables, as the most thermally conductive connection to the electrodes, are also the primary heatsinks for the electrode stack at cryogenic temperatures. The shielding for the cable is directly soldered onto the copper flange, to ensure high thermal conductance.

The electrodes interlock with each other using a tongue-in-grove design, preventing leaks of cavity mode energy to the rest of the vacuum chamber. Calculations done in COMSOL show a quality factor for modes, $Q > 10^6$ using this geometric design with a perfect conductor. Electrodes are aligned and isolated using a set of six evenly-spaced ϕ0.040" ceramic rods and spacers on each side of the electrode. The rods fit into alignment holes in the tongue-and-grove region; the gap distance between electrodes is 0.64mm. Electrodes are grouped into modules of six to allow for rapid interchange of cavity components to generate different cavity geometries during servicing. Modules are held together using a stainless steel (Alloy 316LN) bracing structure that interlocks at the ends.

One of the electrodes is split into six azimuthal components. Using these electrodes, torque is applied to plasmas by applying a rotating radio-frequency electric field to nearby trapped plasmas. This allows us to radially compress and expand trapped plasmas in experiments in what is known as the “rotating wall” technique. The sectors are held fixed by a set of PEEK spacers wedged the external azimuthal gaps, mounted on an stainless ring. Small kapton sheets prevent rotation and accidental shorting of the individual sectors. None of the

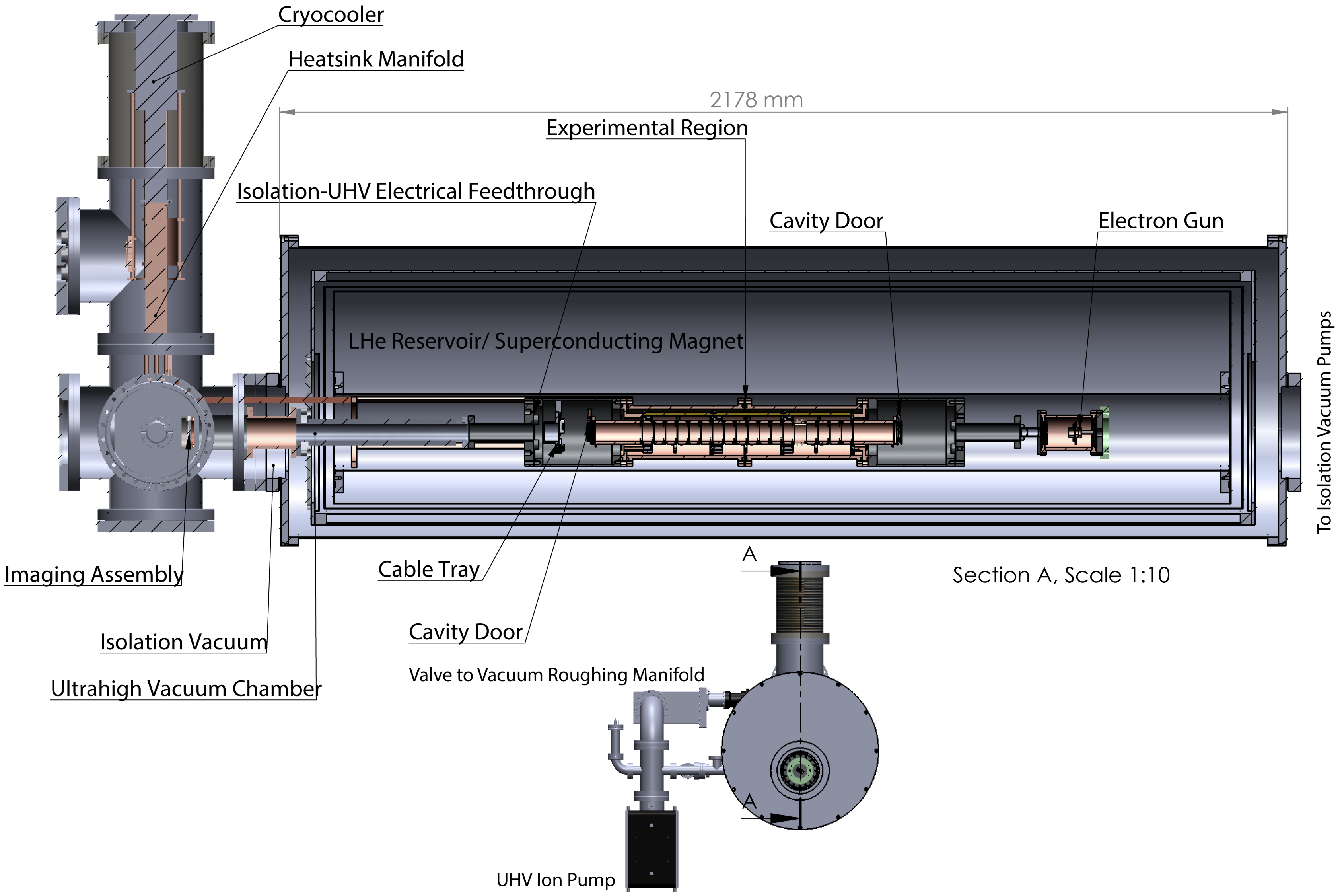

Figure 3.1: Sectioned view of the CERES apparatus.

insulators has direct exposure to the interior of the cavity, so there is very little reduction in the Q of cavity modes in this region.

Cavity Doors and Integrated Detectors

The ends of the cavity are capped by long electrodes grounded to the vacuum chassis with doors that are capable of opening when either injecting plasmas the cavity region or extracting plasmas to the imaging detector. When closed, the doors seal the interior of the electrodes as an electromagnetic cavity. Since conventional motors do not work under a high magnetic field and cryogenic vacuum environment, we use a pair of induction coils on each door to open them in the presence of a high magnetic field. Two coils are required to move the door, a main coil on the door and a secondary coil on the lever arm. Under an external magnetic field, the coils are energized in sequence to torque the door open and closed. The doors are mounted such that they open horizontally to prevent the need to actively energize coils during operation. The induction coils for the cavity doors are powered by programmable power supplies that are triggered through software. The in-vacuum leads for these coils are 34AWG copper wire instead of copper-backed superconducting cable to reduce ohmic heating of door during operation, as the majority of the superconducting lead was not below critical temperature. The cavity doors hang on a slightly undersized Vespel hinge to prevent sticking during cryogenic operation. The door frame was 3D-printed in sterling silver, which was found to be vacuum compatible as discussed in Sec. 3.9.

The doors include basic detectors for charge collection and orientation. There is a hall probe (Cryomagnetics HSU-1) mounted onto the face of each door that can be used to measure the magnetic field strength along each door axis with 100G resolution. This can also be used to find the doors' positions when the drive coils are turned on. The charge collection is achieved using thin (.020"), gold-plated copper sheets mounted onto the doors. Isolation of the Faraday cup is achieved with a Kapton sheet standoff.

The cavity door on the side of the electron source has a outward-facing Faraday cup that can be used for measuring electron flux from the source. By adjusting the DC bias voltage on the cup, we are also able to characterize the energy distribution of injected electrons.

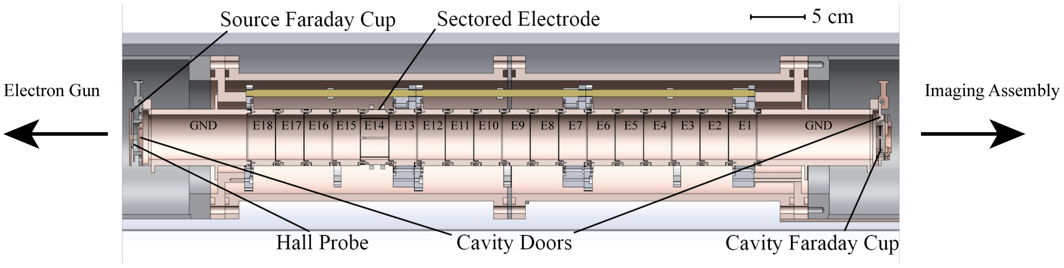

Figure 3.2: Experimental Cavity Region.

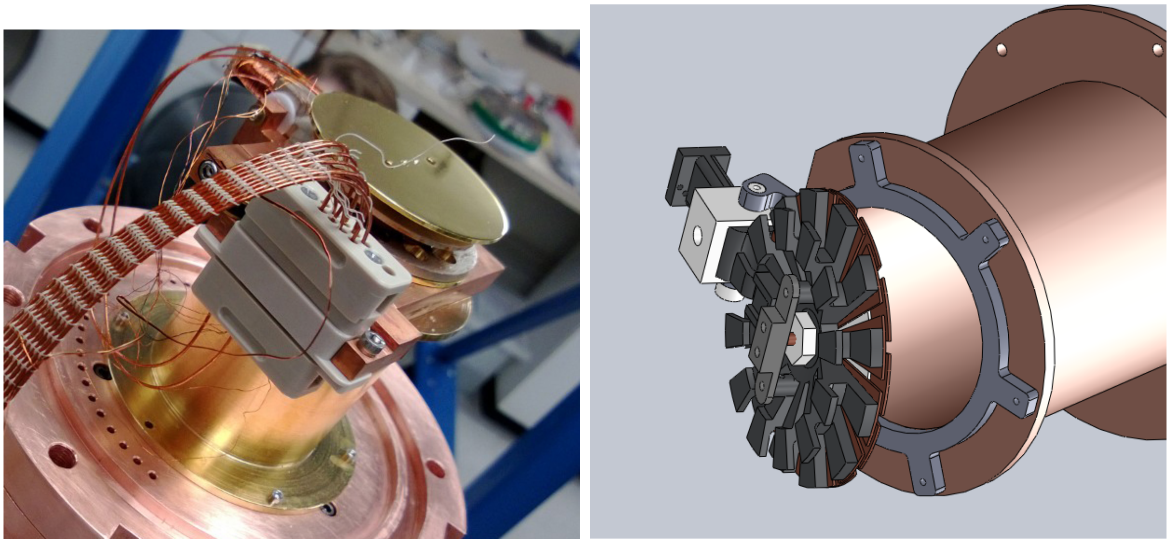

Figure 3.3: Cavity Door from 2012 (*left*) on the electron source side. This door includes the back-facing charge collector (gold plate) and the Hall probe (epoxied to the rear of the charge collector). The current version of this device (*right*) features radial slices in conducting plates in the assembly to reduce inductive forces from eddy currents that were slowing door movement in the high field.

On the detector side of the cavity, there is an inward facing Faraday cup embedded in the door in order to measure charge extractions without opening the cavity. The signal cable for the cup is connected to a voltage preamplifier and capacitor that is used to destructively measure the time-resolved charge deposited on the charge collector. This information can be used to determine total charge of a trapped plasma. Isolation of the Faraday cup is provided by a vespel channel and standoffs.

It was found during the course of operation that the doors were opening slower than expected, an effect we suspected was due to eddy currents driven by the motion of the door in the high background magnetic field since the door in a cryogenic state was highly conductive. A new version of the door was built such that both the door frame and Faraday cup has radial slices passing them to reduce the eddy currents produced when opening and closing the doors.

Electromagnetic Mode Structure

Electromagnetic modes in a cylindrical cavity can be represented in a basis of transverse electric (TE) and transverse magnetic (TM) modes. Since there is a strong magnetic field along the axis, only the TE modes resonantly contribute to electron cooling. These TE modes are identified using characteristic azimuthal, radial, and axial numbers, $m, n,$ and p, and have frequencies,

Mode n, p	Calculated Freq.	Measured Freq.	Measured Q
1, 1	4.4047 GHz	4.3942 GHz	11,000
1, 2	4.4411 GHz	4.4301 GHz	-
1, 3	4.5012 GHz	4.4902 GHz	-
2, 1	12.7233 GHz	12.7043 GHz	21,000
2, 2	12.7360 GHz	12.7270 GHz	-
2, 3	12.7570 GHz	12.7548 GHz	-
3, 1	20.3675 GHz	20.3407 GHz	29,000
3, 2	20.3754 GHz	20.3568 GHz	9,400
3, 3	20.3886 GHz	20.3818 GHz	21,000
4, 1	27.9286 GHz	27.8793 GHz	56,000
4, 2	27.9344 GHz	27.8885 GHz	-
4, 3	27.9440 GHz	27.9089 GHz	-

Table 3.1: Measured TE$_{n1p}$ Cavity Mode Characteristics. Measured modes are at a lower frequency from the cylindircal geometry due to the finite Q associated with skin-depth penetration and the perturbation of the cavity walls due to electrode gaps.

$$\omega_{mnp} = c\sqrt{\frac{x'^2_{mn}}{R^2} + \frac{p^2\pi^2}{L^2}}, \tag{3.1}$$

where x'_{mn} is the n^{th} root of the first derivative of the Bessel function, $J'_m(x)$, R is the radius of the cavity, p is a positive integer, and L is the axial length of the cavity. These modes, and their interaction with electron motion, are discussed in detail in Chapter 2.

These modes were directly measured in a cavity of 18-electrodes and a pair of endcaps using an Agilent N5244A network analyzer to supply and detect modes in the cavity. This was done to characterize to frequency expected losses and scattering in the cavity modes. Modes in the system can be identified as peaks in a frequency-chirped spectrum of the analyzer. Since the majority of the particles are trapped near the center of the electrodes, the modes of interest to us must have strong electric fields at the trap center. The only modes that satisfy this condition have $m = 1$. These can be easily picked out in the spectrum by placing a small glass bead on a wire that passes down the center of the electrodes. Moving the z-position of the bead will shift the mode frequency of all $m = 1$ modes; the number of shifts as the bead moves across the entire length of the cavity gives the p-number of the mode. The modes and their measured qualities are shown in Table 3.1. The quality of the mode is measured from the 3dB-width of the mode's lineshape.

Cryogenic Cooling

The apparatus is cryogenically cooled in order to maintain superconductivity in the solenoid magnet and to keep the environment of the experimental region cold. During operation, the superconducting magnet is immersed in liquid helium to keep the material below the critical point. The helium dewar is isolated using multilayer aluminized mylar heatshielding and an isolation vacuum. The central bore of the magnet dewar is cold, reducing the heatload due to blackbody radiation on the experimental region.

In order to cool the electron plasma, emitted radiation must be transfered into the cavity walls, thermalizing the plasma to its environment. The cavity electrodes and experimental region are actively cooled using a Sumitomo RDK-415 cryocooler to pump 1.5W of heat from the cavity region. Heat is transported along the axis of the bore, to the cryocooler, using copper rods attached to the exterior of the UHV chamber. The UHV chamber is decoupled from the helium reservoir, cooling the superconducting magnet to reduce liquid helium consumption in the system. Temperatures of different regions of the chamber are monitored using four-point resistance measurements across Lakeshore CERNOX sensors. The final, minimum temperature of the cavity electrodes, after cooling, was found to be 14K.

Copper joints in the heatsinking manifold are compressed together using threaded fasteners, with .004" indium foil sheets placed between the compression surfaces to ensure high-thermal conductivity at the joints.

Heatloads to the experimental region from conduction are estimated to be 500mW, mostly due to structural connections with the liquid nitrogen chamber made with stainless steel. Since the trap is only observed to cool to 14K, there may be a poor compression connection in some location, or blackbody radiation from the walls of the external chamber may be leaking into the bore-region at a higher rate than expected from clearance holes in the shielding to allow for tuning of the UHV chamber position in the bore. Contacts with the electrodes may also require improvement since the cabling providing much of the cooling power to the electrode material is sunk through an thin isolating Kapton sheet to provide electrical isolation from the chassis.

3.2 Electrode Control System

Electrode signals are controlled through a realtime National Instruments PXI system. This system determines the timing, triggering, and electrode signals that are used in the experiment. Experimental sequences are written on a client computer, compiled, and uploaded to the DAC and FPGA cards using the same software suite developed for ALPHA. A PXI-7811R FPGA controls the digital input/output lines and acts as a timer for a pair of PXI-6733 analog output cards. Digital signals, used for triggering various instruments, can be driven at 37.5ns intervals, matching the cycle clock of the FPGA. Analog signals are preloaded into the PXI-6733 memory and stepped using a FPGA digital line. The analog output is used to bias the electrodes, and has a maximum sampling rate of 1MS/s.

The analog signals are initially sent through a high-bandwidth, unity-gain amplifier stage to buffer the control circuit from high-voltage amplifier feedback and supply sufficient current to bias electrodes when the high-voltage amplifiers are not used. At this point, signals

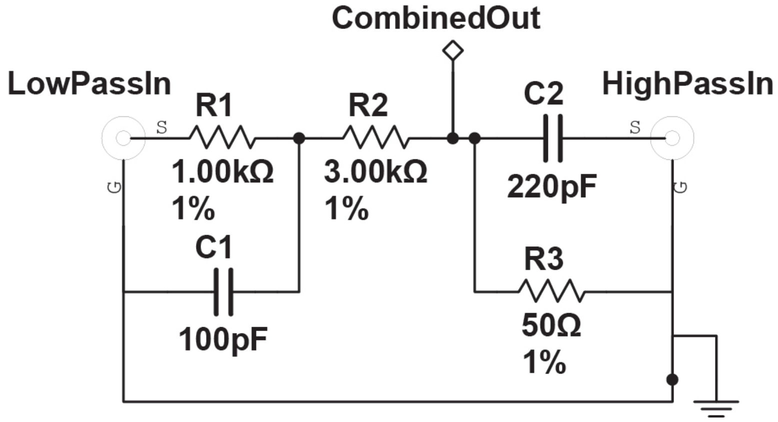

Figure 3.4: Circuit diagram for electrode filter circuit. There are two inputs into the circuit; the low-pass filter is used for the computer-controlled, amplified sequenced voltages while the high-pass filter is used for sending RF signals to the electrodes. An optional inductor can be placed between channels to prevent diocotron decay in the sectored electrode.

are broken into individual coaxial cables to reduce noise coupling into the lines. Signals are amplified and transmitted through a passive low-pass filter shown in Fig. 3.4. Radio-frequency signals produced by waveform generators can be trigged digitally from the PXI system and passed to the electrode using the high-pass filter. In particular, we utilize a six-phase custom RF generator to torque plasmas for compression. The combined signal is sent to the electrodes through a vacuum feedthrough. NbTi superconductor leads are used in the isolation vacuum to prevent thermal transport from the outside, although due to the thermal gradient they are not superconducting for the entire length of the cable.

3.3 Electron Imaging Detector

Trapped plasmas can be imaged by extracting the plasma along magnetic field lines onto an imaging detector located 860mm downstream from the cavity in a fringe magnetic field. Since charged particles remain highly magnetized during extraction, they are locked to the field lines such that the radial profile of the trapped plasma is preserved during extraction. From the topology of the field lines during extraction, we infer the image preserves the profile shape while magnifying the size of the plasma by $\sqrt{B_0/B_i} \sim 9$, where B_0/B_i is the ratio of the magnetic field in the cavity to the field at the detector. Although this is a destructive measurement, it allows us to retrieve a high resolution snapshot profile.

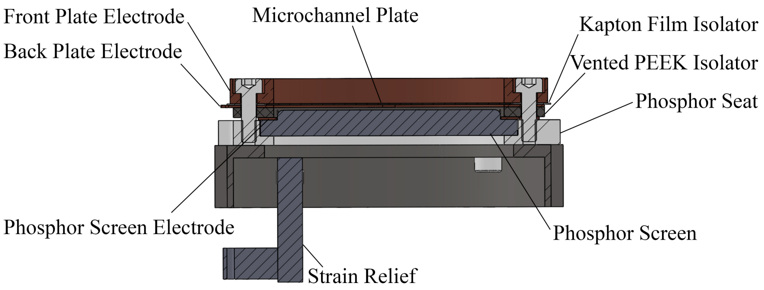

Figure 3.5: Schematic of the Microchannel Plate Imaging Detector Assembly. The plate is held between two annular electrodes isolated by a kapton film sheet. The electrodes are aligned and fastened to a seated faraday cup, the plate offset 1.04 mm above the phosphor surface. Isolation structures and fasteners are made of virgin PEEK for vacuum compatibility.

Electron Amplification

The imaging detector converts incident electrons into a flash of light that can be imaged with a camera. Incident electrons hit small channels on the input side of a microchannel plate (MCP). A electrostatic bias is placed across the the plate to accelerate incident particles. When particles hit the walls of a channel, they eject additional electrons. This results in a cascade of electrons ejecting from the back of the plate, effectively amplifying the charge per incident electron by a factor of up to 5.0×10^4 [5]. Our MCP was a 6μm-pitch, 50mm-diameter, plate manufactured by Photonis, including extended dynamic range and magnesium oxide coatings to improve saturation levels and quantum efficiency of the detector, respectively.

The cascade of electrons is accelerated to a few kilovolts onto a P47 phosphor screen that emits 400nm photons, with 40ns response time, when excited by incident electrons. The phosphor layer is backed by a fiberoptic plate that allows imaging on the back side of the phosphor. Typical electrostatic biases are 1000V across the MCP and 3900V between the back of the plate and phosphor screen. In this configuration, we expect 50 γ/e^- incident on the phosphor screen. The structure of the detector was custom-designed with a reduced profile to fit inside our chamber at a location with moderate field strength ($\sim$ 250G).

The structure of the detector is shown in Fig. 3.5. The assembly required a custom design in order to fit inside the vacuum chamber at the desired fringe field.

Image Capture

Both the ultrahigh vacuum chamber and isolation vacuum behind the detector have vacuum windows, allowing for optical access to the phosphor screen. The image generated on the phosphor screen is captured using a PCO Sensicam QE. The resulting image has a resolution of 50μm per pixel, comparable to the plume radius of ejected electrons from an individual channel. [71] Quantum efficiency of the camera is 40%, with a detection threshold of ~ 4 electrons per pixel. The camera is a low-noise, high-efficiency CCD camera that allows for detection of single electrons with the phosphor screen; given the typical location of the camera 40cm from the phosphor screen, we expect, on average, 600 electrons to be generated on the CCD per incident electron on the detector.

Amplified Faraday Cup

The microchannel plate can also be used as an amplified charge collector, which is especially useful for measurement of low temperatures in plasmas. We can read number of post-amplification electrons from the microchannel plate directly by measuring the voltage change on the phosphor screen as charge is collected. The voltage depends on the capacitance of leads connected to the phosphor screen (1.3nF). However, this signal must be recovered as a pickup from a high-voltage line since the phosphor screen must be biased higher than the back of the MCP to capture ejected electrons. The detector is isolated from the high-voltage power supplies that bias it using a 100mHz filter, filtering the detector from power supply ripple and response. This allows charge accumulation to be read for millisecond-scale extractions. The voltage increase is measured by placing a 100μF high-voltage capacitor between the detector and digitizer, so that the high frequency signal is allowed to pass to the digitizer. A pair of Schottky diodes is used to protect the amplifier circuit from large voltage spikes.

The signal is amplified using a SRS SR560 low-noise preamplifier and read using either a 14-bit,100MS/s PXI-5412 or a 5GS/s Techtronix DPO 5034 scope. This allows for a resolution of about 30 incident electrons on the MCP front plate with 1.2MHz bandwidth. The largest limitation on this method is the supply noise present on the high-voltage line when it is energized.

Phosphor Light Capture

In an effort to reduce the effect of ripple and noise from high voltage supplies on the measurement of electrons incident on the microchannel plate, we have developed a system that measures the light produced by electrons incident on the phosphor screen. This is described in detail in Sec. 4.2.

3.4 Vacuum System

Two volumes of the apparatus need to be evacuated when operating the experiment. The interior vacuum of the trap, that includes the cavity, requires UHV of $< 10^{-9}$mbar to ensure long trapped electron lifetime. Having a background above this threshold will expand the plasma through collisions with the background gas. Outside this vacuum system is an isolation vacuum that is used to keep the experiment and cryogen reservoirs thermally isolated from the room temperature walls.

UHV Vacuum

The UHV vacuum chamber runs through the bore of the superconducting magnet such that the experimental cavity is centered in the homogeneous magnetic field produced by the superconducting solenoid. During operation, the vacuum is pumped by a 150L/s Agilent ion pump attached to the remote roughing manifold. During startup the pump is backed by a 300L/s turbopump and Edwards XDS-35 Oil-Free Scroll Pump. During pumpdown, the gas is vented through the channels at the edge of the imaging detector; it is critical to pump the volume slowly to prevent pressure differentials across the detector's plates.

Since the cavity region of the chamber is cryogenic, the pressure is expected to drop further in the cavity region due to cryopumping (adsorption of molecules onto the walls of the electrodes). The adsorption process can be saturated over long cryogenic periods, resulting in higher background gas densities. This has been observed by preforming a rudimentary mass spectrometry of the background gas on different days of cryogenic operation. We achieve this by intentionally heating an electron plasma to ionize the background; the resulting ions were confined in a Penning trap and identified using a time of flight measurement during an extraction to the multichannel plate. We found that we could reduce background gas by reheating the experimental region to greater than 50K for a day, clearing many of the adsorbed molecules.

Isolation Vacuum

An isolation vacuum surrounds the cryogen dewars and the UHV vacuum. It is necessary to keep these components thermally isolated. The isolation vacuum is evacuated by a Varian Turbo-V 70 backed by a Edwards E2M30. Once pumped to the 10^{-5}mbar range maintained by a 300L/s Varian ion pump. A grounded copper mesh is placed over the ion pump inlet to prevent ion spray damage to exposed surfaces.

3.5 Superconducting Magnet

The homogeneous magnetic field in the experimental region is generated by a superconducting solenoid magnet immersed in a liquid helium bath. The magnet was fabricated by Oxford Instruments using NbTi coils and was previously used for initial antihydrogen generation experiments by the ATHENA collaboration. The magnetic field is homogeneous to 6×10^{-4} of the target field over the central meter of the chamber, with a maximum gradient of 3.6G/cm when operating at 6.0T. There is a 10cm range in the center of the experimental region where the magnetic field is homogeneous to better than 0.1G/cm at 6.0T of the target field. Since the gradient of the field changes depending on the location of the electrons in the trap, the effective width of the cyclotron resonance can be controlled by the location and size of the trapping volume.

The superconducting coil is protected from quenches when energized using a pair of back-to-back external diodes. These diodes are in series with a water-cooled steel pipe, allowing current to be ramped in a controlled manner in the coils over 60 minutes. Internal diodes acting as bypasses were placed by the manufacturer to keep wires from being damaged during the quench ramp-down.

The magnet power supply, a TCR 40T250, is controlled by a computer running a realtime Labview state machine. The maximum current supplied to the magnet is 242A, corresponding to 6.02T field at the center of the device. The supply software is configured to automatically respond to quenches and ramp at the appropriate rates.

It is important that a the magnetic field is aligned with the axis of electrodes, since misalignments can potentially drive instabilities in the trapped plasmas. The magnetic field can be aligned during cryogenic operation by using a custom gearbox drive to shift the angle of the superconductor relative to the mounting platform for the experiment.

3.6 Electron Gun

The electrons in our system are sourced by a filament coated in barium oxide (Kimball ES-015). Electrons are provided by heating the filament and applying an electric field to the surface with a set of planar electrodes on the front and back of the filament. The filament itself is located inside the superconducting solenoid magnet geometry, and so electron trajectories are locked to field lines after emission. This keeps the beam centered radially in the electrodes where electrons can be captured and confined. The filament normally is operated at 1.18A, slightly higher than the recommended operating limits, to compensate for the additional time needed to heat the material from cryogenic temperatures. The filament is generally biased (usually -30V) relative to the chassis of the experiment; it is capable of supplying 5μA of electrons into the confinement region.

Electron Capture

Electrons are captured by manipulation of the electrode potentials when the filament is emitting an electron beam. The beam is blocked from passing through the device by a large negative voltage applied to an electrode. The electron beam has a two stream distribution as electrons are reflected off the potential. There are a variety of potential manipulation schemes possible for loading that we will describe in this section. These schemes can generally be broken into two categories: either cutting a low-kinetic energy ($\sim$ 10eV) beam in the trapping region by raising a confinement potential or making a slower beam ($\leq$ 2eV) and lowering the potential slowly so that collisions in the cross-streaming electron beam will populate the trap. These are known as *cut-trapping* and *pull-trapping* respectively. The effective difference between the two schemes lies in the typical final electron radial distribution, maximum number, and loading stability.

Cut-trapping will typically load electrons at a higher initial linear density and temperature. Using this technique, the electron cloud would often have a large radius and be offset from the trap center. This was corrected by applying a rotating wall drive after loading in order to center and compress the plasma to high densities. Cut-trappng is also sensitive to the initial beam energy, electrode potential, and ramping rate since these can change the radial offset of the beam as it is cut. Due to small drifts in the filament emission over the course of a day from heating, this can present problems in loading stability when the experiment is in heavy use. This trapping technique is often useful for loading a reservoir of electrons in one end of the trap that can be used to supply experiments requiring a large number of small pulses of particles in quick succession.

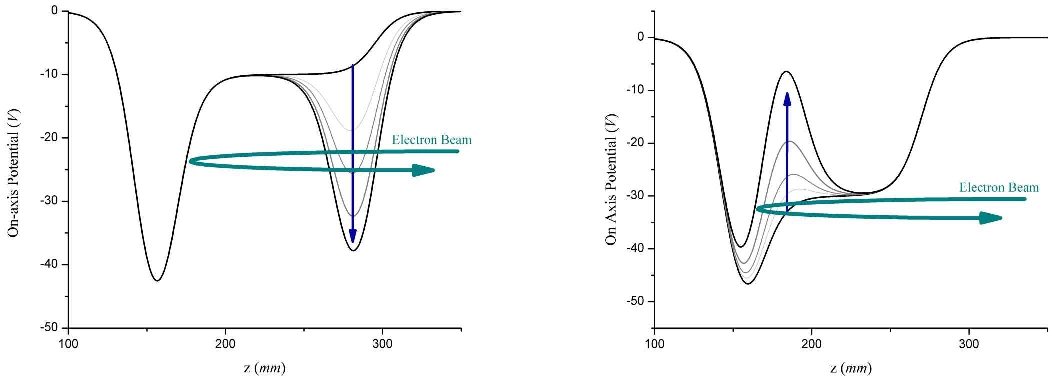

Figure 3.6: A comparison of common loading schemes. Cut-trapping (*left*) raises the potential of a single electrode to cut the beam, while pull-trapping (*right*) relies on instabilities driven by collisions to fill the lowered trapping potential. Note that electrons are captured at high electrostatic potential since they are negatively charged.

Pull-trapping is used for greater control over the loaded electron number. The depth to which the potential well is biased correlates with the number of electrons loaded, up to an observed linear density limit, dependent on magnetic field. This has not been well characterized. At T=4.0T, we observe saturation near $15M\mathrm{e}^{-}/cm$. Pull-trapped electrons generally have smaller radius when loaded, and are less sensitive to filament heating. These behaviors have been partially modeled by performing instability analysis on the electron beam.

3.7 Plasma Mode Diagnostic

Plasma oscillation modes, called Trivelpiece-Gould modes, can be detected by driving an RF signal with small frequency distribution on an electrode and recovering the signal from a separate electrode. The specific target mode driven determines the location of the drive and pickup electrodes. Measurement of mode frequency shifts is useful for nondestructive measurement of the temperature of a plasma at high temperatures due to thermal perturbations of the plasma distribution [22, 30] . Signals are generated by an arbitrary waveform generator, a National Instruments PXI-5421, and sent to electrodes through the high-pass signal filter. The pickup electrode signal is filtered with a band-pass and amplified by a SR445A multiple-stage amplifier. The amplified signal is digitized using a National Instruments PXI-5142, and a digital FFT analysis processes the mode response and determines frequency. This can only be done with a large number ($N \sim 10M$) of confined electrons, due to the sensitivity of our electronics.

3.8 Bulge Cavity Module

Recently we replaced one of the electrode modules (E1-E6) with a module that replaces three of the standard electrodes with reduced electrodes that have smaller inner diameter. The radius of the cavity increases and then decreases smoothly, following a parametric curve such that the interior of these electrodes resembles a bulge. The bulged electrode structure was designed and characterized by Nathan Evetts and Walter Hardy from University of British Columbia to isolate specific modes of the cavity from the exterior by designing the ends of the cavity to act as microwave cutoffs for the mode. [29] In this way, the mode is isolated from external radiation at the cyclotron frequency with coupling at a comparable rate to the dissipation expected from a closed OFHC cavity.

The electodes for the bulge cavity are made of OFHC copper. The maximum inner diameter of the bulge is 2.40cm and reduces to 2.00cm at either end to trap resonant radiation in the cavity. The cavity interior was sputtered with a layer of nichrome to reduce the effective Q of the cavity in order to prevent mode saturation and to allow for easier locating of resonant modes. The nichrome, while slightly magnetic, only contributes minimally ($< 1G$) to the magnetic field experienced by particles on axis. This nichrome was measured to reduce

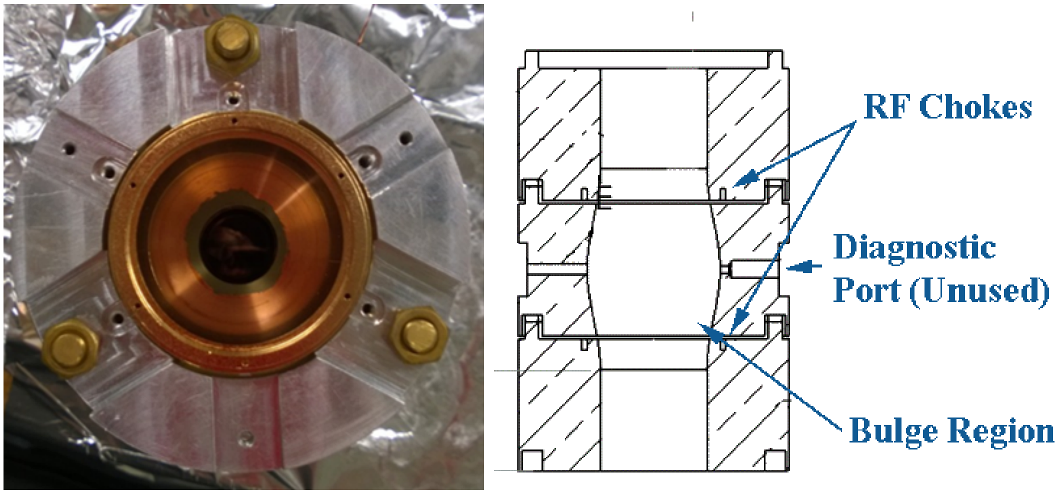

Figure 3.7: The Bulge Cavity. The photograph (*left*) shows the bulge cavity installed in one of the electrode modules in the E2-E4 position. Note that the cavity has a dark coating on the interior, a combination of colloidal graphite and a sputtered layer of nichrome. A cross-section of the bulge electrodes (*right*) shows the shape of the cavity. Note that microwave chokes are included in the electrode design to further reduce leaks into interelectrode gaps. A diagnostic port was used to find mode locations on bench tests, however this port is currently unused when the electrodes are installed.

the Q of the targeted TE_{131} mode at 33.6GHz (cyclotron radiation resonant at 1.2T). The electrodes were painted with a layer of colloidal graphite to prevent oxidation.

The primary advantage of the bulge cavity is that particles can be injected without having to mechanically open an aperture at the ends of the cavity while still maintaining high-Q in the region. We successfully measured enhanced cavity cooling in this region, as described in detail in chapter 5.

3.9 Vacuum Compatibility of 3D-Printed Materials

Additive manufacturing, or 3D printing, of parts has many potential advantages over traditional machining for construction of experimental apparati. [45] Material and machining costs of parts fabricated using 3D-printing methods are generally lower since there is little waste in the process and complicated shapes become much easier to produce. Printing also gives the ability to generate geometries that would have only been previously possible with either welding or an expensive casting process. Since printing is additive, it is possible that there are small voids in the material that would trap gases that would later vent slowly into the vacuum, making the part unsuitable for ultrahigh vacuum environments. [68] It is of particular interest how well these materials perform in a vacuum environment since they can drastically reduce the time and cost to build complicated, specialized geometries, such as resonant electrode strucutres, for use in cold atom traps and plasma devices.

Printed Part Description

In order to test the dimensional tolerances and outgassing properties of printed materials, a CAD design for a modified waveguide was printed by Shapeways in a variety of different materials using printers developed by EOS GmbH. [56] These printers use a technique called selective laser sintering (SLS) to fuse powdered materials into parts. [1] While the waveguides were ordered from a specific printing service, they are thought to be representative of 3D printed materials by examination of material datasheets from similar sintering printer services that use the same methods. The waveguide was modified to include extra exterior tabs to measure dimensional tolerances of the printing process. Printed materials included glass, acrylic, PA12 polyamide, alumide (polyamide/aluminum powder), and sterling silver (92.5% Ag). Although stainless steel was also available, we did not use it in our system since it was found to be a highly-magnetic alloy incompatable with magnetic confinement experiments of interest to us. It is important to note that sterling silver printing is a cast part where the mold has been 3D printed, so it is not expected to have trapped gases that the other materials may have.

Anomalies in the printed parts were noted for these waveguides. Glass was found to be unsuitable for fine detail, as it warped significantly such that surfaces designed to be flat became noticeably concave ($>$ 0.5mm deflection), even with sufficient support during printing. Common failure modes in others materials included minor distortions in thickness or breaks, especially in a thin tab (0.65mm) designed to test fabrication of small features. At the present, fractures and poor resolution in thin features is a known issue with printing fine-detailed objects fabricated by a laser sintering process. [70] The thin acrylic tab broke off at the base during shipping and the silver tab, while solidly attached, had a small fracture running through the material. The adjacent, thicker tab (1.29mm) did not have these defects in either the silver or acrylic. The printed silver and acrylic were found to have excellent machinability, so some small features may still be possible by traditional machining methods after printing an oversized piece.

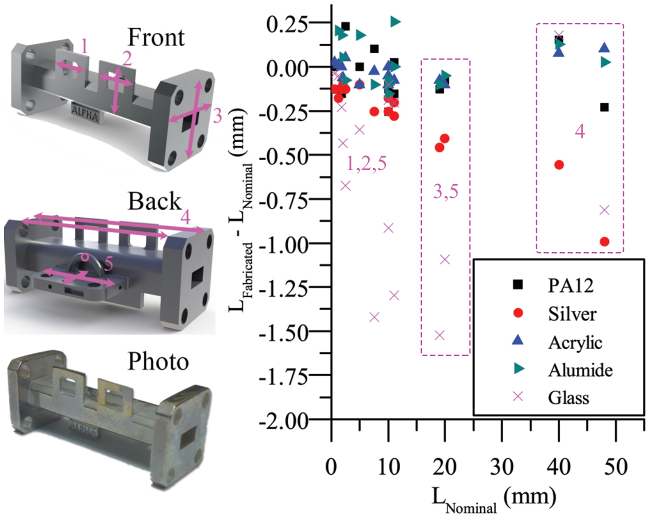

Figure 3.8: (Color online) CAD renditions (*top left*) of a modified waveguide used as an sample 3D printed part compared a photograph (*bottom left*) of the actual waveguide printed in sterling silver. The lengths of particular features of this waveguide, highlighted and numbered in the CAD renders, are compared to printed versions of waveguide in different materials; the difference of the measured length of each waveguide to the nominal length in the CAD submission is shown for these features in the graph. (*right*) The numbers on the graph refer to the numberic labeling of features on the CAD drawings. The waveguide has dimensions 48mm × 20mm × 19mm. Measurements were made to 0.01mm accuracy and precision.

.

The accuracy and precision of printed part dimensions was measured by comparing the lengths of features on the waveguide to the nominal specifications in the CAD model. The difference between the nominal and measured lengths are compared in Fig. 3.8. Note that the silver part was found to be scaled down by $\sim 1.6\%$ relative to the CAD model; this was confirmed by the printing service to be a miscalibration of the scaling in the printer. In order to compensate for this, we measured accuracy as the variance from the residual sum of squares assuming a linear offset. The accuracy was found to be $\sigma_{\mathrm{Ag}} = 0.072$mm, $\sigma_{\mathrm{Acrylic}} = 0.062$mm, $\sigma_{\mathrm{Glass}} = 0.557$mm, $\sigma_{\mathrm{Alumide}} = 0.175$mm, and $\sigma_{\mathrm{PA12}} = 0.138$mm for silver, acrylic, alumide, glass and polyamide respectively.

Vacuum Properties

Before measuring the outgassing behavior of the materials, the waveguides were chemically cleaned and baked in vacuum to remove any oils or dust. Using CERN cleaning guidelines,[74] adapted as needed to suit the variety of materials, the following general procedure was used

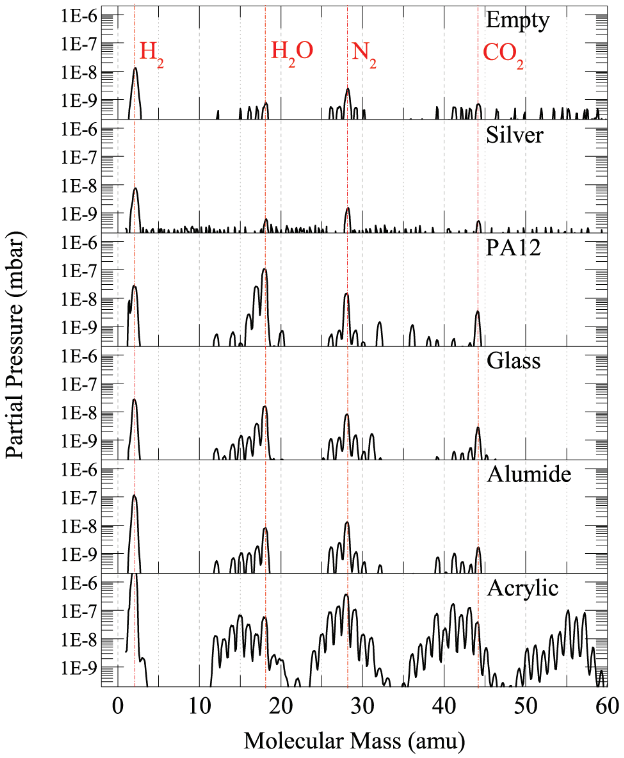

Figure 3.9: Residual gas analysis of materials in a vacuum system 24 hours after cleaning and bakeout processes. The top curve is the residual gas of an empty chamber.

to clean parts:

1. Ultrasonically clean part in deionized water with mild detergent
2. Rinse with deionized water
3. Degrease using acetone if material is acetone resistant
4. Ultrasonically clean with ethanol heated at 40C to dissolve excess organics
5. Evaporate excess ethanol by spraying with dry nitrogen
6. Insert into vacuum chamber and pump down to 10^{-6} mbar or better pressure
7. Bake chamber at 24 hours at minimum of either 120°C or maximum recommended temperature of the material. Ramp temperatures up and down at a maximum of 5C/hr.

The baking and residual gas analysis was performed in the same vacuum chamber. The 25L, room-temperature vacuum chamber was brought to ultrahigh vacuum by a turbopump backed by a dry rotary roughing pump and maintained using an 150L/s ion pump. The empty chamber was able to be pumped to an ultimate pressure of $2.0 \cdot 10^{-9}$ mbar. With the gas analyzer filament on, the empty chamber pressure rose to $1.2 \cdot 10^{-8}$ mbar, where nearly 90% of the total pressure is due to molecular hydrogen. This is a typical behavior found in hot-filament vacuum gauges such as the gas analyzer due to adsorption processes. [63]

The residual gas analysis was performed using a SRS RGA100 mass spectrometer 24 hours after the bakeout was completed. The spectrometer filament was placed out of line of sight of the test piece to avoid excess heating; results are shown in Fig. 3.9. The silver piece had outgassing rates below $1 \times 10^{-10}\mathrm{mbar\,L/cm^2s}$, the detection limit of our analyzer. The polyamide and alumide had outgassing rates of $\sim 3 \times 10^{-8} - 4 \times 10^{-7}\mathrm{mbar\,L/cm^2s}$ following baking, comparable to teflon and viton materials.[59] The residual gases present were atmospheric, suggesting that air was trapped in the material. Alumide, although part polyamide, appears to have adsorpted less water from the cleaning process. To avoid sublimation of polyamide material itself, the polyamide based materials must be baked at a low temperature (65°C). When attempts were made to bake at 100°C, the vacuum became very poor ($\sim 10^{-6}$mbar) and a residue was found on the vacuum chamber walls near the piece. Glass had outgassing performance comparable with the polyamide materials, but could be baked at higher temperatures.

Acrylic was not able to be pumped to ultrahigh vacuum pressure levels. The mass spectrum for acrylic appears to have a hydrocarbon chain contamination, shown as the 13amu repeating feature in the mass spectrum, leading to the conclusion the acrylic material was sublimating into vacuum, even at low (55°C) baking temperatures.

Of the tested materials, only sterling silver was found to be accurately printed and UHV-compatible; polyamide-based materials could be used sparingly in vacuum similar to teflon and viton. Glass and acrylic are not recommended since glass tended to deform during fabrication, and acrylic had very poor bakeout performance.

Chapter 4

Plasma Imaging and Temperature Diagnostics

In this chapter, we will discuss various diagnostics that are used to understand the behavior of plasmas in our system. While the basic idea behind these techniques has existed for nearly 35 years [61], we introduce refinements to the diagnostics that improve the measurements of the radial profile and temperatures in the plasma, allowing for better modeling of these systems.

While working with the ALPHA collaboration, I developed the imaging system used for analysizing radial profiles of confined non-neutral plasmas. This has proven to be an invaluable tool in understanding the dynamics of particles confined in the system in order to optimize confined positron-antiproton behavior for $\bar{H}$-synthesis. The equipment and calibration used in this imaging system at ALPHA is described in section 4.1. This information has appeared in a previously published article [5]. In section 4.2, this technique has been extended to use the microchannel plate as ultralow noise (sub-10 electron resolution), high speed-charge amplifier by collecting the light generated by the phosphor screen.

In the final section, we discuss the development of analytical techniques to quickly measure the relevant plasma parameters from acquired data.

4.1 Antiproton, Positron, and Electron Imaging with a Microchannel Plate/Phosphor Detector

Microchannel plate (MCP)/phosphor screen based diagnostics have proved invaluable in studying the evolution of lepton plasmas in Penning-Malmberg traps [24, 16, 61] . The MCP is used as an imaging device by accelerating electrons into a phosphor screen. It can also be used as a low-background particle detector by measuring current drawn by the MCP during measurements. These diagnostics provide a radial profile of the trapped particles that enables one to infer information about the plasma.

Recently, cold-antiproton ($\bar{\mathrm{p}}$) experiments at CERN have extended the use of this diagnostic to antiprotons [3, 4, 2, 11, 39]. In this paper, the ALPHA collaboration reports on the relative and absolute sensitivity of the MCP to leptons and $\bar{\mathrm{p}}$'s and shows how the diagnostic can be used to find the line-integrated radial density profiles of the particles in our Penning-Malmberg trap. The goal of the ALPHA collaboration is to synthesize, trap, and study antihydrogen. Knowledge of these radial profiles is invaluable in the optimization of this process.

The implementation of this diagnostic in our experiment is complicated by several unusual factors. Space and thermal isolation requirements force us to place the MCP in the fringe field of our solenoid. As a result, the path the particles take while being extracted from the trap to the MCP is sensitive to the details of magnetic fringe fields as well as the energy and mass of the particles. Additionally, $\bar{\mathrm{p}}$'s annihilate when striking the MCP; products from these annihilation events can cause additional emission of electrons from the MCP. Thus, the response of the MCP to $\bar{\mathrm{p}}$'s is greater than one would predict from protons of equivalent energy [40]. This enhanced response has not previously been well characterized.

Plasma Extraction Procedure

In the ALPHA apparatus, non-neutral plasmas are confined in a Penning-Malmberg trap [11]. The traps employ a large superconducting solenoid to generate a 1 T axial magnetic field homogeneous over 80 cm to one part in 10^3 in the trapping region. This magnetic field confines the particles radially. A series of annular electrodes are used to create axial electrostatic wells for axial confinement. Two pairs of correction coils can be used to adjust the tilt of the magnetic field over 60 cm in the trapping region. Neutral (antihydrogen) atom confinement is achieved by adding an Ioffe-type octupole plus mirror fields. These fields create a magnetic minimum in which antihydrogen atoms can in principle be trapped. However, for the majority of this paper, particle imaging is performed without inclusion of the transverse neutral-trapping magnetic fields to simplify the analysis of data.

An upstream injection line at CERN's Antiproton Decelerator facility provides antiprotons on average every ~ 100 s, some of which are degraded to ≤ 5 keV and captured [8]. Electron and positron sources are both located downstream from the trap. Once injected, the clouds of charges are manipulated into a desired location, density, and temperature through

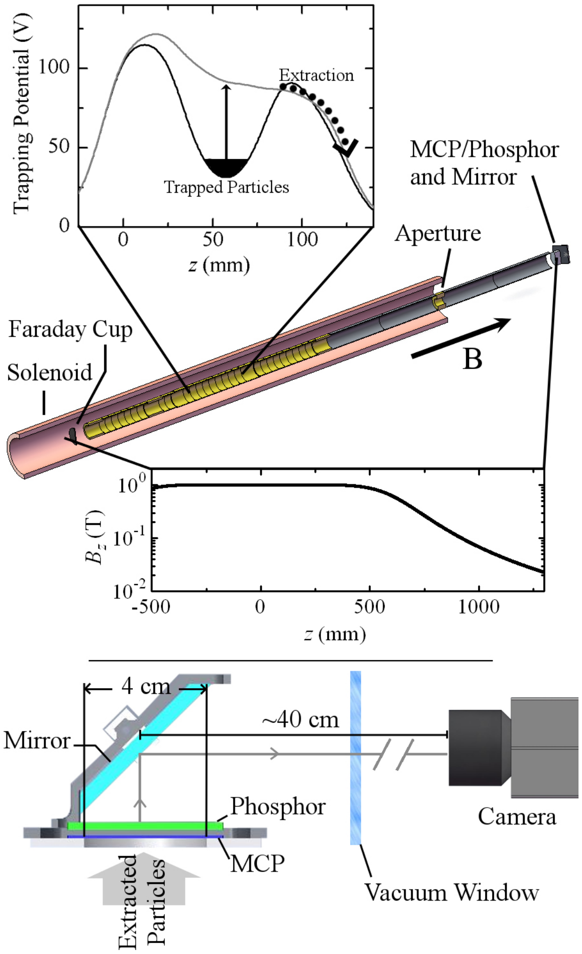

Figure 4.1: (Color online) Cold plasma trap (top) and MCP imaging system (bottom) of the ALPHA experiment. Particles are extracted from the trap by slowly (over milliseconds) raising the potential under the trapped particles, allowing them to escape over the lower barrier of the well. Once over the barrier, the particles are ejected with an effective kinetic energy of 100 eV along the magnetic field. Particles that impact the MCP are amplified and imaged as described in the text.

changes in electrode potentials, application of additional magnetic fields, and passive radiative cooling to the 7K background temperature of the trapping environment.

To measure the plasma properties, the electrode potentials are manipulated so that the particles escape from the trap towards the MCP, which lies 1.3 m downstream from the trapping region, in the fringe region of the magnetic field ($\sim$ 240 G, See Fig. 4.1). Typically, particles are extracted from the trapping region with 100 ± 1 eV of energy. The plasma is highly magnetized during extraction, in the sense that particles follow magnetic field lines closely as they are constrained transversely by cyclotron motion. The magnetic field lines guide the extracted particles down the extraction column onto the MCP. The leptons are effectively bound to the field lines along their entire extraction trajectory; antiprotons deviate during the last few centimeters of their trajectory. The electrodes and aperture along the extraction column can collimate the outer edge of the particle cloud as it travels to the MCP, limiting the transverse size of the trapped particles we can image.

We image using an 4.0 cm diameter MCP and phosphor screen assembly purchased from El-Mul Technologies. The assembly is controlled by three voltages, applied to the front and back of the MCP and to the phosphor, that can be adjusted to suit the particle species and line-density. The front voltage accelerates the incoming particles over the last few centimeters of their trajectories to a desired impact energy; this is usually set to give the particles a maximum impact energy of 200 eV. The MCP's back plate voltage relative to the front controls the gain of the MCP and is chosen to avoid saturation. The front-to-back voltage is varied from 900V for low numbers of trapped particles ($N < 10^5$ leptons or 10^3 $\bar{\text{p}}$), down to 400 V for large numbers ($N > 10^8$ leptons or 10^5 $\bar{\text{p}}$). Higher gains (greater front-to-back voltages) saturate the MCP for large numbers of particles. We use a 120 ns response phosphor (P47) placed at 3.0 kV relative to the back of the MCP to convert the shower of electrons from the MCP to $\sim$ 400nm photons with an amplification factor α of 24 ± 3 photons/e$^-$ [65].

Images on the phosphor screen are captured on a CCD camera placed outside the vacuum chamber. The camera shutter is set to open over the entire extraction cycle. The CCD camera (PCO Sensicam QE) captures a 688×520 image from the phosphor screen with quantum efficiency $\eta_{qe} = 40\%$ and signal readout resolution of ≈ 4.1 electrons (10.3 photons)/pixel on the CCD chip [66]. The area imaged by each pixel (6200 μm^2) is square and contains roughly 30 MCP channels. The cross section of photons that are measured on the CCD have an effective solid angle $\Omega_{cam} = 2\pi\left(1 - \sqrt{1 - 1/4N_f^2}\right)$, where N_f is the f-number of the lens used with the camera. Putting this information together, the number of electrons stored on the CCD scales with the number charges emitted from the MCP by a factor $\eta_{qe}\alpha\Omega_{cam}/(4\pi)$. The ratio of electrons ejected from the back plate of the MCP to the number of incoming particles is referred to as the MCP's gain.

The large number MCP response to each species is calibrated by comparing the extractions of particles to the MCP to extractions to a Faraday cup held at 1 T, 40cm upstream from the trap region. Since both measurements are destructive, they must be performed on successive injections of particles. For leptons, we find the results to be very repeatable,

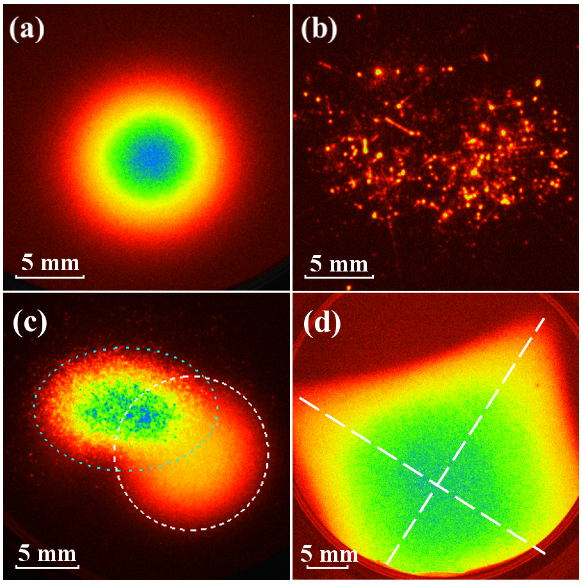

Figure 4.2: (Color online) In (a), we show a typical profile of a lepton plasma; in this case, positrons. The high-gain, sparse p̄ image in (b) shows the tracks from annihilation products of the antiprotons. During a mixing operation (c), overlapping e^- (white dash) and p̄ (cyan dots) are extracted simultaneously to demonstrate differences in the transverse mapping of species. Note that p̄'s make defined speckled patterns while the electrons image to a smoother distribution due to the number of particles imaged ($\sim 10^6$ e^- and $\sim 10^4$ p̄). Perturbing the extraction with transverse trapping fields (octupole) produce images with azimuthally dependent deformation as shown in (d); axes of deformation are shown as white, dashed curves. Color intensity (red to blue) scales to the peak intensity of each image.

having reliable counts of particles with $\leq 5\%$ injection variance during steady operation. The number of leptons is found by measuring the total accumulated charge on the Faraday cup, with a background noise level of 10^5 charges. However, this technique does not work for p̄'s since there are significantly fewer of them, and the resulting signal is below the noise level of our electronics. Additionally, even if noise level was improved, the accumulated charge would not directly indicate the p̄ number since decay products from nuclear-p̄ annihilations may carry away charge. Instead, the Faraday cup is utilized as a beam stop, and p̄ numbers are found by detection of charged particles from annihilations on the Faraday cup by nearby scintillator/photomultiplier pads. The efficiency for p̄ annihilation detection by the scintillator/PMT system is estimated by Monte Carlo simulations to be $25 \pm 10\%$. The accuracy is in part limited by the knowledge of the branching ratios of annihilation reactions. Since this is an unknown of the overall scaling factor, and is not apparent in measurements, we have chosen to omit this uncertainty in figures in this paper with the understanding that it is always present for absolute p̄ numbers.

MCP Calibration

Microchannel plates consist of a dense array of amplifying channels. Particles that hit the front of the MCP may release electrons into a channel [78]. The electron is accelerated along the channel, and may initiate a cascade within the channel. For a small number of particles, the MCP gain may be as high as $3 \cdot 10^4$ (for leptons); however, if a large number of particles is extracted, we find that the gain is more limited. This happens because the rate at which charge is expelled from each channel during measurement is much greater than the current from the circuit's RC-recovery, effectively depleting the channel [36]. We measured the stored charge limit to be $\sim 2 \cdot 10^4$ electrons on average per MCP channel.

The impact of one low energy electron or positron initiates approximately one cascade. An antiproton, however, annihilates with the MCP material. The high energy secondary particles that result from the annihilation can excite additional cascades, enhancing the MCP gain. Tracks from secondary particles are often visible in images taken with our MCP, as shown in Fig. 4.2b. Thus, the response of the MCP to individual $\bar{\text{p}}$'s varies. Using images similar to Fig. 4.2b, with low numbers of extracted particles, we compare the distribution of the spot intensities on the phosphor screen from both electrons and antiprotons in Fig. 4.3. When necessary, we take care to aggregate the signal from a $\bar{\text{p}}$ spot and its track. We find that the response per $\bar{\text{p}}$ event has a much wider distribution than for the electrons. Despite the wide distribution in intensities of an individual event, the data shown in Fig. 4.4 demonstrate that, experimentally, the MCP response to a cloud of $\bar{\text{p}}$'s is linear over a wide and useful regime. Profiles for a small number of events can still be generated by point-finding routines on the image. The measurements in Fig. 4.3 and Fig. 4.4 were taken at

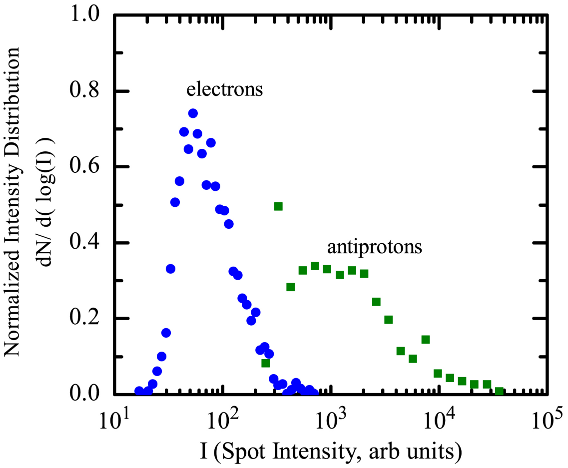

Figure 4.3: Normalized ($\lim_{I\to\infty} N(\log I) = 1$) electron and antiproton spot intensity distributions. For both species, the MCP front-to-back voltage was 900 V; the impact energy was 200 eV. These parameters maximize the gain.

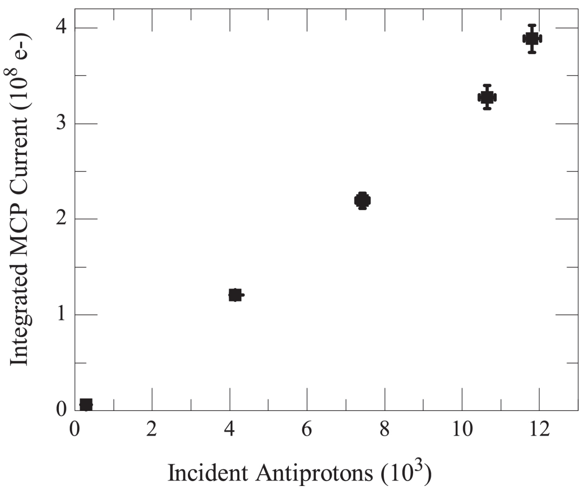

Figure 4.4: Response of the MCP as a function of the number of $\bar{p}$. Same biasing parameters as in Fig. 4.3.

the maximum MCP gain settings to demonstrate that the detector does not saturate for the number of $\bar{p}$'s measured.

Figure 4.5a compares the MCP response to $\bar{p}$ and leptons as a function of front-to-back bias. The data were obtained by extracting the particles from the trapping region with a uniform energy of 100 eV and then varying the impact energy by changing the bias on the front plate of the MCP. This procedure assures that extraction energy and trajectories are independent of the bias as the potentials are largely identical over all but the last few centimeters of the particle paths. Since we assume that branching ratios of nuclear-$\bar{p}$ annihilation do not change significantly for low impact energies, the supposition that the response is generated from $\bar{p}$ annihilation products of $\bar{p}$ implies that the effective gain should be largely independent of $\bar{p}$ impact energy. However, the method of changing the bias of the front plate of the MCP to adjust impact energy has an additional effect on the gain. For $\bar{p}$ impact energies of less than 100 eV, the absolute bias on the MCP front plate is negative; this can reduce the measured gain since electrons ejected off the front plate are pushed out to the grounded walls of the vacuum chamber instead of being pulled back onto the MCP. We are unable to disentangle this effect from the response of the detector for low energy $\bar{p}$ impacts. This effect manifests itself for leptons as well; the kink near 100 eV in the e^+ response occurs because the front bias is repulsive to secondaries for impact energies of greater than 100 eV (since the e^+ charge is opposite of the $\bar{p}$ and e^-).

The gain for all three species of particles increases near-exponentially with the front-to-back bias as shown in Fig. 4.5b. This result indicates that the underlying amplification mechanism of the MCP remains intact, despite a two order-of-magnitude difference in the gain response. We do not expect the 240 G magnetic field on the MCP to greatly affect the gain from a zero field setting since the length scale of electron cyclotron motion in the channel is much larger than the channel size on the MCP. However, this might no longer be the case if the MCP were placed in fields on the order of 1 T.

Radial Profile

The mapping between the observed radial profile and the actual plasma can be quickly constructed under the assumption that the particles are strongly magnetized, meaning the distance traveled during a cyclotron period satisfies $v_{\parallel}/\Omega_c \ll |(\partial\mathbf{B}/\partial z)/B|^{-1}$, where $v_{\parallel}$ is the transverse velocity and Ω_c is the cyclotron frequency. When this assumption is met, charged particles closely follow field lines onto the MCP, leading to a radial expansion of $\sqrt{B_{\text{trap}}/B_{\text{MCP}}}$ about the axis of the solenoid. Simulations using a fourth-order Runge-Kutta trajectory solver find that magnetic-guiding overestimates the expansion by 2% for antiprotons; electrons remain strongly bound to field lines and the expansion is accurately predicted by the above estimate.

Even strongly magnetized particles will undergo $\mathbf{E} \times \mathbf{B}$ and magnetic curvature drifts. In our system, drift corrections are on the order of $\sim$ 100 mrad about the magnetic trap axis during the extraction process from the trapping region to the MCP. Since electrons and positrons are ejected from the trap with much higher velocities, and in much greater densities than the antiprotons, the drifts induce species-dependent rotations of the MCP image from the actual trapped particle distribution. These differences would not be noticeable for radially symmetric plasmas since the drifts would induce azimuthal motion; however, misalignments between the magnetic field lines and the electrode axis can drive these rotations about an “off-center” axis. We observe offsets, shown in Fig. 4.2c, between $\bar{\text{p}}$ and lepton images, that we attribute to this effect.

To simplify our interpretation of images, we normally extract particles with the transverse neutral trapping fields turned off. However, when particles are ejected in the presence of such transverse multipole fields, the magnetic field lines, and therefore the trajectories become more complex. A distorted image (Fig. 4.2d) generated by the inclusion of magnetic fields for neutral particle transverse-confinement is observed with octupole-symmetry as expected. Knowing the applied multipole moments, the radial profile can, in principle, be reconstructed from such images by applying an appropriate mapping of the field lines back into the trapping region.

Conclusion

We have developed an MCP/phosphor screen system to measure the radial distribution of low energy electrons, positrons, and antiprotons extracted from a Penning trap. We have calibrated the response of the MCP to all three species and found that the gain for antiprotons is significantly higher than the gain for leptons. We posit that this behavior is due to additional MCP channels being triggered by nuclear-$\bar{\text{p}}$ annihilation products.

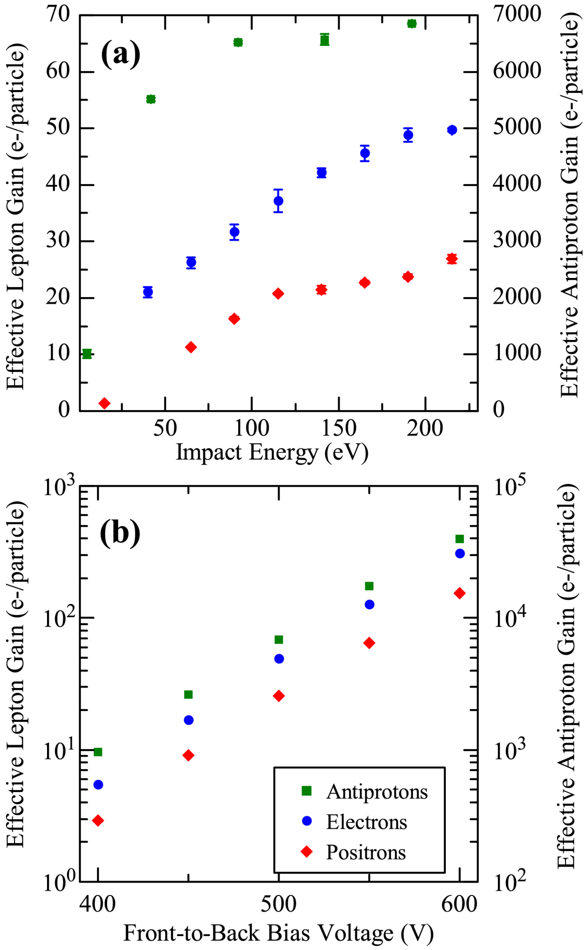

Figure 4.5: (Color online) Effective gain of the MCP for different species of particles while varying the voltages on the front and back plates. Particles are extracted from the trap at $\sim$ 100 eV and accelerated by the front plate voltage. In (a), the front-to-back voltage bias was kept constant at 500 V, while impact energy is varied; in (b), the front-to-back voltage bias is varied while the impact energy is held at 200 eV. The uncertainties in the measurements in (b) are $< 2\%$.

4.2 Photocell Detection for Time-of-Arrival Analysis

Traditionally in non-neutral plasma experiments, destructive diagnostics are performed on a plasma by extracting it onto a charge collector. The time at which the charges begin to arrive on the detector gives information about the distrubution of the trapped charges. Often this charge collector takes the form of a microchannel plate (MCP)/phosophor assembly, as discussed in the previous section, since the assembly amplifies charge through an avalanche process [78], which allows for imaging of the plasma distribution by accelerating amplified charges onto a phosphor screen. The avalanche process has a response time of $\sim$ 40ns, and so the phosphor plate itself can be used as a charge collector by reading voltages across a capacitor connected between the plate and the ground.

This method of charge collection has the advantage of being quite robust for larger amounts of charge in a laboratory setting, and requiring relatively few components. There are however disadvantages to this measurement that can reduce the effectiveness. Since the phosphor screen must be biased at a voltage higher than the voltage applied to the back of the microchannel plate, typically $\geq$ 1.2kV, the capacitor is not able to be read directly from the plate, but rather through a 1kHz high-pass filter to isolate the high voltage. This has the consequence that the ripple noise associated with high-voltage power supplies is passed to our digitizer as well, creating a high noise baseline in our system, even with 1Hz pi-filters installed between the power supply and the detector. In addition, high-voltage capacitors needed for this job are expensive and often do not perform to the specified voltage without risk of discharges. These discharges can mask the actual plasma signal and, at worst, damage the preamplifiers used by the digitizer to record the signal, even with diode protection installed. This method also relies on a high-quality ground for low background noise, which is difficult to achieve in our experiment.

In order to avoid these difficulties, we have developed a photocell diagnostic that converts excess light generated by the phosphor screen, that is not used by the camera in the imaging system, to measure the charge deposited as a function of time. This technique allows for a higher singal-to-noise ratio and therefore better resolution ($\leq$ 10 electrons) on the accumulated charge since the phosphor now acts as an additional amplification stage and the detector is now floating from the noisy ground of the device. Here, we describe the construction and layout for using a photodiode in this manner, and compare it to the charge collector method.

Theory of Operation

Electrons that impact the microchannel plate and enter one of the channels are amplified by an avalanche process. This process is tunable based on voltage applied across the plate, however in typical settings used, this generates 10^4 electrons at a efficency of $\eta_{\mathrm{MCP}} = 75\%$, corresponding to the cross-sectional area of the channels. Once the electrons are generated,

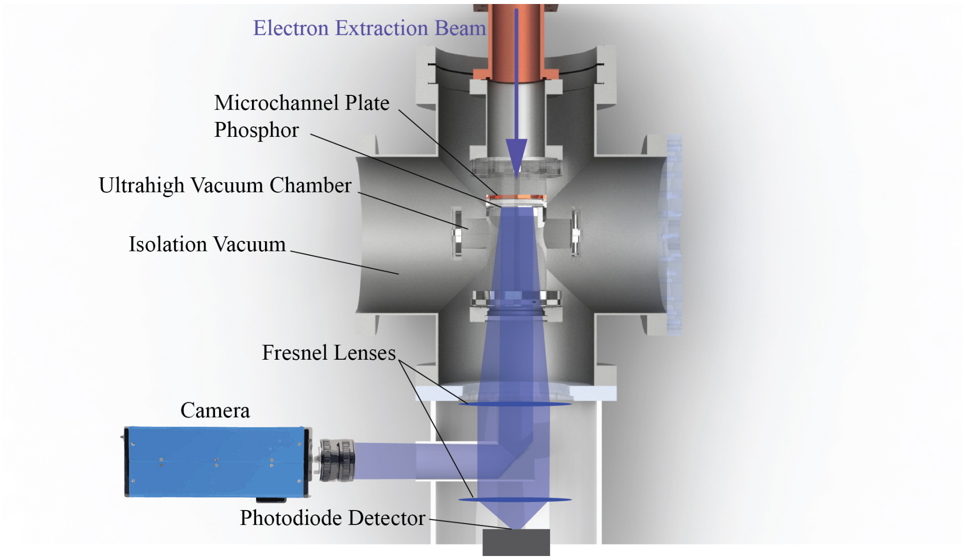

Figure 4.6: The layout of the photodiode detector scheme. Electrons impact the MCP and the signal is converted to photons by the phosphor screen. This assembly is in an ultrahigh vacuum chamber, which itself is placed in a high vacuum for isolation purposes. The light must travel through two vacuum windows over a distance of 10" to reach our external optics. Part of the light passes through to a mirror, which redirects it to a camera. The remaining light is refocused onto a photodiode assembly using a pair of Fresnel lenses.

they are accelerated with $\Delta V \geq 3750V$ onto a (P47) phosphor plate. This phosphor has a particularly fast response time (49ns), and will emit 30-200 400nm photons per incident electron, tunable by the accelerating voltage applied to the plate. The short response time makes the signal generated by the light appropriate for time-of-arrival measurements in our plasma diagnostics. The phosphor is backed by a fiberoptic material the passes the light back toward a vacuum window in our apparatus. In normal operation, this gives an effective gain of $\sim 5 \cdot 10^5$ photons per electron incident at the front of the plate.

The emitted light passes through two vacuum windows onto an optics platform. Here the light is redirected, using a pair of Fresnel lenses, onto a photodiode detector. Fresnel lenses are used since they are signifcantly cheaper than using a large standard glass lens and use less space on the optics table. A portion of the light from the window ($\sim$ 10%) is reflected onto a fast-shutter camera, through an aperature cut into the Fresnel plate so that the light can pass through to the camera undistorted for imaging. The remaining light (70%) passes around the mirror and mirror mount and is refocused by a second Fresnel lens onto a Thorlabs FDS100 photodiode sensor. The photodiode sensor converts the light to an electron-hole pair with quantum efficiency $\eta_{\text{PD}} = 31\%$. While reflections on the vacuum walls provide more light to the sensor and therefore a higher effective solid angle, we conservatively estimate the solid angle of the first fresnel lens using light directly coming from the phosphor screen as $\Omega/4\pi \approx .05$. In this case, the photodiode acts a 0.6-gain charge amplifier with respect to charge arriving at the plate using standard voltage acceleration for our device.

While a lower-than-unity gain may seem disadventageous at first, the noise can be made significantly lower on the photodiode circuit since it is not connected to the chassis of the experiment. In addition, the capacitance assocated with charge collected is signficantly lower (50pF at 9V reverse bias) with the photodiode than the capactiance required from the coaxial cabling for the in-vacuum high voltage lines (1.3nF), resulting in a higher voltage-per-charge readout.

Transimpedance Amplifier

It is necessary for the photodiode to have an amplifier attached that is capable of 100ns response times in order to measure temperatures at the 10K level in our system. The challenge was in finding an amplification solution that provided high bandwidth, low bias current, and high slew rates, and could be operated for days with standard batteries. The problem with many amplifiers that operate in this frequency regime is that they are only stable over relatively short bands of response; many of our initial attempts to solve this problem involved the RF amplifier either being perturbed easily into unstable behavior or the circuit oscillating at large amplitude near poles at $f \sim 10$MHz. We have developed a solution that solves these problems and allows for a 50-gain preamplification stage on our photodiode signal.

The solution is in a combination of our choice of operational amplifier and using a small-signal, high-speed transistor to supply the necessary current to the operational amplifier from the photodiode signal, as shown in Fig. 4.7. The Intersil EL2125 was found to fit the requirement of stability over a wide range of frequencies (1kHz-10MHz), while maintaining a very low noise level. In addition, it had the benefit of a large range for input bias voltage and supply, which is helpful when designing a photodiode circuit that needs to be reversed biased for better capacitive behavior. The only problem with this chip was the relatively large input bias current offset, meaning that charge accumulated by the photodiode would quickly be drained by the amplifier. In order to remove this drain, a 2N3823 is used to manage the current load, so that the accumulated charge remains on the diode and regulates the voltage on the transistor. The circuit has a fast recovery time of 50μs from charge drained through the 1MΩ resistor, but this is enough to time to record the relevant information about the tail of the distribution for plasmas with $T < 1$eV without problems resolving the signal due to background noise.

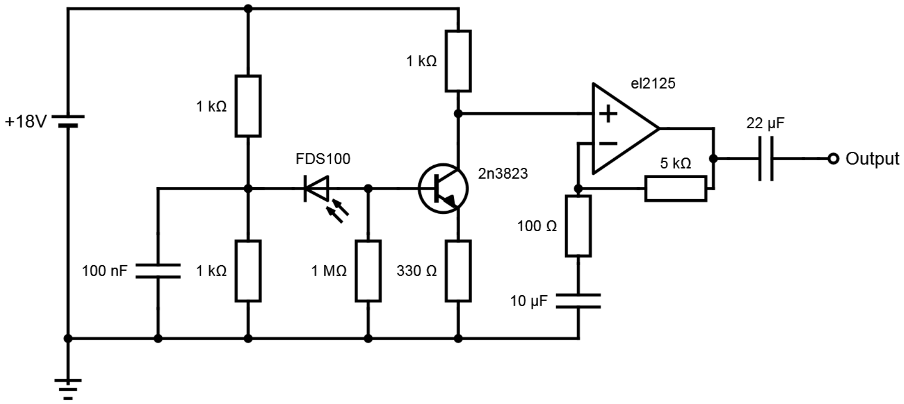

Figure 4.7: Transimpedance amplifier circuit diagram.

Results and Comparison

A typical amplified photodiode response to a plasma extraction is shown in Fig. 4.8 and compared to the response of the pickup on the high-voltage bias cable. Here, the signal is taken directly from the photodiode amplifier, while the high voltage pickup passes through a Stanford Research Systems SR560 voltage preamplifier with a gain of 100. The response axes for each detector have been rescaled so that the curves are drawn at the same height.

The first noticable feature is the 50kHz ripple on the high voltage line creates a signal-to-noise ratio roughly 10 times higher than the photodiode. The ripple cannot be simply subtracted away since it's unclear if the ripple waveform maintains the same shape as the pickup is biased. The ripple also interferes with the temperature measurement since the phase of the ripple will influence cold temperature measurements which rely on the first thousand electrons to establish a temperature. If the voltage is converted into impacting charges on the detector, the RMS noise of the photodetector corresponds ~ 7.3 electrons incident on the microchannel plate, with the correction for η_{MCP} included.

The photodiode response begins to deviate from the high voltage curve near 2V before it reaches an amplifier saturation limit at 4.3V. The deviation is caused by a combination

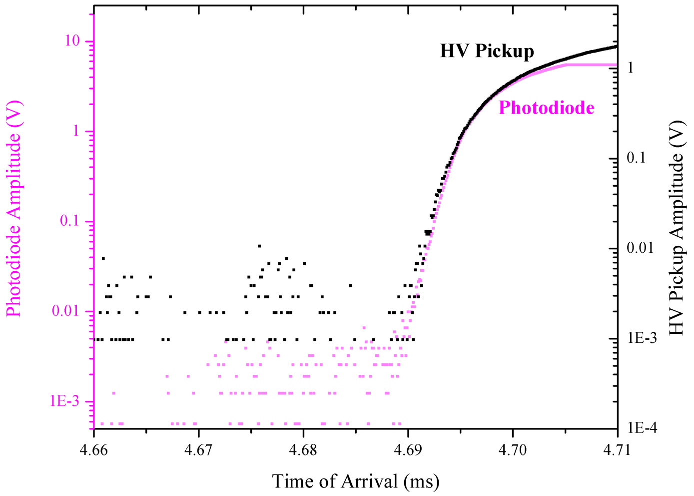

Figure 4.8: The response of the photodiode to a slow plasma-extraction pulse is compared the simultaneous response from pickup on the high-voltage biasing lines. Note that the signal-to-noise ratio of the signal is improved for the photodiode despite a lower saturation threshold. This data was taken with a typical MCP Front/MCP Back/Phosphor bias of 100V/1200V/5000V.

of the faster RC-recovery time and the non-linear correction to the charge extraction of the plasma. As more charge is extracted, the reducing self-fields of the plasma reduce the effective deconfinement rate of particles leaving the well [15] . This reduced rate, convolved with a fast response time of the detector, causes a slower voltage ramp from the amplifier. Fortunately, this this does not distrupt the temperature-measurement diagnostic since the diagnostic only uses the first two decades of signal above the noise floor.

The signal-to-noise ratio has potential to improve beyond the standard settings used in Fig. 4.8 by raising the voltage applied to the phosphor screen and therefore the gain of the photodiode stage. Unfortunately, this is not possible to do safely on our device with the current high voltage feedthroughs. In addition, optics can be inserted into the vacuum system, closer to the phosphor plate to increase the solid angle of light capture. These two enhancements would reduce the noise floor to the single-incident electron level.

Acknowledgements

A guide to high-speed amplifier techniques written by Jim Williams [77], has proven invaluable in diagnosing and inspring a solution to the transimpedance amplifier problem. Eric

Hunter and Nicole Lewis played a significant role by debugging the transimpedance amplifier and optimizing the response behavior.

4.3 Fast Plasma Diagnostic Analysis

A large amount of data is typically collected in each plasma extraction, including a trace of the time-of-arrival of charge and an image of the extracted plasma projected onto the microchannel plate. In order to inform us of interesting experimental parameters while running the experiment, it is often necessary to have real-time feedback on the previous experimental cycle. In order to do this, the experiment uses a suite of curve fitting routines developed to measure the temperature and interesting radial profile parameters of the plasma. Often these curves or images can contain $\mathcal{O}(10^6)$ datapoints, requiring a significant amount of computer processing time to fit the curve to a non-linear model. The nonlinearity makes it difficult to quantify the uncertainty in individual parameters once the curve is fit. In this section, we discuss a series of fast plasma diagnostic analysis routines developed to improve accuracy and reduce computation time for this information.

Temperature Fitting Routine

The temperature of the electron plasma is measured by extracting electrons onto a microchannel plate detector as discussed in the previous sections. The time-of-arrival of particles is measured as an integrated charge collection signal. Since the electrons are Debye shielded within the plasma, they are expected to have a Maxwellian velocity distribution in the axial direction,

$$f(v_z) = n_0 \frac{2m_e}{\pi k_B T} \exp\left(-\frac{m_e v_z^2}{2k_B T}\right). \tag{4.1}$$

As the voltage applied to the confining electrode, $\Phi(t)$, is monotonically raised to the base of the well, Φ_b, electrons with the highest energy in the distribution will begin to escape. The particles are then accelerated down an electrostatic potential to the detector such that they arrive within 100ns, comparable to the response speed of the detector. The integrated charge extracted to the detector should have the form,

$$N(t) = \sigma \int_{\Phi_b - \alpha\Phi(t)}^{\infty} \sqrt{\frac{e}{2m\phi}} f\left(\sqrt{\frac{2e\phi}{m}}\right) d\phi, \tag{4.2}$$

where α is a geometrical correction of the confinement well depth based on the electrode geometry used and σ is the area over which the plasma is extracted. In our system, for most plasma geometries, $\alpha = 0.67$. Solving this integral yields,

$$N(t) = \sigma n_0 \left(1 - \text{erf}\left(\sqrt{\frac{e(\Phi_b - \alpha\Phi(t))}{k_B T}}\right)\right). \tag{4.3}$$

In the limit of large x, $\text{erf}(x) \to 1 - \frac{e^{-x^2}}{x\sqrt{\pi}}$, so in the tail of the distribution,

$$N(t) \approx \sigma n_0 \frac{k_B T}{\pi e(\Phi_b - \alpha\Phi(t))} \exp\left(-\frac{e(\Phi_b - \alpha\Phi(t))}{k_B T}\right). \tag{4.4}$$

If the electron plasma starts to extract at $t = t_0$, we can set $\Phi_0 = (\Phi_b - \alpha\Phi(t_0))$, and further approximate the above as,

$$N(t) \approx \sigma n_0 \frac{k_B T}{\pi e \Phi_0} \exp\left(-\frac{e(\Phi_b - \alpha\Phi(t))}{k_B T}\right) = C \exp\left(-\frac{e\alpha\Phi(t)}{k_B T}\right). \tag{4.5}$$

The second expression condenses all the constants into a single term C. Therefore, assuming $d\Phi/dt$ is constant over the initial part of the extraction, $N(t)$ can be fit to an exponential function near t_0 and the temperature can be retrieved.

This derivation has ignored the radial profile of the plasma and therefore self-field corrections, which have been studied extensively [17, 10, 15]. Serendipitously, it has also been found that the intial extraction column size, σ, in this configuration is constant with radius $\sim 2\lambda_D$, so we may treat it as a constant for this calculation [73]. Neither of these corrections to the extraction model cause a change in the scaling of $N(t)$ near the extraction time t_0.

The extraction traces are fit to exponential curves $(Ae^{\gamma(t-t_0)} + B)$ using a Levenberg-Marquardt least-squares fitting algorithm [55]. The term t_0 is taken to be a constant as described below. There are, however, practical problems with using only this algorithm to establish a temperature. First, the fitting routine is very sensitive to offsets and noise since a small amount of noise can cause the routine to converge on a poor value t_0 if the initial charge extraction location is "misidentified" by the routine. This can lead to very significant problems when measuring the temperature. Secondly, non-linear corrections to the model described in Eq. 4.5 will force $N(t)$ to appear as if it has a higher temperature when a significant portion of the charge is removed, dependent on the initial charge distribution and temperature. Proper windowing of the data used in the fitting routine is necessary to avoid this non-linear region. It can be frustrating for any experimentalist to measure temperatures since there is generally only a small window of data, above the noise level but below the non-linear region, that can be used to actually retrieve quality temperature information. Finally, since the eigenvectors of the Jacobian used to step the fitting routine have a large aspect ratio in fitting-parameter space and eigenvectors do not generally fall along the fitting parameter bases, the statistical temperature uncertainties are often difficult to characterize.

In order to resolve these problems, an additional layer of statistical analysis has been added to our curve fitting routines. We solve for the statistical uncertainty by subsampling the data. Since data is acquired at 100MHz sampling rate, there is sufficient data to utilize a bootstrapping method on top of the fitting routines. The data is arranged into a variable number of subsamples each consisting of 10% of the points, randomly chosen from the main dataset. Temperature curves are fit using each subsample. The average of the subsample fit temperatures is then used as the measured temperature, with the square root of the variance of the temperatures being used as an uncertainty. Typically, we find that variances will converge within 16 subsamples for most temperature measurements.

In order to decide on the proper windowing of data, we have developed a tool that assists in deciding which window contains the most information about the temperature while avoiding the non-linear region of the extraction. The extraction signal is partitioned with three markers by the user:

- t_-: A time in the base of the signal, where electrons have not started to extract.
- t_0: A guess of the time where extraction starts, when it is just above noise level.
- t_+: A time when the signal is clearly in the non-linear regime.

The best results usually occur when $t_0 - t_- \gg t_+ - t_0$ and $t_0 - t_-$ is much longer than the period of dominant noise in the signal, since the Levenberg-Marquardt routines generally perform better when it has a large base to establish the DC offset of the signal for fitting parameter B. The routine also uses the range $[t_-, t_0]$ to establish the expected noise amplitude of the acquisition. The routine then performs a bootstrap fit for data in the ranges $[t_-, t_0]$, $[t_-, t_0 + \Delta t]$, $[t_-, t_0 + 2\Delta t] \ldots [t_-, t_+]$ for some Δt. For each of these fits, the fit temperature, bootstrap-derived uncertainty, and average reduced chi-squared of the fit. The noise

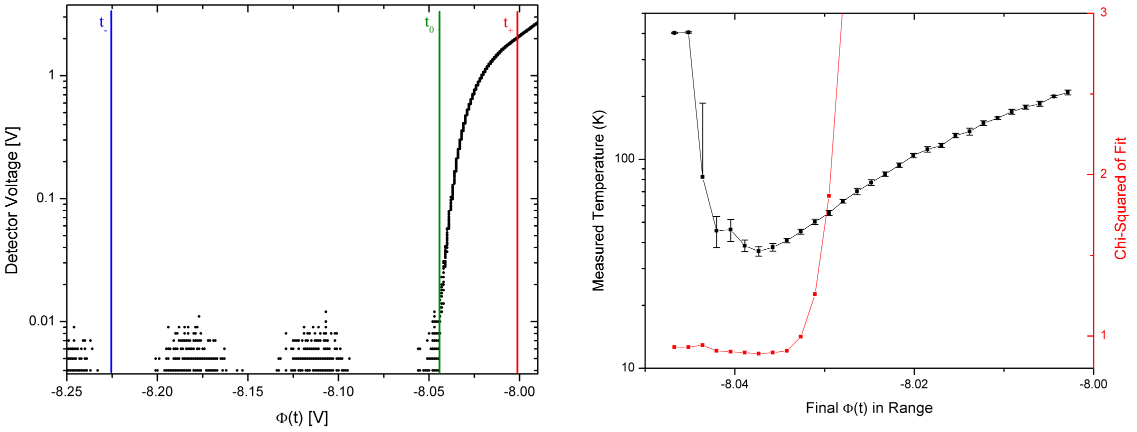

Figure 4.9: Typical temperature fitting routine results for a cold (39±4K) plasma extraction. On the left, the raw data for the extraction is shown with the user-selected partition points, rescaled to the voltage of the ramping electrode. Note that the curve has negative value for some regions due to a ripple in the signal and therefore does not appear in a log-scale graph. Bootstrap fitting is performed on the various ranges as described in the text, and the resulting temperatures/chi-squared values are shown on the right. The temperature is taken as the average of points in $[-8.042, -8.037]$, weighted by inverse-uncertainty.

amplitude is used as the expected variance for evaluating the chi-squared distribution. The ranges with large uncertainty in temperature and $\chi^2 \sim 1$ typically indicate that the model is overconstrained, therefore the range does not have enough information from the extraction to properly fit the temperature. Ranges with large χ^2 indicate an underconstrained model, where the measured extraction range is now in the non-linear regime.

Initial guesses for parameters are made using this partition as well. The parameters A and γ are determined by the slope and offset of $\log N$ in the $[t_0, t_+]$ partition, while the offset B guess is determined by the average of N in the $[t_-, t_0]$ partition. A good guess is necessary for faster convergence of Levenberg-Marquardt to the specified cutoff. While t_-, t_0, and t_+ need to be manually specified by the user, it is conceivable that an algorithm could be developed to automate this process for most plasmas observed.

In practice, there is usually a small range where the fitting routines simultaneously generate small uncertainties and $\chi^2 \sim 1$. In cold plasmas ($T < 500$K), the non-linear region is marked a dramatic increase in χ^2 where the value increases from ~ 1 to 10 over a relatively short (10mV) region of the ramp. While we do not have a good routine for determining the "best" temperature fit from these parameters, the good-fit region generally does not have a large variance in the temperature range. Either the weighted average of these values or the last point before the non-linear region occurs can be used.

GPU Accelerated Calculations with CUDA

Since a large number of curve-fitting attempts are needed in the above process, and larger datasets can require up to $\mathcal{O}(10^{10})$ floating point operations, the analysis process takes a long time to run on a standard processor. In order to expedite this analysis so that it can be performed as new data arrives, we parallelized components of the Levenberg-Marquardt algorithm. The algorithm does not lend itself to natural parallelization, however there are subcomponents of the routine such as computing gradients of the model curve with respect to fit parameters and large matrix multiplication operations that are relatively easy to run in parallel [28].

Code was developed using nVidia CUDA with the cuBLAS environment in C++ to load these sub routines onto the GPU. Special care was taken to minimize CPU-to-GPU memory transfer, since this can significantly slow the process. The analysis was performed with a nVidia GeForce 780 GTX GPU with 2304 cores. For large datasets, the routine was found to run at least 100 times faster with GPU assistance, making it possible to perform the computationally-intensive analysis above in seconds. The routine was written as a dynamic link library and as such is usable by either writing a short executable shell or directly inserted into LabVIEW routines, depending on the application.

Radial Profile Fitting Routine

As discussed in previous sections, it is useful to have an image of the projection of the plasma during extraction since the radial profile is need to properly model the self-fields of our plasma. This can be used to predict resonant Trivelpiece-Gould modes, establish corrections to the temperature measurement routine, measure heating due to plasma expansion, and watch for undesirable instabilities such as unstable diocotron modes. In order to perform these calculations quickly, it is useful to fit the image of the plasma to a analytic function for which these quantities can be more easily solved.

An analytic function of the form,

$$f(\mathbf{x}) = A \exp\left(-\left(\frac{|\mathbf{x}-\mathbf{x_0}|}{r}\right)^n\right) + B, \tag{4.6}$$

was chosen to represent the plasma fit. Note that this model includes six fitting parameters: the center location of the plasma $\mathbf{x_0}$, the radius r, the peak density A, the offset B, and a flatness parameter n. The offset, B, is treated as a background from the camera and subtracted from the final distribution. This near-gaussian form is used since trapped plasmas are typically azimuthally symmetric and, when projected along onto a transverse image, can vary from a flattop profile ($n \geq 5$) for very long plasmas to a Gaussian-like ($n \approx 2$) profile for short plasmas. There is *no theoretical justification* why plasmas should take this general form, but it has proven to be a robust form that matches many of the observed radial plasma distributions we encounter.

However, since this fitting routine has a large number of parameters and there are over 10^6 pixels used as data points, a large number of numerical-intensive iterations are required to find the best fit. We have developed techniques to reduce the number of parameters of this fit, reducing the chance that the fitting routine will stumble into a local residual-minimum that does not reflect the true distribution.

Center-Finding Algorithm: Minimal Azimuthal Variance

The first step to reducing the number of fitting parameters is to find the center of the plasma. Intuitively, it would seem that this could be done using a center-of-mass calculation, but this requires prior knowledge of the offset and the assumption that the extracted plasma lies entirely on the imaging plate, which is not the case for larger radius distributions. Instead, we have chosen to evaluate for a point of minimum azimuthal variance in the distribution from an assumed center, $\mathbf{x_c}$. This value is generated by splitting the data into subsets $\mathcal{R}_i$ based on individual pixel locations $\mathbf{x}$:

$$\mathcal{R}_i = \{\mathbf{x} \mid i \leq |\mathbf{x}-\mathbf{x_c}| < i+1\} \tag{4.7}$$

The intensity of the pixel at $\mathbf{x}$ in the image is written as $I(\mathbf{x})$, and the number of pixels in each set $\mathcal{R}_i$ is written as N_i. The azimuthal variance at a point $\mathbf{x_0}$ is defined as,

$$\sigma_\phi^2 = \frac{\sum_i \sum_{x\in\mathcal{R}_i} (I(x) - \mu_i)^2}{\sum_i N_i} \tag{4.8}$$

where μ_i is the average of $I(\mathbf{x})$ for $\mathbf{x} \in \mathcal{R}_i$. The value of σ_ϕ^2 can be thought of as a measure of the cocentricness of the plasma about the test point.

A grid of test points is placed over the image area, and σ_ϕ^2 is evaluated at each of these points. The point with minimum value is considered the best fit for the center. Rather than spending a large amount of resources to generate a fine grid, a course grid can be made, a solution found, and the process reiterated with a finer, more localized grid. This measure was found to be incredibly robust for plasmas with a moderate azimuthal symmetry, even with large fractions of plasma not hitting the microchannel plate due to poor steering.

Center-Finding Algorithm: Gradient Vertex Detection

An alternate method for finding the center of the distribution is to use a algorithm similar to vertex detection methods [58]. Here, the local gradient of the image intensity is calculated on a grid and the point that minimizes a weighted distribution of distance to the gradient axes is chosen as the center point. This method is faster than the minimum axial variance method and can be used to detect multispecies extraction profiles, but it occasionally performs poorly if the plasma image is very occluded or the plasma is too small due to the sampling grid.

Solving the Near-Gaussian Fit

Once the center is determined to good confidence with either of the previous algorithms, it is fixed and the data is converted to a one-dimensional dataset using the distance from the center as an independent variable. Once this is done, the data is fit to a four-parameter curve,

$$f(x) = A \exp\left(-\left(\frac{x}{r}\right)^n\right) + B, \tag{4.9}$$

using a Levenberg-Marquardt algorithm. This process can be made faster by using a weighted fitting routine where the averages and inverse square roots of variance for each $\mathcal{R}_i$ are used as the dependent variables and weight respectively. Example fit solutions are shown in Fig. 4.10.

If a GPU is available, there is enough processor power to generally leave the center location as a fit parameter, while using the value found above as an initial guess, and to use the Levenberg-Marquardt directly on the set with two-independent variables. Additionally,

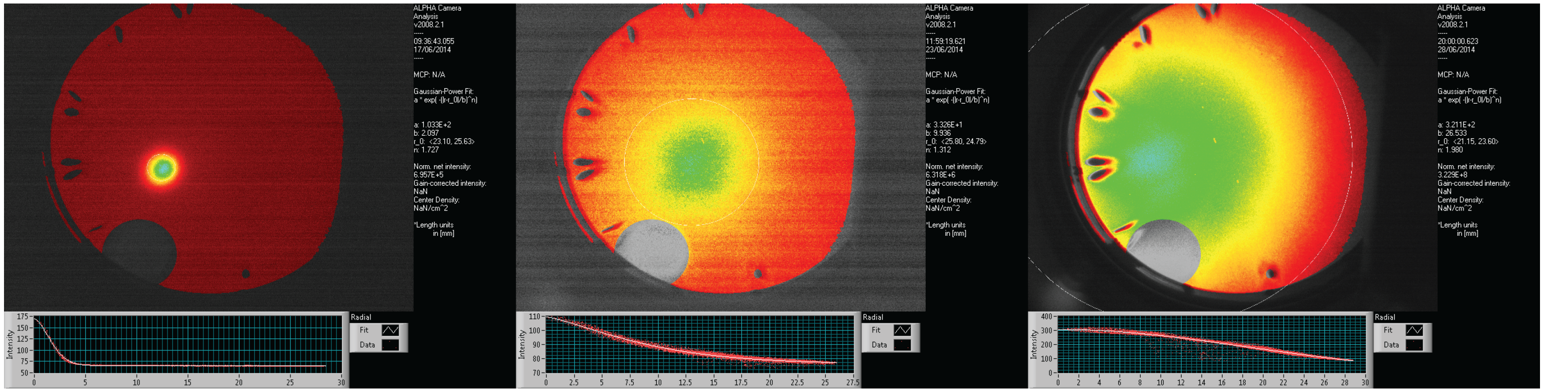

```
ALPHA Camera
Analysis
v2008.2.1
-----
09:36:43.055
17/06/2014
-----

MCP: N/A

Gaussian-Power Fit:
a * exp( -(|r-r_0|/b)^n)


a: 1.033E+2
b: 2.097
r_0:  <23.10, 25.63>
n: 1.727

Norm. net intensity:
6.957E+5
Gain-corrected intensity:
NaN
Center Density:
NaN/cm^2

*Length units
         in [mm]
```

```
ALPHA Camera
Analysis
v2008.2.1
-----
11:59:19.621
23/06/2014
-----

MCP: N/A

Gaussian-Power Fit:
a * exp( -(|r-r_0|/b)^n)


a: 3.326E+1
b: 9.936
r_0:  <25.80, 24.79>
n: 1.312

Norm. net intensity:
6.318E+6
Gain-corrected intensity:
NaN
Center Density:
NaN/cm^2

*Length units
         in [mm]
```

```
ALPHA Camera
Analysis
v2008.2.1
-----
20:00:00.623
28/06/2014
-----

MCP: N/A

Gaussian-Power Fit:
a * exp( -(|r-r_0|/b)^n)


a: 3.211E+2
b: 26.533
r_0:  <21.15, 23.60>
n: 1.980

Norm. net intensity:
3.229E+8
Gain-corrected intensity:
NaN
Center Density:
NaN/cm^2

*Length units
         in [mm]
```

Figure 4.10: Examples of fitting routine solutions for a variety of plasmas. For each plasma extraction, a picture is taken by a high speed camera (*shown in false color*). The image is masked (*greyscale*) to only permit data from active and calibrated regions of the detector. Using the fitting routines described in this section, the curves are fit to the near-Gaussian model. The result is shown in the graphs below each image where the best-fit curve (*white*) is overlayed with the datapoints (*red*). The first e-folding radius is shown in each image by a white circle. Note that even for the large image on the right, a fit is still obtained despite a good fraction of the plasma missing the detector.

binning is not necessary, so data no longer needs to be averaged to fit to the curve. Convergence typically happens within 500 cycles of the algorithm, including steps that fail to decrease the residual. Constraints must be placed on $r > 0$ and $n > 1$ to prevent the model from finding a false minimum. The image of the plasma (1024 x 1024 pixels) takes at most 3 seconds to fit with this technique.

Special thanks goes to Lenny Evans, who translated my old code to GPU-accelerated code for use in image-fitting routines in our lab, as well as diagnosing and solving the problems associated with the algorithm tending to step towards a bad region in parameter space.

Chapter 5

Measurement of Resonant Cooling

Resonant behavior between cavity modes and confined magnetized electrons has previously been studied in systems with a relatively low number of confined electrons $N < 10^5$ by Tan and Gabrielse [75], however for many experiments it is useful to generate cold samples of millions of leptons. It is unclear how the resonant behavior scales to a large number of particles since the linewidth of the resonance was observed to broaden and shift. In addition, while confined electrons are coherently resonant for a small number of electrons, as in Tan and Gabrielse's experiment, it is suspected that they instead behave as a classical ensemble for larger numbers. In this chapter, we present the demonstration of enhanced cooling for a large number of confined electrons in an electromagnetic cavity.

The majority of data presented here was collected in the last two weeks of my time at Berkeley, and should be regarded as preliminary results. Many of the observed behaviors are not well-explained by the models presented in this thesis, but I anticipate that a significant amount of work will be done by future students in the group to characterize this behavior. Special recognition goes out to Eric Hunter, a fellow graduate student, who has been rapidly collecting this data as I run the analysis and write this thesis.

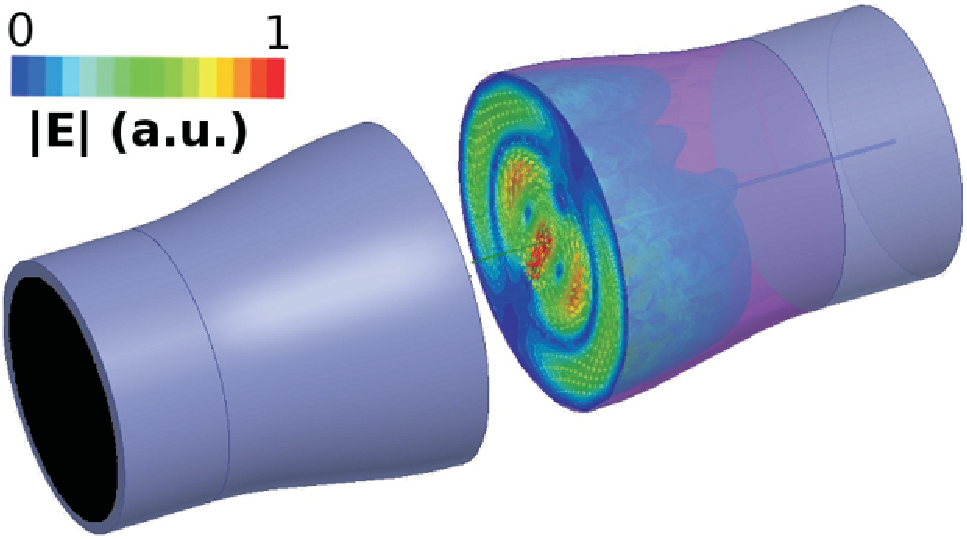

Figure 5.1: Plot of the magnitude of the electric field, $|\mathbf{E}|$, associated with the TE_{131} cavity mode. This calculation was performed by Hardy and Evetts.

5.1 Cooling in the Bulge Cavity

In the following experiments, we use the bulge cavity module to demonstrate cavity enhanced cooling. The bulge cavity is described in detail in Sec.3.8. There are many advantages to operating in the bulge over the standard cavity. First, the mode structure is sparser, due to the smaller geometry of the inner electrodes walls in this region; this allows for less potential overlap between cavity modes that can complicate the measured spectrum. Second, the reduction in radius from the main cavity region isolates the bulge cavity electrodes from low-frequency electrical noise in the cavity since the contribution of electrostatic potential from neighboring electrodes along the trap axis is highly attenuated. Finally, if the bulge is used for cavity cooling, the main cavity can be used as a trapping reservoir for a large number of electrons. We can transfer approximately one million electrons into the cavity at a time, such that the cooling experiment can be repeated about once every two seconds, allowing for higher frequency resolution when searching for peaks when the magnet is set to ramp at a fixed rate.

There is one other important reason that cooling was attempted in the bulge. One of the in-vacuum induction coil leads on the cavity doors became disconnected during routine operation, slowing the speed which the door could be opened and closed. Opening the door sallows radiation to leak into the main cavity, reducing the effective Q and exposing the cavity to warmer regions of the vacuum system. This can reheat the electron plasmas stored in the main cavity on the classical cyclotron time scale, effectively masking the enhanced cooling of the cavity by the time electrons can be extracted to the imaging assembly. The bulge electrode geometry is expected to block most strongly-resonant external radiation.

The bulge is nearly cylindrical, so we use the cylindrical cavity mode naming conventions ($\mathrm{TE_{nmp}}$ and $\mathrm{TM_{nmp}}$) to describe the cavity modes in the bulge. The values n and m correspond to the radial and azimuthal wave indices, respectively. Since the ends of the bulge cavity are largely open, the modes that are trapped within the structure, with reasonable Q, have small values the axial wave number p. Modes with larger p leak out of the cavity, despite reduced radius at either end. The ”leakiness” of most confined modes is calculated to be much less than the attenuation due to the electrode surface resistance, making contribution from external radiation negligible. The cavity was designed by our UBC collaborators, Evetts and Hardy, with the $\mathrm{TE_{121}}$ and $\mathrm{TE_{131}}$ modes, as the primary targets for enhanced cooling. These modes were tuned to have $Q \approx 2500$ when empty to allow for a single particle cooling rate enhancement, or Purcell factor with geometric correction,

$$F_p = \frac{6\pi c^3}{\omega_c^3 V} \frac{|\mathbf{E_0}|^2}{\langle |\mathbf{E}|^2 \rangle} Q, \tag{5.1}$$

compared to a free, magnetized electron. Here, $\frac{|\mathbf{E_0}|^2}{\langle |\mathbf{E}|^2 \rangle}$ is taken to be the of the ratio of the square of the electric field in the mode at the plasma location to the average electric field squared over the entire cavity.

It should be noted that when these measurements were taken, one of the leads to the outside bulge electrodes (E2) had become disconnected inside the vacuum system, so the electrostatic potential was not well known. Observations were made by looking at fast extraction signals that the electrode maintained a relatively fixed voltage over extraction, but this also indicated that while the plasma was trapped in the bulge, the axial extent of the plasma was not known.

5.2 Locating Resonant Cavity Modes

In order to observe enhanced cooling, cavity modes must have significant overlap with the cyclotron frequency of electrons in the trap. Since the cavity geometry is fixed, the cyclotron-cavity resonance must be tuned by adjusting the magnetic field generated by the superconducting solenoid. At lower magnetic fields ($< 1.5T$), the magnet is ramped using a Lakeshore 625 magnet power supply, with 0.1mA ($\delta B = 25$mG) resolution. This corresponds to a resolution in the cyclotron frequency of $\delta f_c = 70$kHz. At a field of 1.0T, this gives a resolution of 1 part in $4 \cdot 10^5$. The absolute field of the magnet is known only to 1% near the center of the trap, due to a combination of superconductor hysteresis [43] and signal scaling uncertainty in the power supply. The field however is assumed to scale with an external hall probe, used to monitor magnet ramping operations.

Resonances are detected by measuring the temperature relaxation curve of a confined electron plasma in the bulge cavity after the plasma is heated. In order to perform this operation faster, the temperature needs only be found for a given relaxation time, so long as initial plasma temperature and profile are repeatable. The fixed relaxation time must

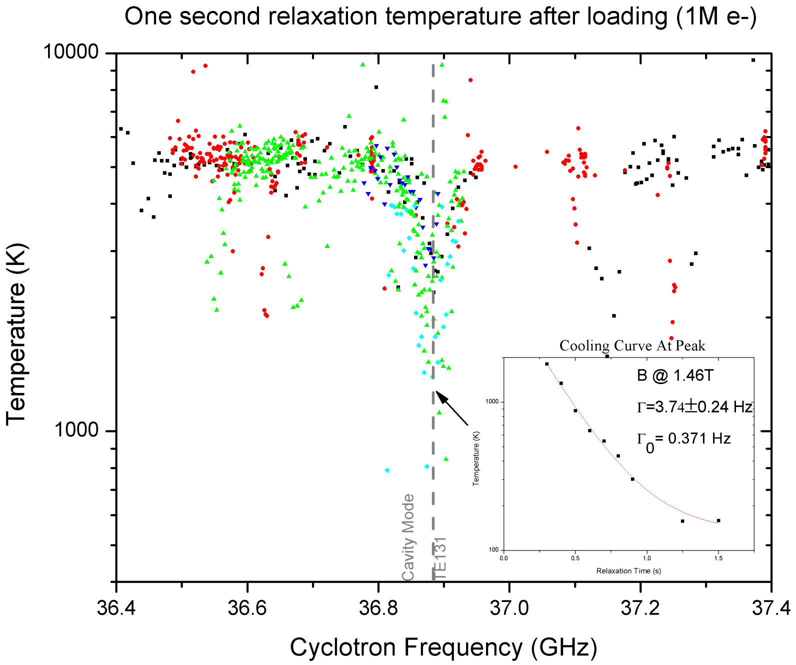

Figure 5.2: This plot shows a cyclotron-cavity cooling peak by measurement of the relaxation temperature of a 1M electron plasma. When the cyclotron frequency overlaps a cavity mode, electron plasmas injected into the cavity experience higher cooling rates by resonant coupling with the cavity mode, resulting in lower temperatures after a fixed relation time. Fixing the magnetic field at the peak, a cooling curve is taken. In this case the cooling is enhancement factor $\Gamma/\Gamma_0 = 10$. Different colors correspond to individual magnetic field sweeps through the resonance.

also be short enough that plasma expansion effects do not contribute a significant amount of energy to the plasma.

In our case, the "heating" procedure takes the form of the plasma injection itself since the injection procedure produces plasmas with repeatable number and temperature. As mentioned, the electrons are injected by loading the main cavity with a large number ($N \approx 200M$) of electrons. The main cavity electrostatic well is lowered until a small number of electrons (tuned to 1.00±0.10M) escape along the axis of the trap. The electrons flow toward the bulge cavity where they are confined in an electrostatic well. This cycle is repeatable for roughly 20 shots before the plasma parameters begin to drift, and the cavity well must be reloaded.

Operating near 1.0T, the free-particle relaxation rate is expected to be 0.19s^{-1}. Once injected, we allow the plasma to relax for $t_R = 1s$. This is enough to resolve locations of enhanced cooling in the cavity since resonantly cooled plasmas will tend to cool at least one

Mode n, p	Calculated Freq.	Measured Freq.	Linewidth (FWHM)	Cooling Enhancement
2, 1	21.66 GHz	21.70 GHz	15 MHz	1.4
2, 3	25.449 GHz	25.48 GHz	70 MHz	2.0
3, 1	33.908 GHz	33.838 GHz	60 MHz	2.0
3, 2	36.58 GHz	36.652 GHz	70 MHz	4
3, 3	38.62 GHz	38.64 GHz	90 MHz	10
3, 4	40.264 GHz	40.404 GHz	90 MHz	2.3

Table 5.1: Measured TE_{n1p} cavity mode cooling resonances.

e-folding, while plasmas out of resonance will not significantly relax. Allowing the magnetic field to scan at $dB/dt = 1.25 \cdot 10^{-5}$T/s, we are able to acquires traces such as those shown in Fig. 5.2. The plasma temperatures are measured destructively by reading the time-of-arrival of electrons on the imaging assembly as described in Sec. 4.3. Once a peak is found, the magnetic field can be fixed to the peak location. The cooling rate is found by repeating the previous measurement with a fixed field, but allowing the relaxation time to vary.

5.3 Characterization of Cooling Behavior Near Modes

Once we locate a candidate cooling peak, it is of interest to characterize the bandwidth and lineshape of this resonance. In order to do this, we adjust the magnetic field to make displacements of the cyclotron frequency relative to the cavity mode. A cooling curve of the plasma is taken by measuring the temperature of a plasma at a number of relaxation times $0\mathrm{s} \leq t_R \leq 3\mathrm{s}$ after heating. Cooling curve measurements are alternated with $0.5s$ relaxation time shots to ensure loading stability from the reservoir. The measured temperatures are fit to an exponential function with offset, $A \exp(-\Gamma t) + B$. The best fit for the parameter Γ is the measured cooling rate of the system.

Care must be taken when sweeping the magnetic fields for these curves since hysteresis in the ramp can shift the location of measured peaks. The magnetic field is monitored by a hall probe in the fringe region of the solenoid to ensure repeatability in the field strength during scans.

We have identified cooling peaks associated with the cavity modes TE_{121}, TE_{123}, TE_{131}, TE_{132}, TE_{133}, and TE_{134}. These are shown in Table 5.1. The TE_{121}, TE_{123}, and TE_{131} had a factor of ≤ 2 cooling enhancement at the peak center, suggesting that the modes may be strongly saturated with 10^6 electrons since the empty cavity linewidth predicts a factor of 1000 enhancement in cooling. The final mode, TE_{133}, however was found to exhibit a factor of at least 10 in the cooling rate. It is unclear why this mode behaves significantly differently, but this may be due to better geometric localization of the mode to where the plasma is confined.

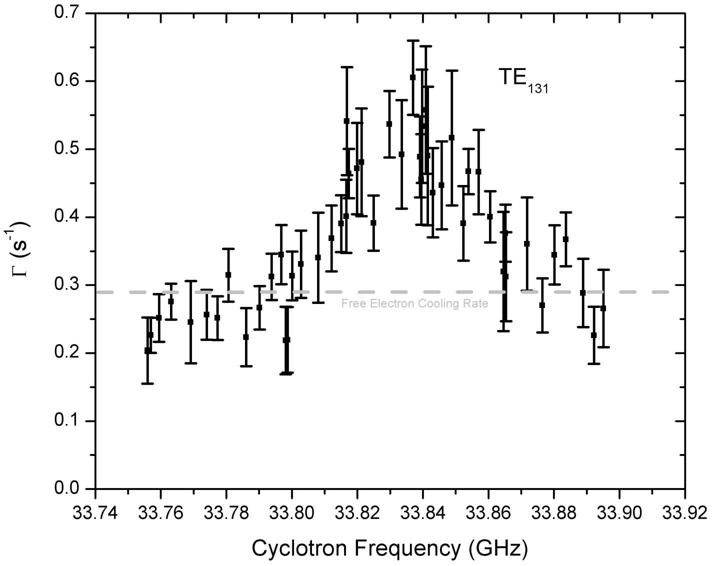

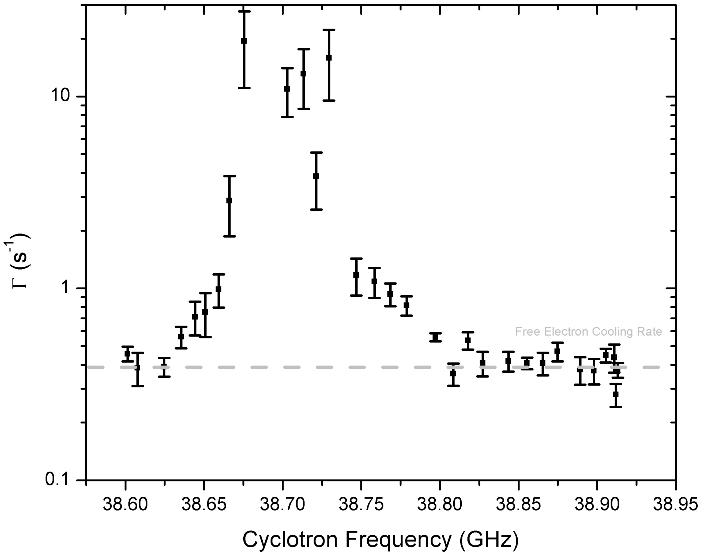

Figure 5.3: Examples of measured cooling rate lineshape and bandwidth for interacting TE modes; note that for visibility the TE_{133} is on a logarithmic scale. Γ is the e-folding rate for the temperature relaxation. Cooling rates for points with $\Gamma > 5\mathrm{s}^{-1}$ may be unreliable since the curve cools below our preliminary analysis routine noise floor within 0.2s and the plasma does not warm to the same temperature under the heating operation at the center of the peak. This suggests extremely rapid cooling, but it is difficult to quantify Γ for these points with the preliminary results.

5.4 Cavity Mode Saturation

As described in Sec. 2.2, the cooling rate is expected to depend on the number of confined particles. This is because cyclotron emission is emitted into the cavity and can be reabsorbed by other resonant electrons in the distribution. From the previous discussion, we expect this effect to manifest when the rate of rate of photon absorption by the walls of the cavity is comparable to the rate of cyclotron radiation times the number of electrons ($\Gamma_c \sim N\Gamma$). This can be found by evaluating,

$$N \sim \frac{\Gamma_c}{\Gamma} = \frac{\omega_c}{2Q}\frac{1}{F_p\Gamma_f}, \tag{5.2}$$

where Γ_f is the free electron emission rate. Assuming non-coherent emission, this is expected to generally occur when $N \sim 2 \cdot 10^6$ for many of the lower-order modes in the bulge cavity.

In order to observe saturation, the magnetic field is ramped to a resonant mode peak found using the procedure in Sec. 5.2. Once at this location, a temperature-relaxation time curve is taken for different confined electron numbers, ranging from 10^6 to $5 \cdot 10^7$. In order to vary the number of particles, injection into the bulge is no longer a pulsed operation, but a full transfer of a plasma captured in the main cavity. Since different numbers of electrons are loaded and electron density affects the self-field and loading behavior, the plasmas do not share identical radial profiles or initial temperatures upon injection. A plot demonstrating saturation is shown in Fig. 5.4, resolved at the peak in Fig. 5.2.

While cooling behavor was observed, the saturation effects do not match our expected predictions for the behavior of the system. The cooling rate appears to saturate for a higher number of confined electrons, but not at the electron number predicted by the model in Sec. 2.2. There is also an anomolous dip in the cooling rate between $3 \cdot 10^6$ and 10^7 confined charges. We propose two possible explainations for this. First, the cavity mode frequency is expected to shift with the number of confined particles since adding resonant particles reduces the effective Q of the cavity. Since the magnetic field is held constant during this operation, the cavity mode has the potential to shift away from the cyclotron frequency. The dynamics of this shift and evaluation of the equilibrium condition will require better modeling of the system and is beyond the preliminary analysis presented here. Increaing the number of electrons in the cavity also extends the length of the plasma in the cavity from self-field effects. This allows for the possibility that additional nodes in the mode structure are now accessible to the electrons, increasing the average $|\mathbf{E}|^2$ over the plasma volume and therefore the average cooling rate of particles in the trap.

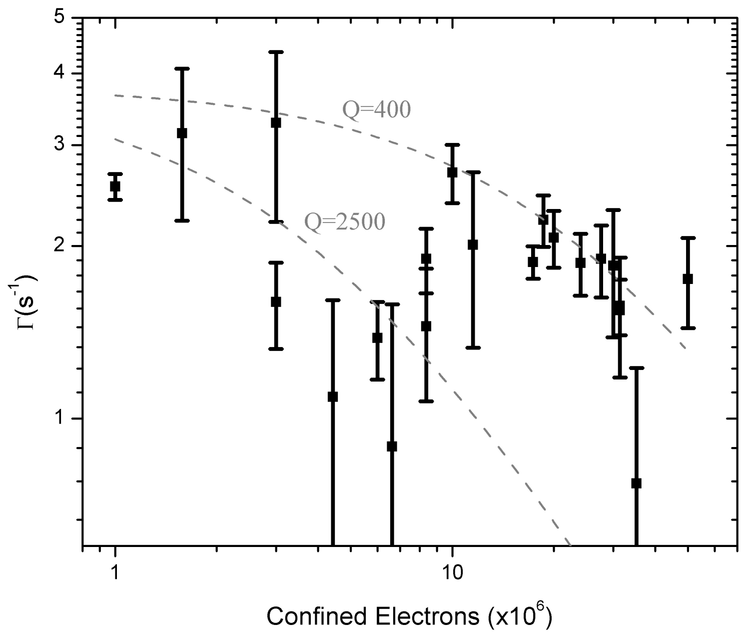

Figure 5.4: The measured cooling rate as a function of electrons confined in the bulge region. The data is taken at constant field close to the center of a resonance peak. Theory curves for an assumed single particle cooling rate of $\Gamma = 3.8\text{s}^{-1}$ are shown for the resonant cavity modes with $Q = 400, 2500$. These calculations do not include the shift of the mode relative to the cyclotron frequency due to stronger coupling to the ensemble.

Chapter 6

Experiments in Cold Electron Plasma Manipulation

The measurement of enhanced cooling was a success, but this required characterization of plasma behavior in the trap to order to prepare appropriate sequences for manipulating the plasma. While learning about plasma manipulations in the trap, we encountered a variety of behaviors that were either unexpected or poorly characterized. In this chapter, a series of small experiments and observations about a selection of these peculiarities is discussed.

Use of the "rotating wall" technique, for modifying the radial profile of confined non-neutral plasmas does not have a known general theory to describe observed expansion and compression behavior. In section 6.1, we present a measurement of compression for various drive parameters and plasma displacements in the regime where the gradient of the electric field is on the same order as the size of the confined electrons, an unusual regime for this behavior.

One of the major suspected sources of background heating is radio frequency noise parasitically coupling into the trap. Applied signals pass thorugh multiple filters before entering the vacuum system to ensure that low noise is applied to the electrode leads, however it is a concern that transients could still capactiviely couple through the grounding chassis of the experiment into coaxial cables. In an effort to see if this heated the plasmas we characterized noise generated by various instruments and the observed effect on plasma temperature in section 6.2.

Finally, in section 6.3, we discuss an anomalous behavior when running the plasma temperature diagnostic, where the charge did not always extract as the curve predicted for a Maxwellian distribution. We suspect that this is due to an autoresonant excitation of the plasma on extraction which may prove useful for certain plasma applications.

6.1 Rotating Wall Compression on Short, Rigid Plasmas

For many applications, the density and radius of confined plasmas must be modified to optimize certain plasma behaviors. Originally developed as a technique for reducing particle losses in non-neutral plasma traps from background gas and resistive wall drag[20], the *rotating wall* is a robust technique for manipulating the radial profile of confined, non-neutral plasmas in a Penning trap configuration [25]. This technique relies on the property that non-neutral plasmas, in equilibrium, rotate about the central axis of the trap due to the $\mathbf{E} \times \mathbf{B}$ drift motion generated by the combination of the electrostatic trapping potential and self-field of the trapped particles. Disregarding drag effects in the systems, the angular momentum about the central axis of a plasma is a conserved quantity. When torque is applied to the plasma, the plasma will reequilibriate to a state with higher or lower density depending on the torque, to match the drift motion condition; this takes the form of a radial compression or expansion of the plasma in the presence of axial confining fields.

In the rotating wall technique, torque is applied by applying a transverse, rotating electric field in area where the plasma is confined. The rotation comes from application of phase-locked RF signals applied to a special electrode in the trap that has been azimuthally split into sectors. The phase of the signals applied to each sector is offset such that the electric field experienced by the plasma is constant in magnitude, but rotates at the RF frequency. This drive generates an azimuthal perturbation, δn, in the plasma that is effectively phase-offset from the drive direction. Given this behavior, $\tau = \langle \delta n \cdot \mathbf{r} \times \mathbf{E} \rangle$ will be the effective torque on the plasma. Although the specifics of the dynamic formation of the δn perturbation have not been well-modeled in many regimes, the technique is generally usable when the RF signals are applied to the confining electrodes, or edges, of the plasma and have a frequencies near $m_\theta \neq 0$ finite-length Trivelpiece-Gould modes of the plasma [25].

Unfortunately, since the dynamics of the δn-perturbation are not well known, it is difficult to optimize the rotating wall drive parameters for a general plasma. In a recent example, explored by Surko's group at UC San Diego, it has been found that applying a larger amplitude signal can alter the compression behavior into a strong-drive regime where the drive can still compress when far away from the Trivelpiece-Gould frequencies [18, 44]. Specifically, in our device, due to a restriction in the number of electrodes we wanted to use for compression operations, we found that the general perturbative drive technique for applying the rotating wall fields to the edge of the plasma were inapplicable because the axial extent of the rotating wall fields $(E_\perp/\partial_z E_\perp)$ were comparable to the axial size of our confined electron plasma. Here we describe a set of compression experiments in a regime where pure electron plasmas with length smaller than the electrode length scale and compare the effectiveness of compression to longer, traditional trapped electron plasmas.

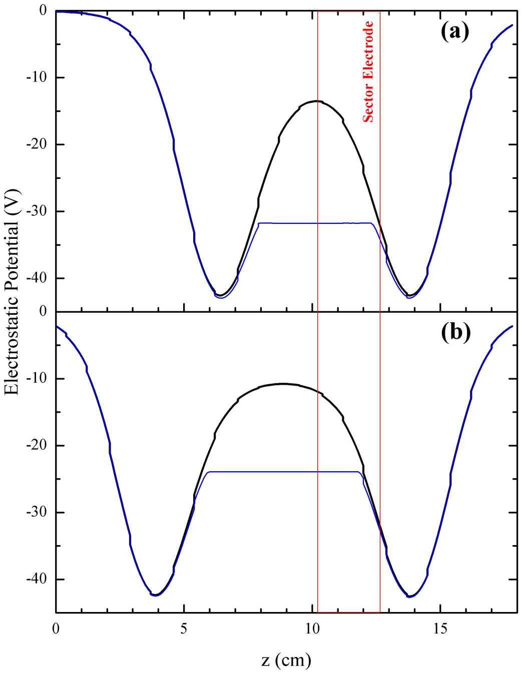

Figure 6.1: Electrostatic potentials for confinement wells with two (a) and three (b) inner electrodes. The potentials are shown for an empty well (*black*) and with the self-fields of 40M confined electrons (*blue*). The location of the sectored electrode is shown in by the red box.

Compression Procedure

Electrons were injected into the electrode stack with a homogeneous magnetic field of $B = 3.00$T. Electron plasmas were captured by lowering an electrostatic potential well in the path of a reflected electron beam. In this way, we were able to repeatably capture a set number of particles to 2% repeatability, calibrated to the final depth to which the potential is lowered. Once captured, the particles were gently transported into a well shape that closely matches a harmonic potential. Regardless of the location of the well, one of the confining electrodes was always the sectored electrode, in order to allow the plasma to be driven by the rotating wall fields. Changing the axial length and transporting the plasma did not produce significant changes to the radial profile.

Once the plasma was positioned in the storage well, the rotating wall is applied at a constant frequency, f_{RW}, and amplitude, V_{RW}, for a set amount of time. We performed scans of compression behavior for different drive frequencies, and the final radial profiles and final peak densities were recorded. Radial profiles and temperatures are determined by destruc-

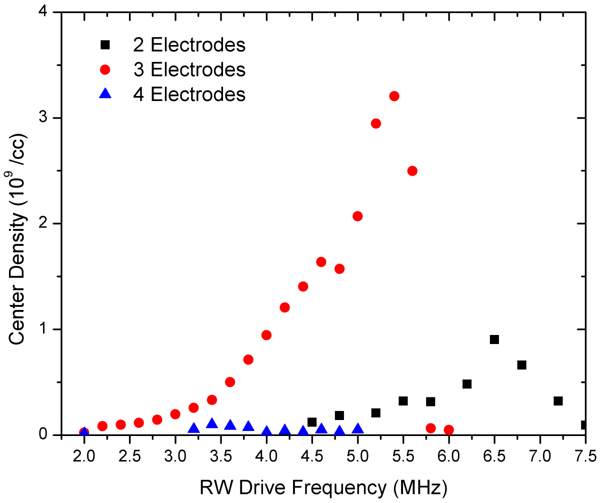

Figure 6.2: Peak density of plasmas compressed using a constant rotating wall drive of constant frequency and amplitude. Plasmas were confined in simple confinement wells with two, three, and four inner electrodes.

tively imaging the plasma on a microchannel-plate phosphor assembly. A wide range of amplitudes was used, ranging from the perturbative to strong drive regimes; typically strongly-driven plasmas would compress to a final state much faster ($\leq 10s$), but no extensive study was done on to characterize this behavior. Once the drive was removed, most compressed plasmas would slowly expand to a larger radius at an initial rate of $dr/dt \approx 100\mu$m/s. Compressed plasmas consistently equilibrated at temperatures ≥ 2000K when strongly-driven.

Compression in Different Length Confinement Wells

Compression in the strong drive regime was compared for various simple confinement wells. The sectored electrode is placed as the rightmost, inner electrode in the well, so that the rotating wall field is applied asymmetrically to the edge of the plasma. The electrostatic potential is shown in Fig. 6.1. The confinement well was loaded with $N = 40.0$ million electrons and a rotating wall field of $E_\perp = 200$mV/cm is applied on the axis of the trap for 10 seconds. The peak locations of compression, shown in Fig. 6.2, correspond to the $m_\theta = 1, m_z = 1$ excitation of Trivelpiece-Gould mode frequencies for the plasma in the particular geometry. It is noted that the peak compression varies for the number of inner electrodes used, however this is believed to be an effect of the position of the rotating wall electrode with respect to the edge of the plasma as discussed in the following section.

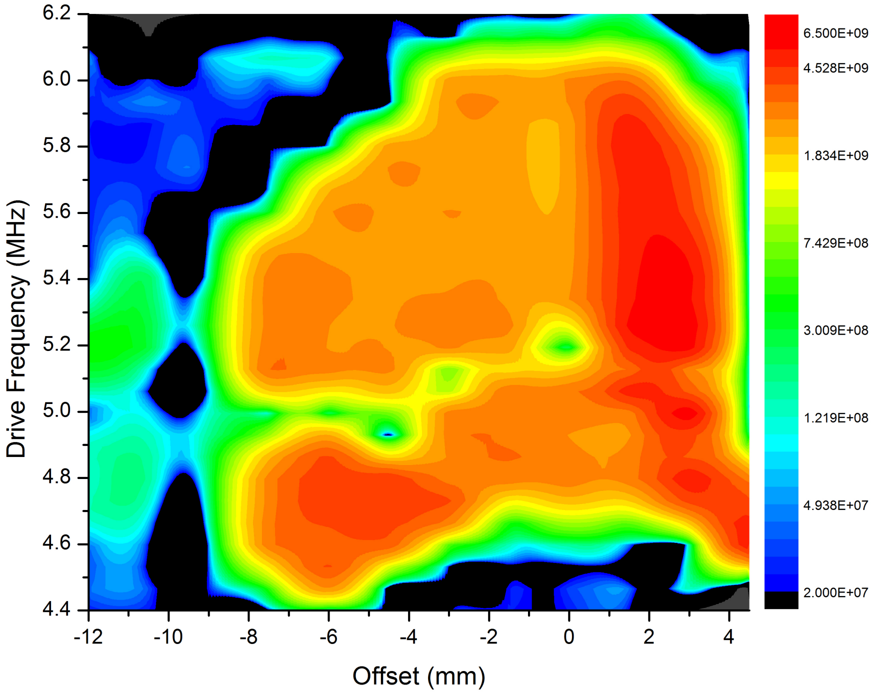

Figure 6.3: Peak density (*logarithmic color scale*) of the compressed plasma as a function of drive frequency and offset position of the center of the plasma relative to the sectored electrode boundary. The compression is driven with a 5V amplitude for 10s, corresponding to a central electric field of 1V/cm. Errors in the density measurement are under 10%, largely determined by statistical fits of the radial profile shape of the distribution for the smallest radius plasmas.

For stronger drives, the compression happens on a much faster rate, $\propto V_{RW}^2$, [44] such that a wide range of frequencies were observed to compress the center of the plasma beyond 10^9/cc in under 5sec. By reducing the number of particles in the well, the lengths of the confined plasmas are reduced, the the plasma exposure to the rotating wall field has changed, eventually allowing the two inner-electrode wells to perform better for compression when $N \leq 10$ million electrons.

Compression Scaling with Location

We studied compression of a short plasma without a long support column of unperturbed transverse fields, where instead the entire plasma was exposed to the rotating field. For this measurement, $N = 5.0$ million electrons, mimicking a desired compression procedure for the ALPHA collaboration. Short storage wells, consisting of two low electrodes surrounded by two confining potential electrodes, generated a the harmonic potential that, at the confinement potential minimum, had $\partial^2\Phi/\partial z^2 \sim 2.4\text{V/cm}^2$ along the axis of the electrodes. Using a zero-temperature waterbag model solver for the self-consistent density-field distribution, this plasma, with the initial measured radial profile of $\sqrt{\langle r^2 \rangle} \approx 1.8\text{mm}$, was calculated to have a axial length of $1.65 \pm 0.05\text{cm}$. From the measured radial profile, we infer that the trapped plasma resembles an elongated football rather than the ellipsoidal shape typically used to estimate plasma behavior [22].

The plasma location can be shifted by adjusting the electrostatic potentials on the potentials of six electrodes neighboring the confinement well, maintaining the z^2 through z^4 coefficient terms of the potential about the desired center of the trap. The resulting compression behavior is shown in Fig. 6.3. The center of the confined plasma was offset relative to the sector electrode, with $z = 0$ centered on the edge of the sector electrode and a neighboring electrode. The rotating wall drive was most effective when about 65% of the plasma was located under the sectored electrode, and it appears that as the plasma is moved to this location, it enters a strong-drive regime where the compression becomes less-frequency dependent over a 10s timescale. While there is no detailed model available describing why this is the optimal location, a simplified explanation may be that $\partial E_\perp/\partial z$ generates a distortion in δn over the length of the plasma, tilting the plasma slightly. Assuming this was a linear relationship, the maximum torque would occur when $E_\perp \cdot \partial E_\perp/\partial z$ is maximized over the entire plasma. The plot of this shown in Fig. 6.4, and suggests that this is a plausible explanation for why maximum compression is observed in this location.

Additional observations

For a certain range of frequencies (1.8MHz $\sim$ 3.2MHz), the application of the rotating wall would leave the plasma in a compressed state, but off-axis from the center of the trap. In this state, the plasma exhibited a diocotron motion stable over the scale of seconds about the center of the trap. This was found to be due to a peculiarity in filterboard used to high-pass signals to the electrodes. Specifically, a pole due to an LRC component in the circuit, typically near $f_{RW} = 2.6\text{MHz}$ was driving a phase-shift in the transmitted signals that varied amongst the sectored electrodes. This behavior can effectively drive the plasma off-axis since the transverse electric field geometry now has a off-axis maximum. We corrected this behavior by adjusting the inductance of the diocotron-suppression bypass in the circuit to move the pole to a lower frequency.

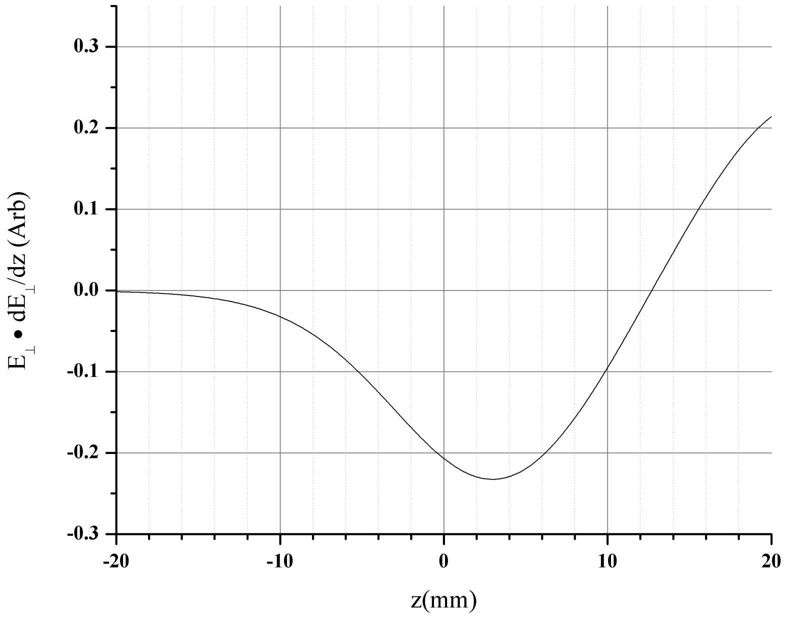

Figure 6.4: The transverse electric field times the gradient in the axial direction of the rotating wall drive as a function of the offset of the center of the plasma from the edge of the sectored electrode. This matches the offset definition in Fig. 6.3.

6.2 Plasma Interaction with Instrumentation Noise

The ability to generate low-temperature distributions of confined non-neutral plasmas is necessary for many experiments where the charged particles are used for application such as sympathetic cooling and recombination with other trapped species, such as performed in the antihydrogen synthesis experiments [9, 33], and spectroscopic analysis of materials with cold positron beams [13]. While many non-neutral plasma trapping experiments can generate low-temperature distributions with either a small number of trapped particles ($< 10^4$) [38] or by driving internal states, such as with laser-cooling, the ability to reliably cool pure lepton plasmas down to the temperature of the confining electrodes has proven elusive.

Electron plasmas, in many confinement experiments, tend to equilibrate at much higher than the expected background temperature of the electrodes. This means that either there is additional energy being driven into the plasma either through non-neutral plasma dynamics, such as joule heating [15], or that additional noise is being driven into the electrodes such that the mean electromagnetic energy in the system is not in thermal equilibrium with the material temperature of the system. In both non-neutral plasma traps in Berkeley and in CERN, the empirical expansion rate of the plasmas from background collisions and resistive drag accounts for only a small fraction ($\leq 10\%$) of the heating required to maintain trapped plasmas at their observed high temperatures, assuming free-particle Larmor radiation rates. While part of this may be due to saturation effects in the confining cavity suppressing the cyclotron cooling, there was also found to be a significant contribution due to heating from noise introduced by instruments used to monitor and operate the experiment.

Instrumentation Noise and Switching Supply Transients

Much of the electrical noise in the lab can be traced back to switching supply transients for various instruments. The transients from this noise cause ringing in the frequency range of 5MHz to 50MHz on the grounding plane of the experiment, usually transmitted through BNC signal cables used for instrumentation wiring and timing. Each instrument had a unique noise signature that was measured by taking a power spectrum of an electrode grounded through the filterbox using a Textronix DPO Oscilloscope; the noise was observed to be present even without the signal filtering electronics attached to the electrode. The noise typically took the form of 4 to 20 relatively sharp peaks ($\sim$ 30kHz bandwidth) with -80dBm to -100dBm amplitude, some of which may be harmonics of other peaks. Broad noise bands are also apparent on the power spectrum, but these are generally attributed to finite length cable reflections, as they can be shifted by bending the cables, and they vary from electrode-to-electrode. The peaks were cataloged and experimental sequences needed to be modified to avoid noise generated by essential equipment that could not be powered down during experimental operation.

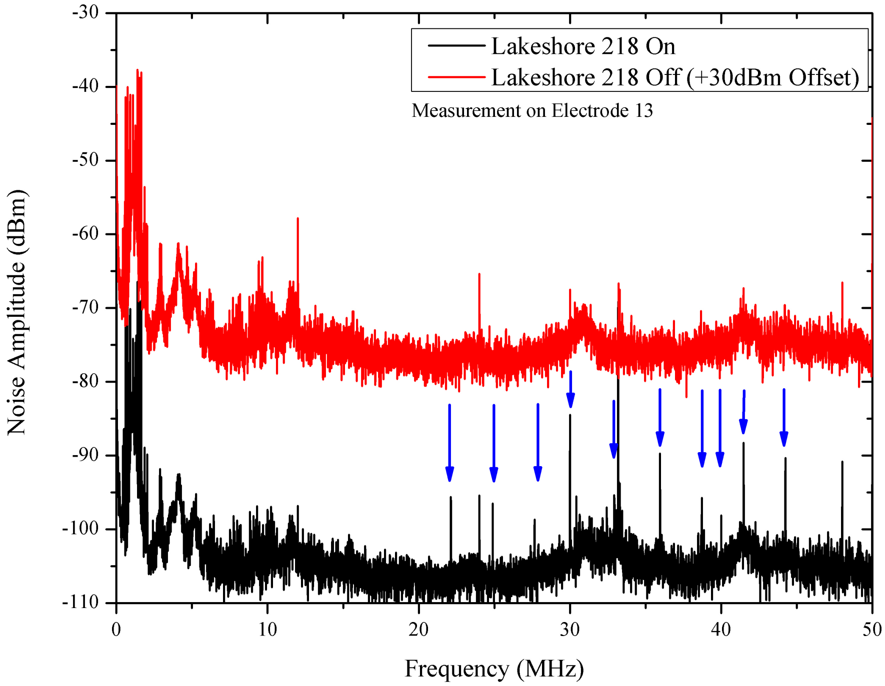

Figure 6.5: A comparison of the noise power spectrum on electrode E13 with the Lakeshore 218 temperature monitor turned on and off. This monitor is responsible for tracking temperatures of cryogenic areas in the experiment. Arrows point out strong peaks that appear in the spectrum when the power is turned on. Variations in the noise amplitude of different peaks may vary by ±5dB when repositioning the measurement cable, explaining why some peaks may look slightly higher with the sensor turned off.

Since capacitive coupling through the ground plane was the suspected coupling mechanism, the noise could be partially suppressed by a 10nF surface mount capacitor placed between the signal output and ground in the filterbox. This, however, also slows the speed at which cables can be driven by the high voltage amplifiers, so it is not a desirable solution in general.

The observed amplitude at the vacuum feedthrough does not necessarily correspond to an applied amplitude at the electrode, however there is evidence that some fraction of the signal reaches the electrode by observation of the plasma temperature as a function of the confinement well shape. The instrument with a noise peak near the sloshing frequency ($m_\theta = 0, m_z = 1$) of the confined plasma can be turned on and off, and a temperature change is observed in the plasma.

In order to confirm this behavior, a set of artificial noise peaks was injected through the filterbox into the system using a Fluke 6060A RF signal generator. By scanning either

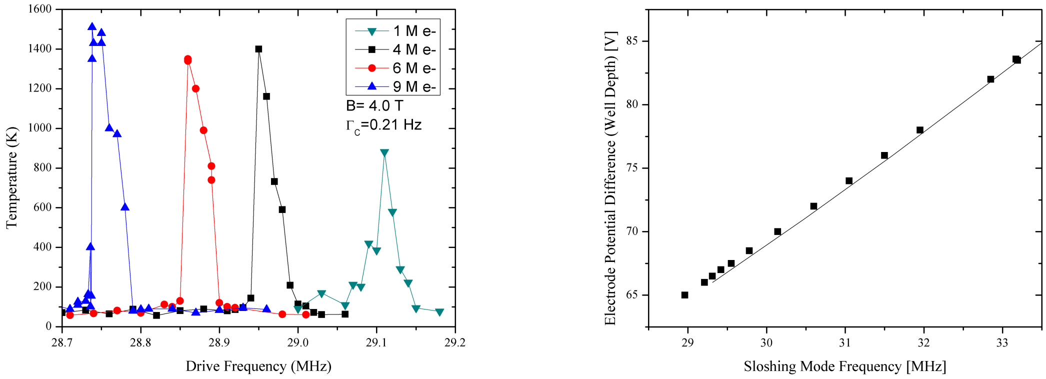

Figure 6.6: Demonstration of sloshing mode peak shifting as a function of the number of electrons trapped (*left*) in a -60V - 5V - -60V well configuration, intentionally driven by a -45dBm signal generator. These peaks can also shift if the radial profile changes significantly or the well depth is adjusted, since these will perturb the sloshing mode frequency. The plasma consistently had a radius of $r_p = 1.3$mm for this demonstration. The plasma can be stored in various well depths (*right*) to shift the frequency of the sloshing mode; data (*points*) are compared to a model including self-potential (*line*).

the depth confinement of the well or the number of particles stored, we were able to shift the bounce frequency of the plasma, to find the point of maximum heating for the signal. Injection of a -45dBm signal for $N \sim 10$ trapped million electrons yielded a asymmetric peak with 30kHz full-width at half-maximum as shown in Fig. 6.6. The source of the asymmetry in the peak is discussed in the following section. Using the artificial noise as a frequency-to-well depth calibration, scans of over a range of well-depths can be taken to check for the frequency of noise injection from other sources in the system.

Certain instruments have a significant effect on the temperature of the system for cetrain well geometries. Shown in Fig. 6.7 is the equilibrium temperature of a plasma with a particularly noisy instrument, a Lakeshore 218 temperature monitor, that performed precision four-point resistance measurements on Cernox temperature sensors installed in the experiment. Noise conceivably strongly couples capacitively through sensor cabling since many of the sensors are attached directly to the inner electrode stack. When the device was turned off, the noise in this region is reduced significantly, and points with anomalously high plasma temperatures show a drastic reduction in the temperature. Other particularly noisy instruments that were found include the high-speed camera, laptop power supplies, certain desktop power supplies, and FPGA boards used for MCP and electron gun control.

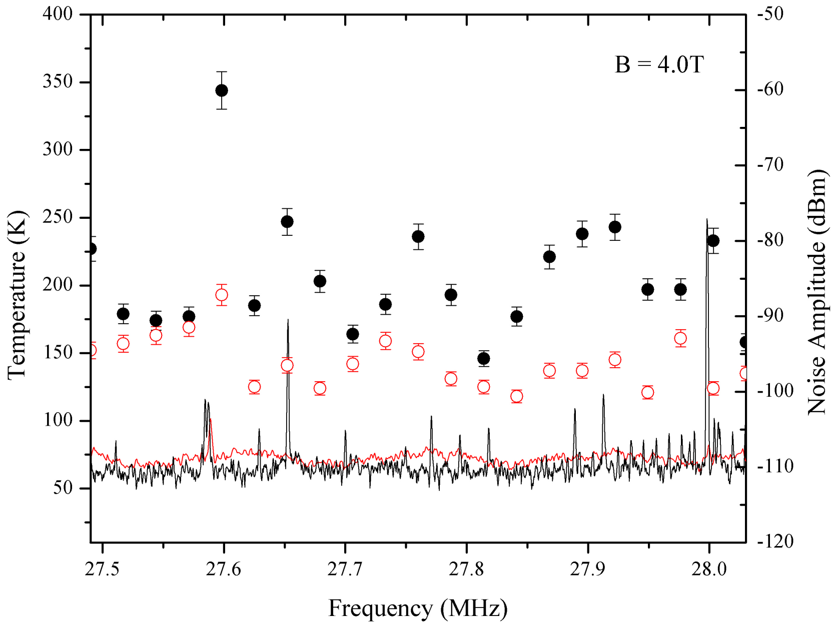

Figure 6.7: The equilibrium temperature for 2.8M trapped electrons in a near-harmonic well such that the plasma has a sloshing frequency shown on the horizontal axis. Data is taken with the Lakeshore 218 Temperature Monitor on (*black circles*) and off (*red circles*). Large differences in temperature between these two states correlates with the noise signature, shown averaged over 5s of acquisition time, associated with each temperatue profile (*solid curves, black:on, red:off*).

DAC Noise and Diocotron Motion on the Sector Electrode

As mentioned in the previous experiment, the rotating wall had the ability to drive the plasma off-center so that it developed a large diocotron orbit. This orbit was made noticeably more unstable, sending the plasma further off axis, when certain high-voltage amplifier channels were used to hold the plasma. The problem was traced back to a voltage regulator on our analog output card, a PXI-6733, which had become unstable and was injecting $<$ 20kHz ripple noise into the system through the low-pass filter lines. Once the card was serviced and replaced, diocotron stability improved dramatically.

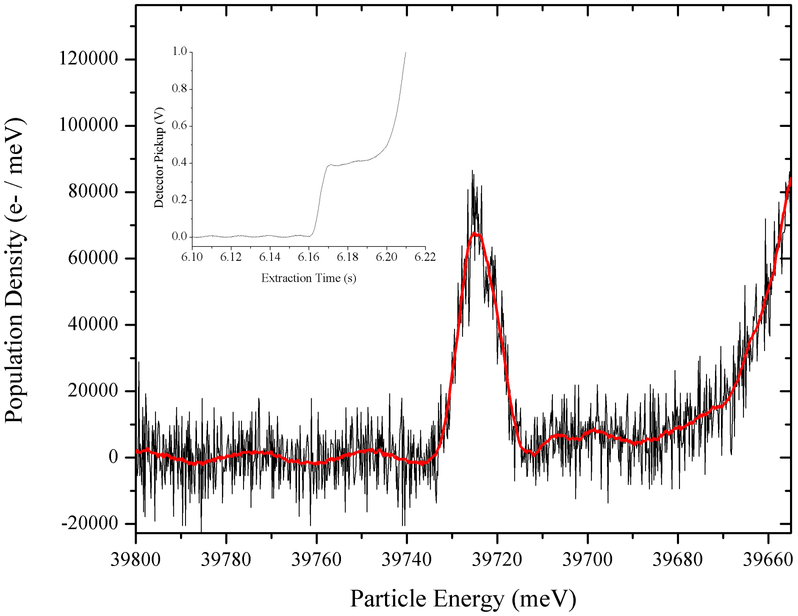

Figure 6.8: Deconvolution of an plasma extraction, rescaled to the plasma well depth. This shows the distribution of particles with respect to energy in the confining well. The raw signal from the amplifier (*inset*) is numerically deconvolved using the response of the amplifier to a fast extraction signal. The red curve is a 2.5μs smoothing operation on the signal.

6.3 Non-Maxwellian Driven Plasma Distributions

When driven near the sloshing frequency of a confined plasma, the plasma was demonstrated to generally heat in the previous section. However, the observation was made that the line-shape of the heating peak was strongly asymmetric with respect to the drive frequency. When the plasma was driven under the sloshing mode frequency, for certain ranges of drive strength, the plasma temperature was actually found to *decrease*, as measured by the typical curve-fitting procedure. This was an unexpected behavior in the plasma, and upon further analysis of the extraction curve, the particle distribution was found to not have a simple Maxwellian distribution.

The plasma is extracted smoothly over 10 to 50ms by lowering the voltage on the confining electrode, such that the plasma is generally extracted from the trap over at least 500μs. Since the time of flight of electrons escaping the well to reach the detector ($\sim$ 400ns) is much less than the total extraction time of particles onto the detector, the time of arrival gives an accurate measurement of the energy of the electron extracted from the well. The energy distribution of the confined electrons was inferred by deconvolving the time-of-arrival signal with the response of the amplifier to a pulsed charge dump.

The measured charge distribution for the high energy tail of the plasma when driven below-resonance frequency is shown in Fig. 6.8. In a Maxwellian distribution, the particles would be expected to follow an exponential distribution, with an e-folding scale ramp of $k_B T$ as particle energy is decreased. However, the distribution shown in the figure demonstrates that a portion of the charge distribution escapes early ($39732\text{mV} \geq E \geq 39715\text{mV}$), before the main bulk of the plasma is extracted ($39680\text{mV} \geq E$). The region between these two energy ranges has effectively no charge escaping. As the frequency shifts toward the sloshing frequency, the depletion band in the distribution disappears, and a Maxwellian distributed hot ($T \geq 0.2\text{eV}$) plasma is observed.

The remarkable feature of the early charge distribution was that nearly $5 \cdot 10^5$ electrons are observed to be extracted, from the center of the extraction axis with radius $r_p \approx 200\mu\text{m}$ and variance of energy, $\sigma_E = 4.1\text{meV}$. This distribution therefore appeared as a cold plasma to our temperature diagnostic due to the relatively small time scale over which particles were ejected. With enough electrons in the initial pulse, the signal saturated our detector masking the fact that the initial pulse was not part of the bulk plasma distribution, causing us to misidentify the temperature. This behavior may also explain anomalous steps in our extraction curve observed when near noisy frequency ranges potentially resonant with stored plasmas.

This behavior may be a characteristic of driven, dissipative non-linear harmonic oscillator systems. For confinement potentials used in our trap, the plasma sloshing motion has a frequency that is dependent on the amplitude of the oscillation such that $\frac{dA}{d\omega} < 0$. The drive, when under the zero-temperature sloshing frequency of the plasma forms a local attraction region in phase space that can pull electrons into islands outside the non-perturbed distribution of the plasma. While this specific system has not been well modeled at this time, this is a general behavior known for dirven, non-linear oscillator systems [26]. A simple example, with dissipations, but without self-field was demonstrated by Andrey Zhmoginov in Fig. 6.9.

The attraction region may be primarily seeded by autoresonant excitation of the plasma as the extraction pulse occurs, since the drive is necessary both at the start and end of the extraction to observe the non-thermal distribution. If drive is removed, the electrons in the phase space island are observed to thermalize into the main plasma distribution with a time scale $< 1\text{ms}$.

The sharp distribution width is of particular interest since this extraction technique could be useful for experiments requiring monoenergetic lepton beams [69, 14]. The distribution width and radial profile is comparable to those demonstrated by pulsed ejection methods [72], and with further study could be useful for generating similar lepton pulses.

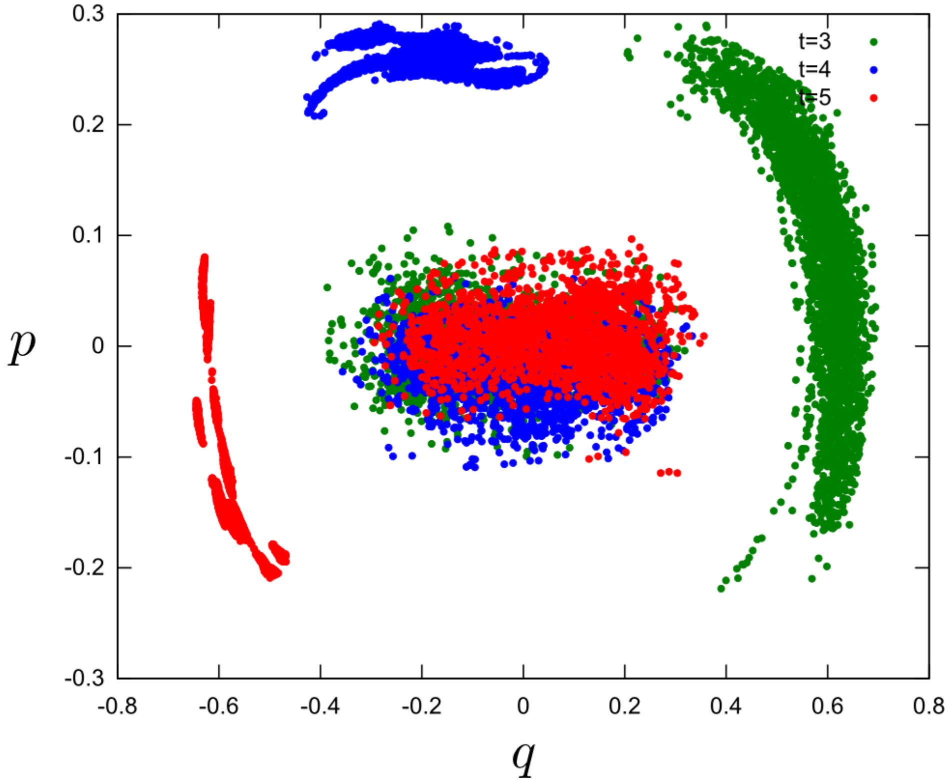

Figure 6.9: In simulations, phase space islands appear spontaneously in a simple, non-interacting distribution when a axial drive is applied to the system. For longer application of the drive, the distribution of the island becomes sharper in phase space.

Chapter 7

Future Directions and Conclusion

7.1 Recommendations and Further Studies

From the discussion in chapter 5, it is clear that there are many aspects of cooling that still need to be explored. The modes that were originally targeted in the bulge cavity behaved relatively poorly, only giving a factor of ~ 2 cooling enhancement. In the large-N_e regime, the simplistic saturation model is currently insufficient for describing the thermalization dynamics of the plasma. In particular, it was surprising that increasing the number of electrons confined in the cavity could increase the cooling rate of the system. Understanding if these behaviors are due to the overlap of the cavity mode nodes with the plasma confinement location would require a better self-potential solver for this geometry and the repair of the disconnected electrode. I anticipate that my colleagues will work on understanding the detailed dynamics and optimizing the cooling behavior in the coming months.

Since future Penning-trap cavities may include many electrodes, it would be interesting to demonstrate heat transfer between two separate electron plasmas in the same cavity as a proof-of-principle. In the same vein, it is unknown if this behavior can still be used effectively when a second species, such as ions or antiprotons, is being sympathetically cooled by an electron cloud.

There are likely relativistic corrections to the calculations presented in this paper. In particular, a Doppler shift along the axis of the cavity and a γ correction to the mass term in the cyclotron frequency may explain a part of the broadening in the lineshape of the plasma. This would mean that Γ for the ensemble is effectively a function of the temperature in each degree of freedom. It would be interesting to see if these can explain any behaviors observed in the plasmas since this would prevent the plasmas from cooling to the environmental temperature in a reasonable amount of time. It also can effect the degree to which superradiance may contribute to the cooling behavior as the number of particles approach the plasma regime.

While we have demonstrated enhanced cooling, we have not been able to demonstrate that we fully understand the heating mechanisms that were keeping the plasma warm. While it is likely that instrumentation noise can account for the majority of this heating, a detailed analysis of this should be done to ensure the coldest temperatures possible.

Unfortunately, we were not able to spend sufficient time to fully characterize the generation of a non-Maxwellian distribution discussed in Sec. 6.3. Specifically, the number of particles in the early extraction pulse was not easily reproducible, although the pulse could be readily generated by an RF drive. It would be of strong interest to the ultracold lepton beam community to further explore this behavior.

7.2 Conclusion

We have demonstrated cyclotron-cavity mode resonance cooling for single component plasmas containing 10^6 to $5 \cdot 10^7$ electrons. Electrons are confined in a Penning trap where electrodes form an electromagnetic cavity. Emission is enhanced by use of the Purcell effect to increase the spontaneous emission rates from the cyclotron motion of electrons confined in the cavity.

Bibliography

[1] Pat. 4863538A. 1989.

[2] G. Andresen et al. "A novel antiproton radial diagnostic based on octupole induced ballistic loss". In: *Phys. Plasmas* 15 (2008), p. 032107.

[3] G. Andresen et al. "Antimatter plasmas in a multipole trap for antihydrogen". In: *Physical Review Letters* 98.2 (2007).

[4] G. Andresen et al. "Compression of antiproton clouds for antihydrogen trapping". In: *Physical Review Letters* 100 (2008), p. 203401.

[5] G. B. Andresen et al. "Antiproton, positron, and electron imaging with a microchannel plate/phosphor detector". In: *Review of Scientific Instruments 80, 123701* (2009).

[6] G. B. Andresen et al. "Centrifugal Separation and Equilibration Dynamics in an Electron-Antiproton Plasma". In: *Physical Review Letters* 106.14 (2011).

[7] G. B. Andresen et al. "Magnetic multipole induced zero-rotation frequency bounce-resonant loss in a Penning-Malmberg trap used for antihydrogen trapping". In: *Physics of Plasmas* 16.10 (2009).

[8] G B Andresen et al. "Production of antihydrogen at reduced magnetic field for anti-atom trapping". In: *J. Phys. B: At. Mol. Opt. Phys* 41 (2008), p. 011001.

[9] M. D. Andresen G. B. Ashkezari, M. Baquero-Ruiz, and et al. (ALPHA). "Trapped antihydrogen". In: *Nature* 468.7324 (2010), 673–U1.

[10] B R Beck. "Measurement of the Magnetic and Temperature Dependence of the Electron Anisotropic Temperature Relaxation Rate". PhD thesis. University of California, San Diego, 1990.

[11] W. Bertsche et al. "The ALPHA experiment: a cold Antihydrogen trap". In: *Low Energy Antiproton Physics*. Ed. by W. Oelert T. Rozek D. Grzonka R. Czyzykiewicz and P. Winter. Vol. 796. AIP, 2005, p. 301.

[12] J. J. Bollinger and D. J. Wineland. "Strongly Coupled Nonneutral Ion Plasma". In: *Phys. Rev. Lett. 53, 348* (1984).

[13] R.G. Greaves C.M. Surko C. Kurz S.J. Gilbert. "New source of ultra-cold positron and electron beams". In: *Nuclear Instruments and Methods in Physics Research B 143, 188* (1998).

[14] G. F. Gribakin C. M. Surko and S. J. Buckman. "Low - energy positron interactions with atoms and molecules". In: *Journal of Physics B 38 R57-R126* (2005).

[15] S. Chapman. "The Effect of Multipole-Enhanced Diffusion on the Joule Heating of a Cold Non-Neutral Plasma". PhD thesis. University of California, Berkeley, 2011.

[16] J.-H. Choi et al. "Trapping and Evolution Dynamics of Ultracold Two-Component Plasmas". In: *Physical Review Letters* 100 (2008), p. 175002.

[17] B. R. Beck A. W. Hyatt D. L. Eggleston C. F. Driscoll and J. H. Malmberg. "Parallel energy analyzer for pure electron plasma devices". In: *Phys. Fluids B 4, 3432* (1992).

[18] J. R. Danielson and C. M. Surko. "Torque-Balanced High-Density Steady States of Single-Component Plasmas". In: *Physical Review Letters* 94 (2005), p. 0305001.

[19] R Dicke. "Coherence in Spontaneous Radiation Processes". In: *Physical Review 93 (1): 99110.* (1954).

[20] C. F. Driscoll, K. S. Fine, and J. H. Malmberg. "Reduction of Radial Losses in a Pure Electron Plasma". In: *Phys. Fluids* 29 (1986), p. 2015.

[21] D H E Dubin. "Electrostatic waves and instabilities in multispecies nonneutral plasmas". In: *Phys. Plasmas 17, 112115* (2010).

[22] D. H. E. Dubin. "Equilibrium and dynamics of uniform density ellipsoidal non-neutral plasmas". In: *Phys. Fluids B 5, 2* (1993).

[23] D H. E. Dubin and T. M. ONeil. "Trapped nonneutral plasmas, liquids, and crystals (the thermal equilibrium states)". In: *Rev. Mod. Phys. 71, 87* (1999).

[24] D. Durkin and J. Fajans. "Experiments on two-dimensional vortex patterns". In: *Phys. Fluids* 12 (2000), p. 289.

[25] F. Anderegg E. M. Hollmann and C. F. Driscoll. "Confinement and manipulation of non-neutral plasmas using rotating wall electric fields". In: *Physics of Plasmas* (2000).

[26] J. P. Eckmann and D. Ruelle. "Ergodic theory of chaos and strange attractors". In: *Rev. Mod. Phys. 57, 617* (1985).

[27] Ronald C. Davidson Edward H. Chao and Stephen F. Paul. "Non-neutral plasma expansion induced by electron-neutral collisions in a MalmbergPenning trap". In: *J. Vac. Sci. Technol. A 17, 2050* (1999).

[28] L T Evans. "Implementation of fast algorithms for fitting modified Gaussians to images". *Internal communication* (2014).

[29] Nathan Evetts. "*Work in Progress, Not Yet Titled*". MA thesis. University of British Columbia, Vancouver, 2015.

[30] D H E Dubin C F Driscoll R W Gould F Anderegg N Shiga. "Thermally excited Trivelpiece-Gould Modes as a Pure Electron Plasma Diagnostic". In: *Physics of Plasmas, 10 1556* (2002).

[31] Robert W. Connatser Jeanette S. Conway Fred B. Seeley Joseph E. Alexander and Jonathan P. Dowling. “Dipole radiators in a cavity: A radio frequency analog for the modification of atomic spontaneous emission rates between mirrors”. In: *Am. J. Phys. 61, 545* (1993).

[32] D. Le Sage B. Levitt W. S. Kolthammer I. Kuljanishvili R. McConnell J. Wrubel F. M. Esser H. Glueckler D. Grzonka G. Hansen S. Martin W. Oelert J. Schillings M. Schmitt T. Sefzick H. Soltner Z. Zhang D. Comeau M. C. George E. A. Hessels C. H. Storry M. Weel A. Speck F. Nillius J. Walz G. Gabrielse P. Larochelle and T. W. Haensch. “Antiproton Confinement in a Penning-Ioffe Trap for Antihydrogen”. In: *PRL 98, 113002* (2007).

[33] W. S. Kolthammer R. McConnell P. Richerme D. Grzonka W. Oelert T. Sefzick M. Zielinski D. W. Fitzakerley M. C. George E. A. Hessels C. H. Storry M. Weel A. Muellers G. Gabrielse R. Kalra and J. Walz. “Trapped Antihydrogen in Its Ground State”. In: *Phys. Rev. Lett. 108, 113002* (2012).

[34] K O Jensen G M Dunn and A B Walker. “Positron states in vacancies and voids”. In: *J. Phys.: Condens. Matter 3 2049* (1991).

[35] G Gabrielse and H Dehmelt. “Observation of Inhibited Spontaneous Emis”. In: *Physical Review Letters 55, 67* (1985).

[36] J.E. Lees G.W. Fraser M.T. Pain and J.F. Pearson. “The operation of microchannel plates at high count rates”. In: *Nuc. Instr. and Methods A* 306 (1991), pp. 247–260.

[37] H Taniyama H Sumikura E Kuramochi and M Notomi. “Ultrafast spontaneous emission of copper-doped silicon enhanced by an optical nanocavity”. In: *Scientific Reports 4, 5040* (2013).

[38] David Hanneke. “Cavity Control in a Single-Electron Quantum Cyclotron: An Improved Measurement of the Electron Magnetic Moment”. PhD thesis. Harvard, 2007.

[39] H. Higaki et al. “Radial compression of protons and H3+ ions in a multiring trap for the productionof ultralow energy antiproton beams”. In: *Phys. Rev. E* 70 (2004), p. 026501.

[40] M. H. Holzcheiter et al. “Trapping of antiprotons in a large Penning trap - progress towards a measurement of the gravitational acceleration of the antiproton”. In: *Nucl. Phys. A* 558 (1993), pp. 709–718.

[41] C. Schmidt J. A. Palkovic F. E. Mills and D. E. Young. “Gabor lens focusing of a proton beam”. In: *Rev. Sci. Instrum. 61, 550* (1990).

[42] F. L. Moore W. M. Itano J. J. Bollinger D. J. Heinzen and D. J. Wineland. “Low Order Modes of an Ion Cloud in a Penning Trap”. In: *Physica Scripta. Vol. 46, 282-284* (1992).

[43] A Jain. “Dynamic Effects in Superconducting Magnets”. In: *US Particle Accelerator School on Superconducting Accelerator Magnets, Santa Barbara, California, June 23-27, 2003.* 2003.

[44] C.M. Surko J.R. Danielson and T.M. O’Neil. “High-Density Fixed Point for Radially Compressed Single-Component Plasmas”. In: *Phys. Rev. Lett. 99, 135005* (2007).

[45] S. Das S. Guduri A. C. Bovik K. R. Diller K. A. Bartels R. H. Crawford and S. J. Aggarwal. “Fabrication of macroscopic solid models of three-dimensional microscopic data by selective laser sintering”. In: *Journal of Microscopy 169, 383-389* (1993).

[46] Bollinger J.J. ; Jelenkovic B.M. ; Mitchell T.B. ; Itano W.M. ; Wineland D.J. King L.B. “Laser-cooled non-neutral plasma experiments at NIST”. In: 1999.

[47] Daniel Kleppner. “Inhibited Spontaneous Emission”. In: *Phys. Rev. Lett. 47, 233* (1981).

[48] L.D. Landau and E. M Lifschitz. *Quantum Mechanics: Non-Relativistic Theory.* Pergamon Press, London, 1981.

[49] Jinhyung Lee and John R. Cary. “Longitudinal cooling of non-neutral plasma by energy exchange”. In: *Physical Review E 71, 036406* (2005).

[50] C. M. Surko. M. Leventhal and A. Passner. In: *Phys. Rev. Lett. 62, 901* (1989).

[51] R H Levy. “Diocotron instability in a cylindrical geometry”. In: *Phys. Fluids 8, 1288* (1965).

[52] C. Carraro V. Lagomarsino A. Odino G. Testera M. Amoretti C. Canali and S. Zavatarelli. “Centrifugal separation of ions and an oppositely charged non-neutral plasma”. In: *Phys. Plasmas 13, 012308* (2006).

[53] R. J. Brecha H. J. Kimble M. G. Raizen R. J. Thompson and H. J. Carmichael. “Normal-mode splitting and linewidth averaging for two-state atoms in an optical cavity”. In: *Phys. Rev. Lett. 63, 240* (1989).

[54] P. Mansbach and J. Keck. “Monte Carlo trajectory calculations of atomic excitation and ionization by thermal electrons”. In: *Phys. Rev. 181, 275* (1969).

[55] D. W. Marquardt. In: *SIAM Journal on Applied Mathematics 11(2), 431441* (1963).

[56] *MSDS and Property Datasheets for materials available at `http://www.shapeways.com/` and `http://eos.materialdatacenter.com/`.*

[57] T.M. O’Neil and P. G. Hjorth. In: *Phys. Fluids **28**, 3241* (1985).

[58] R Parthasarathy. “Rapid, accurate particle tracking by calculation of radial symmetry centers”. In: *Nat Methods 9(7), 724726* (2012).

[59] R. N. Peacock. In: *J. Vac. Sci. Technol., **17**, 330* (1980).

[60] S. Peil and G. Gabrielse. “Observing the Quantum Limit of an Electron Cyclotron: QND Measurements of Quantum Jumps between Fock States”. In: *Physical Review 83, 1287* (1999).

[61] A. J. Peurrung and J. Fajans. "A Pulsed, Microchannel Plate-Based, Nonneutral Plasma Imaging System". In: *Review of Scientific Instruments* 64 (1993), p. 52.

[62] E. M. Purcell. In: *Phys. Rev. 69, 681* (1946).

[63] P. A. Redhead. "Ultrahigh vacuum pressure measurements: Limiting processes". In: *J. Vac. Sci. Technol. A* ***5**, 3215* (1987).

[64] J J Sakurai. *Advanced Quantum Mechanics*. Addison-Wesley, 1967.

[65] *ScintiMax Spec. Sheet*. El-Mul Technologies. 2007. URL: `http://www.el-mul.com/My%20Documents/pdf/ScintiMax_2007.pdf`.

[66] *Sensicam qe datasheet*. PCO. URL: `http://www.pco.de/fileadmin/user_upload/db/products/datasheet/sensicam_qe_20080624.pdf`.

[67] R W Siegel. "Positron Annihilation Spectroscopy". In: *Annual Review of Materials Science Vol. 10: 393-425* (1980).

[68] Joseph J. Beaman David L. Bourell Suman Das Martin Wohlert. "Producing metal parts with selective laser sintering/hot isostatic pressing". In: *JOM, 50 12 17-20* (1998).

[69] C. M. Surko and R. G. Greaves. "Emerging science and technology of antimatter plasmas and trap-based beams". In: *Phys. Plasmas 11, 2333* (2004).

[70] M. Lundin T. Govett K. Kim and D. Pinero. "Design Rules For Selective Laser Sintering". at Mechanical Engineering Design Projects Program, The University of Texas at Austin (2012).

[71] J. E. Barth T. H. Hoenderken C. W. Hagen and P. Kruit. "Influence of the microchannel plate and anode gap parameters on the spatial resolution of an image intensifier". In: *J. Vac. Sci. Technol. B, 19, 3* (2001).

[72] J. R. Danielson T. R. Weber and C. M. Surko. "Creation of finely focused particle beams from single-component plasmas". In: *Physics of Plasmas 15, 012106* (2008).

[73] J. R. Danielson T. R. Weber and C. M. Surko. "Electrostatic beams from tailored plasmas in a PenningMalmberg trap". In: *Physics of Plasmas 17, 123507* (2010).

[74] M Taborelli. In: *CAS - CERN Accelerator School and ALBA Synchrotron Light Facility : Course on Vacuum in Accelerators, Platja d'Aro, Spain.* 2006.

[75] J Tan and G Gabrielse. "Parametrically-Pumped electron oscillators". In: *Physical Review A 48, 3105* (1993).

[76] Joseph N. Tan. "Cooperative Behavior in Cavity-Cooled, Parametrically-Pumped Electron Oscillators". PhD thesis. Harvard, 1992.

[77] Jim Williams. *High Speed Amplifier Techniques*. Tech. rep. Linear Technology, 1991.

[78] J. L. Wiza. "Microchannel Plate Detectors". In: *Nuc. Instr. and Methods A* 162 (1979), p. 587.

[79] H Yokoyama and K Ujihara. *Spontaneous Emission and Laser Oscillation in Microcavities*. Ed. by H Yokoyama and K Ujihara. CRC Press, 1995.